ABSTRACT

Title of Document: OPTICAL NONLINEARITIES NEAR SINGLE PHOTON LEVEL WITH A QUANTUM DOT COUPLED TO A PHOTONIC CRYSTAL CAVITY

Deepak Sridharan, Doctor of Philosophy
2011

Directed By: Professor. Edo Waks
Department of Electrical and Computer Engineering

Over the last decade, exponential increase of information bandwidth over the internet and other communication media has increased the total power consumed by the devices associated with information exchange. With ever increasing number of users, and packing of a higher number of devices onto a chip, there is a great need for reduction in not only the power consumption of the devices but also the costs associated with information transfer. Currently, the benchmark in the energy consumption per logic operation is at femtojoule level and is set by the CMOS industry. However, optical devices based on single photon emitters coupled to a microcavity have the potential to reduce the optical power dissipation down to attojoule levels wherein only few 10s of photons are consumed for a logic operation.

This work presents our theoretical and experimental efforts towards realization of all optical device based on the enhanced nonlinearities of a single photon emitter in a photonic crystal cavity. We show that a single quantum dot coupled to a photonic crystal cavity can be used to route an incoming optical beam with optical power dissipation of 14 attojoules, corresponding to only 65 photons. This value is well below the operational level for current CMOS devices indicating the potential for chip based optical transistors for reduction in energy consumption. The single photon emitters that we use to create the nonlinearity are the quantum dots, which are semiconductor nanostructures that exhibit a discrete energy spectrum. The interaction of the quantum dot, with light confined inside a photonic crystal cavity, results in strong atom-photon interactions which can be used for ultra-low power all optical switching. The strong interactions between a quantum dot and photonic crystal cavity can be further utilized to realize quantum computation schemes on a chip.

I also describe techniques for integrating this transistor into an optical circuit, and discuss methods for post fabrication tuning to make reconfigurable active photonic devices that implement optical data processing at low light levels.

OPTICAL NONLINEARITIES NEAR SINGLE PHOTON LEVEL WITH A QUANTUM DOT COUPLED TO A PHOTONIC CRYSTAL CAVITY

By

Deepak Sridharan

Dissertation submitted to the Faculty of the Graduate School of the
University of Maryland, College Park, in partial fulfillment
of the requirements for the degree of
Doctor of Philosophy
2011

Advisory Committee:
Professor Edo Waks, Chair
Professor Julius Goldhar
Professor Christopher Davis
Professor Luis Orozco
Professor Victor Granatstein

Dedication

Dedicated to my ‘Amma’ – the sole reason of my existence.

Acknowledgements

First and foremost, I would like to thank my advisor Edo Waks, who has served as source of both information and inspiration for me. I started working for him at a time when I was thinking of quitting the scientific field. However, the numerous interactions with him have helped me change my perspective of research and have also shaped into a good human being. I owe my entire knowledge of quantum optics that I gained over the last 5 years to him. I just hope and pray I will be able to do justice to whatever he has taught me.

I have also benefited from my interactions with Glenn Solomon at NIST. My work would be incomplete without acknowledging him, who grew all the quantum dots that I had used for my experiments. I would like to thank my proposal and thesis committee members Prof. Thomas Murphy, Prof Julius Goldhar, Prof Christopher Davis and Prof Luis Orozco. I offer my sincere gratitude to Ranojoy Bose who came in at a crucial time during my PhD. The ability to run experiments with someone to oversee and point out mistakes and take some rest in between without stopping the experiments took a lot of pressure off me. This also gave me the time that I needed to concentrate on theoretical work.

I would also like to thank all my past and current lab members Sina Sahand, Chad Ropp, Shilpi Gupta, Hyochul Kim, Thomas Shen and Kangmook Lim who have made this trip memorable.

I want to thank the people at the Maryland Nanocenter: Jon Hummel, Tom Loughran and John Abrahams who trained me on the electron beam lithography and inductively coupled plasma systems which were a lifeline for my research. Jay Pyle at IREAP has been extremely helpful both during the initial stages of setting up the lab and also over the course of my PhD.

A special thanks to my friend Charles who was with me during testing times and has helped me attain this position.

Life at University of Maryland has given be a lot of good things and good friends. One among the special persons is Jyoti who has been with me throughout this journey, comforting me during tough times and sharing my happiness during the rest. This would definitely not have been possible without her.

Contents

List of Figures

Chapter 1

Introduction

1.1 Overview

The demand for faster and more energy efficient information technology has experienced a significant increase over the past few years. All-optical transistors are considered to be an important alternative for increasing information bandwidth. These devices enable optical signal processing without having to perform transduction to electrical current. A variety of all optical switching devices have been demonstrated using various device structures such as semiconductor quantum wells, semiconductor optical amplifiers, and nonlinear parametric processes. These devices typically rely on weak nonlinearities from a large ensemble of atomic systems, and therefore require large device sizes and dissipate large powers. Photonic crystals (PCs) have been shown as an effective method for significantly reducing optical device sizes. PC optical transistors have been demonstrated using free carrier absorption and laser gain modulation, but these devices still operate in the 0.6-15 fJ range, well above the 0.1 fJ energy dissipation levels of typical CMOS electrical transistors.

All-optical transistors are expected to play an important role in future low power ultra-high bandwidth signal processing [1]. The majority of optical transistors to date achieve optical switching using weak atom-light interactions from a large ensemble of atomic systems [2-7], resulting in high power dissipation and large device size [8]. Here we demonstrate an ultra-compact all-optical transistor with only 14 attojoules of energy dissipation where the optical switching is implemented by a single atom-like system, a semiconductor quantum dot (QD). The device is composed of a QD coupled to a photonic crystal cavity-waveguide optical circuit, where the photonic crystal provides strong light localization creating extremely large optical nonlinearities, even with a single QD [9-12]. The energy dissipation of the demonstrated device is two orders of magnitude lower than previously reported photonic crystal transistors [13,14], and nearly an order of magnitude lower than electrical CMOS transistors [15]. We demonstrate switching speeds of up to 8.4 GHz, providing the potential for high bandwidth and low power consumption optical signal processing in an ultra-compact chip-based device.

In this chapter, I begin by giving an introduction to quantum dots and their advantages. Then I explain the advantages of photonic crystals and how they can be utilized to control and exploit the properties of quantum dots. Particularly, the interaction between the quantum dot and a photonic crystal cavity results in an enhancement of nonlinearities of the quantum dot which can be utilized to achieve ultra-low power all optical switching on a chip. Chapter 2 describes our efforts to resonantly probe a cavity-QD system in-plane through a coupled waveguide mode. In Chapter 3, I show the observation of cavity enhanced stark effect of a QD which is coupled to the cavity. In Chapter 4, I describe the operation of the all optical switch and show that the main nonlinearity involved in switching of an incoming optical beam is the stark shift of the quantum dot. In Chapter 5, I present a theoretical model for an all optical switch based on quantum dots embedded in a DBR cavity. In Chapter 6, I introduce a new technique based on photochromic films to tune the resonances of photonic crystal cavities. In Chapter 7, I use this photochromic technique to demonstrate a reversibly tunable photonic crystal laser. Finally, in

Chapter 8, I describe a protocol to create entanglement between spatially separated quantum dots based on the interactions between a quantum dot and cavity.

1.2 Quantum Dots

Quantum dots are semiconductor nanostructures which are confined in all the three dimensions in space [16]. The three dimensional confinement of the carrier in space gives rise to discrete density of the states. The localized density of states in both the conduction and valence band of the QD and discrete transitions of the QD is very similar to that of atoms and hence QDs are labeled as artificial atoms. In general, the emission properties of a single QD is very complicated. The emission properties of a QD can be understood from the energy band diagram of a QD shown in Fig 1. The number of levels than can exist in a QD is determined by the depth of the potential barrier. The basic excitonic transition of the QD is obtained when one electron is captured in the conduction band s state and one hole is captured in valence band s state. Similarly, if two electrons and one hole are captured in the QD, one electron-hole pair can recombine to give rise to a transition which leaves the QD charged negatively. Likewise, other transitions are also possible between the other states of the QD including neutral and charged transitions. Thus, the spectrum of QD emission is in general very complicated depending upon the transitional probabilities between each state which in turn depends on the growth parameters of the QD. However, for all practical purposes we can treat the QD as being similar to a two level atom by considering just the transition between the s states of the conduction and valence since they are the most well trapped. Thus, the equations used to model of the interaction of optical fields with two level systems are equally valid to QD system.

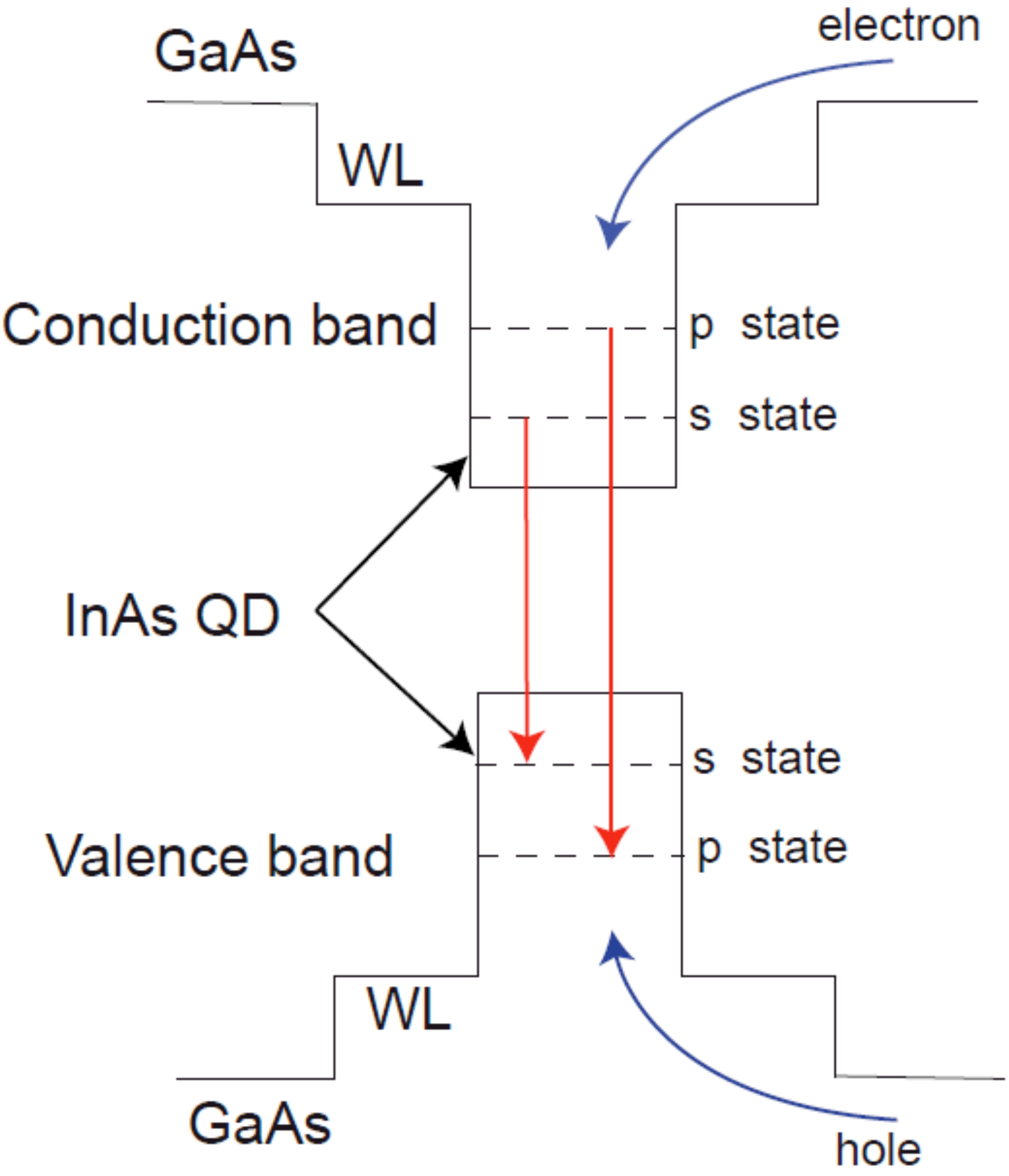

Figure 1 : Energy band diagram of a QD showing the energy of the QD state in relation to bulk GaAs state. Carriers (electrons and holes) are trapped in the QD potential well giving rise to various emissions. WL is the wetting layer state.

The field of quantum information processing based on atoms and ions is the most well developed compared to the systems based on QDs. However, one important advantage of QDs over these systems, which is of particular importance in the field of optical communications, is that QD systems are easily scalable. To replicate and further the field of quantum information processing it is necessary to develop an easily scalable architecture. QDs which can mass fabricated with well known fabrication techniques are the most ideally suited for this.

The emission properties of a QD can be characterized by pumping a sample consisting of QDs cooled down to 4K with a cw laser at 780 nm. The sample is maintained at a temperature of 4K to minimize the phonon dephasing processes which increase the linewidth of the QD transition. Since the laser wavelength is below the bandgap of GaAs, the laser creates excess carriers in the conduction and valence band of GaAs. If these carriers are close enough to the QD, they can fall into the lowest states of the QD giving rise to an excitonic transition corresponding to the s-state transition of the QD as shown in Figure 2a.

The random growth of the QDs on the sample during Molecular Beam Epitaxy ensures that each no two QD have the same shape and size [17-19]. The emission frequency of the QD which is dependent on the shape and size of the QD is also different in this case. In this case, if we excite a collection of QDs with an above band laser, we observe emission corresponding to all the QDs which have been excited. This spread in the observed frequency spectrum of a collection of QDs is the inhomogeneous broadening of the QDs and is shown in Figure 2b.

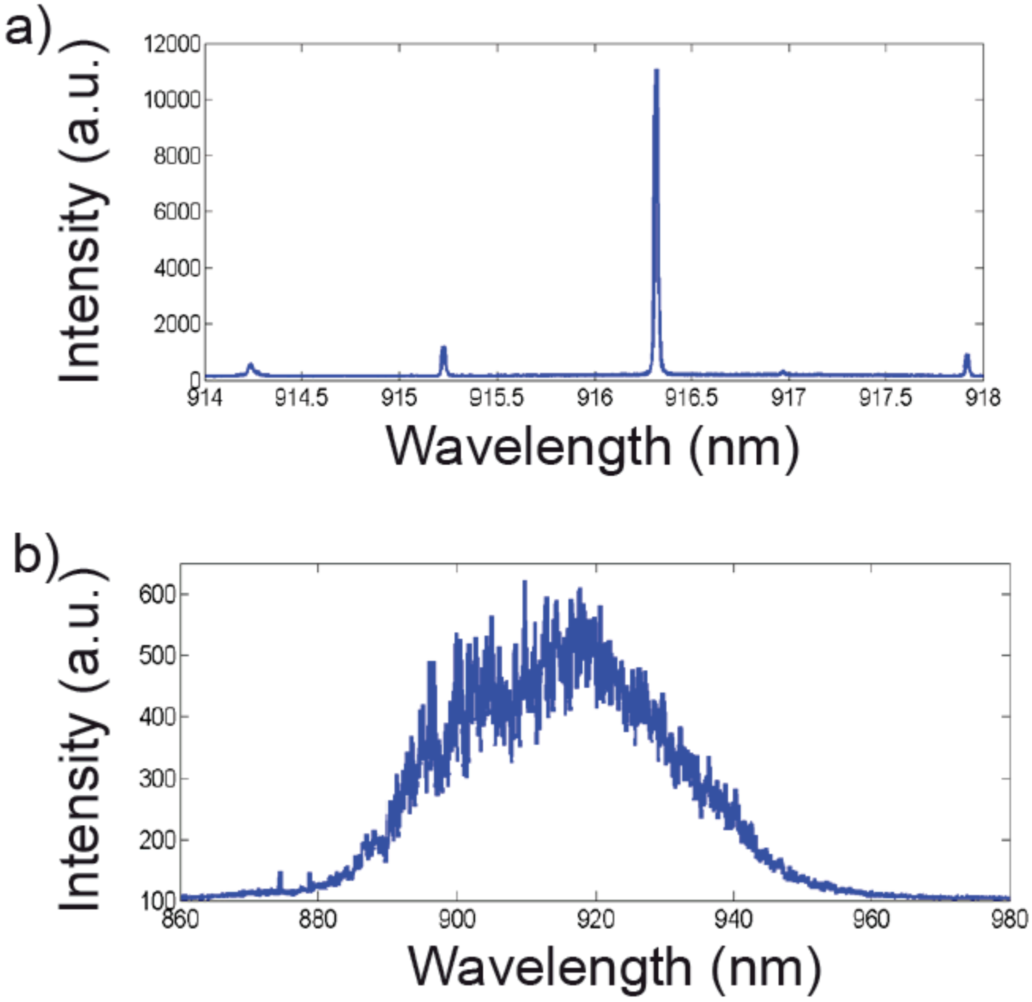

Figure 2 : a) Single QD spectrum at low excitation intensity showing the s-state transition b) Collective excitation of QDs showing the inhomogeneous broadening

1.3 Photonic Crystal

The strength of interaction between a quantum dot and a laser used to excite the quantum dot depends upon the electric field the QD experiences at its position. This strength of interaction can be enhanced by embedding the QD in a photonic crystal cavity, which localizes light into volumes much smaller than the wavelength of light. Photonic crystals are semiconductor devices with periodic and random variation of the refractive index which can be used to selectively engineer electromagnetic modes at frequencies in the materials. This amazing control over the modes which can be created in a photonic crystal can be utilized to control the radiative properties of the materials and localize photons, as first proposed by Yablonovitch in 1987 [20]. As light waves scatter within the photonic crystal, destructive interference cancels out light of certain wavelengths, thereby forming a photonic bandgap, similar to the energy bandgap for electron waves in a semiconductor. Photons whose energies lie within the gap cannot propagate through the periodic structure.

We can also create defects within a periodic array of photonic crystal device by removing a lattice point in the array to give rise to a point defect. In this case, light injected into the point defect called a cavity becomes locally trapped giving rise to a large electric field in the cavity region. Similarly, a line of defects can serve as a waveguide. For a QD embedded within a PC cavity, the interaction with the large electric field gives rise to nonlinear effects with Kerr nonlinearities several magnitudes higher than what has been observed in bulk materials.

1.4 Interaction between quantum dot and a microcavity

The theory of the interaction between a QD and a microcavity can be described by the Jaynes-Cumming Hamiltonian. The total Hamiltonian between the QD and cavity is given by [21]

$$H = \hbar\omega_{cav}\hat{\mathbf{b}}^{\dagger}\hat{\mathbf{b}} + \hbar\omega_{QD}\hat{\sigma}_{+}\hat{\sigma}_{-} + \hbar g\left(\hat{\mathbf{b}}^{\dagger}\hat{\sigma}_{-} - \hat{\sigma}_{+}\hat{\mathbf{b}}\right) \tag{1.1}$$

where $\hat{\mathbf{b}}$ is the bosonic operator in the cavity field which annihilates a photon and $\hat{\sigma}_{-}$ is the dipole lowering operator. The first two terms correspond to the energies of the cavity and QD. The last term corresponds to the Jaynes-Cumming interaction energy between the cavity and QD.

Based on the Hamiltonian of the system, the Heisenberg equations of motion for the cavity field and the QD operator can be derived to be

$$\begin{aligned} \frac{d\hat{\mathbf{b}}}{dt} &= -\left(i\omega_{cav} + \frac{\kappa}{2}\right)\hat{\mathbf{b}} - ig\hat{\sigma}_- \\ \frac{d\hat{\sigma}_-}{dt} &= -\left(i\omega_{QD} + \frac{\gamma}{2}\right)\hat{\sigma}_- - ig\hat{\mathbf{b}} \end{aligned} \tag{1.2}$$

The system of equations relating the cavity field operator $\hat{\mathbf{b}}$ and dipole operator $\hat{\sigma}_-$ can now be diagonalized to obtain the frequency eigenstates of the system which are give by

$$\omega_\pm = \frac{\omega_{cav} + \omega_{QD}}{2} + i\left(\frac{\kappa + \gamma}{4}\right) \pm \sqrt{g^2 - \frac{\left(\kappa - \gamma - i\left(\omega_{cav} - \omega_{QD}\right)\right)^2}{4}} \tag{1.3}$$

From the previous expression, the system can exist in two eigenstates different from the initial resonances of the QD and cavity in one regime called the strong coupling regime. In the other regime called the weak coupling regime, the QD and cavity resonances do not change.

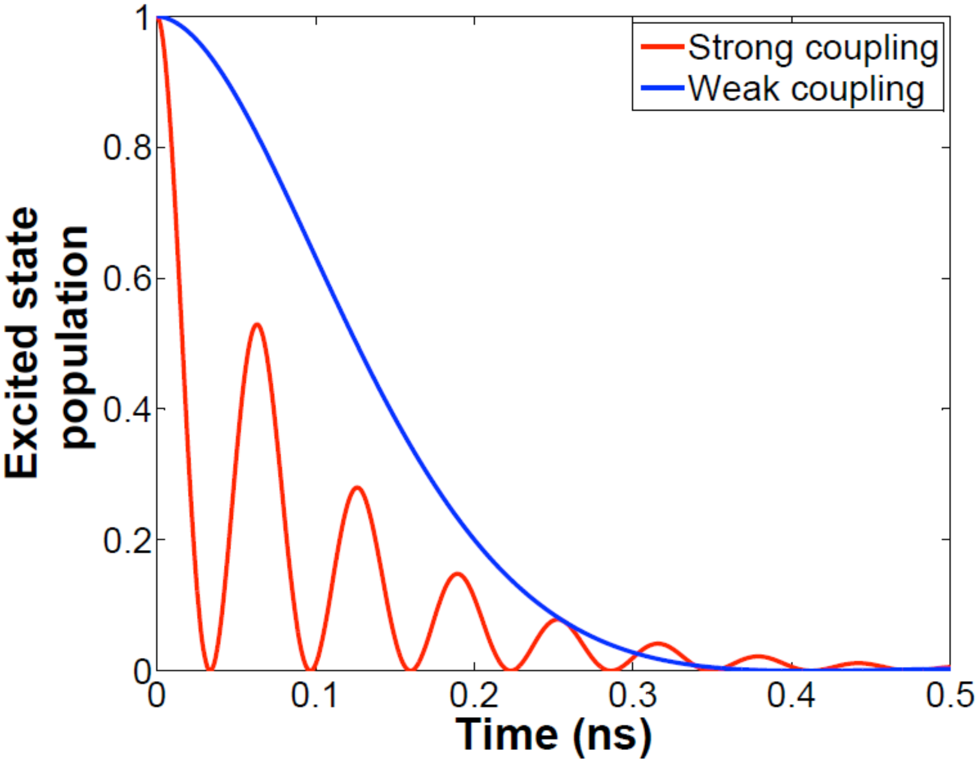

Figure 3 : Population of the excited state of the quantum dot in strong coupling and weak coupling regimes as a function of time. The red curve corresponds to the strong coupling regime with parameters g = 50 GHz and $\kappa = 20\,\mathrm{GHz}$. The blue curve corresponds to weak coupling with g = 4 GHz and $\kappa = 20\,\mathrm{GHz}$

1.4.1 Weak Coupling Regime

In the weak coupling regime, the vacuum Rabi frequency is smaller than the decay rate of the QD and cavity. The decay rate of InAs QDs in bulk is 0.16 GHz [22]. This is usually much smaller than the experimentally achieved cavity decay rate and hence can be neglected for cavity-QD systems. In this case, the eigenstates of the system are given by

$$\begin{aligned}\omega_+ &= \omega_{cav} + i\frac{\kappa}{2} \\ \omega_- &= \omega_{QD} + i\left(\frac{\gamma}{2} + \frac{2g^2}{\kappa}\right)\end{aligned} \tag{1.4}$$

The two eigenstates correspond to the states of the cavity and QD whose frequencies remain unperturbed in the weak coupling regime. However, the decay rate of the QD is modified due to the presence of the cavity mode. This enhancement in the decay rate of the QD is called Purcell enhancement and the factor by which the decay rate is enhanced is called the Purcell factor [23].

The enhancement of decay rate of a QD inside a cavity is attributed to the modification of the local density of states by the cavity. A QD in free space spontaneously emits due to the coupling to the vacuum field modes of the external environment. In the presence of a cavity, the modes are modified such that certain modes are enhanced and others suppressed. Thus, depending upon which mode the QD is resonant with, its emission can either be enhanced or suppressed. If the QD is resonant with the cavity mode, then the emission of the QD is enhanced giving rise to a faster modified decay rate. If the QD is off-resonant from the cavity, the emission of the QD is suppressed giving rise to a longer modified decay rate of the QD.

1.4.2 Strong Coupling Regime

The other regime is called the strong coupling regime. In this case, the vacuum Rabi frequency of the QD is higher than the decay rate of the cavity. The eigenstates now are different from the cavity and QD frequencies and are given by

$$\omega_{\pm} = \frac{\omega_{cav} + \omega_{QD}}{2} + i\left(\frac{\kappa + \gamma}{4}\right) \pm g \qquad (1.5)$$

The strong coupling regime can be understood by considering the simple picture of the QD as a two-level system and a quantized cavity which can hold a maximum of only one photon. Let us consider the case where the system is in the initial state with one photon in the cavity and the QD in the ground state. If we let the system evolve, the photon in the cavity is absorbed by the QD resulting in a state of no photons in the cavity and the QD in the excited state. On further evolution of the system, the QD decays to the ground state due to spontaneous emission into the cavity mode giving rise to one photon in the cavity. In the absence of any leakage of the cavity and QD, this process continues cyclically with the frequency of oscillations of the QD population and cavity photon number given by g. Hence, g is referred to Rabi 'frequency' of the system.

In the frequency domain picture, it has already been shown that the eigenstates of the cavity-QD system in strong coupling are no longer equivalent to the individual cavity and QD frequencies. This can also be understood from the simple cavity-QD picture. As the QD emits a photon into the cavity mode, we do not consider the cavity and QD as separate entities. We identify the cavity field and the QD state as a combined polariton mode. It is precisely the frequency of the polariton modes, called the lower and upper polaritons which is given by the eigen frequencies of the system.

It is of importance to note at this point that for the nonlinear switching experiments that we are trying to achieve with a single QD in a photonic crystal cavity, it is irrelevant which regime we are in. Our experiments are equally valid in both weak and strong coupling. However, we strive to achieve strong coupling in our cavity-QD system for two reasons. First, experimentally things are much easier with the system in strong coupling. The scattered signal from the cavity-QD system can be resolved in a grating spectrometer, which in the case of strong coupling show two peaks corresponding to the two polariton modes. Secondly, the fact that the system is in strong coupling implies that the interaction strength between the QD and cavity is strong. This strong interaction between the two gives rise to higher resonant and nonresonant nonlinearities of the device. In terms of optical switching, this implies that if we want to the switch the transition of a QD embedded within a cavity, lesser photons would be needed for a QD with a higher g. Thus, we strive to achieve strong coupling not because we want to see the Rabi oscillations of the QD, as is the case with quantum information experiments, but because we want higher interaction strength between the cavity and QD.

1.5 Accessing modes of the cavity

So far we have been talking about the interaction between the QD and photons in the cavity. However, we have not mentioned anything about how photons can be injected into the cavity. To illustrate how the cavity mode can be accessed, we consider a cavity-waveguide system, the schematic for which is shown in Figure 4. The cavity has been realized in the photonic crystal lattice by the removal of three holes. This cavity has been optimized to have the highest *Q* for a 3 hole defect interacting with a waveguide mode. The waveguide has been realized by the removal of a line of holes.

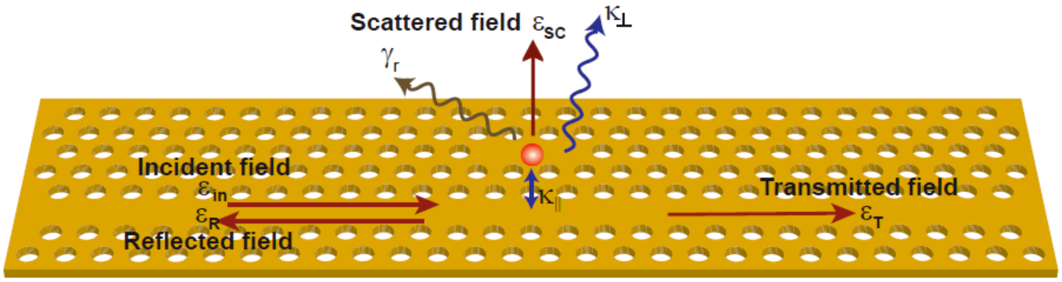

Figure 4 : Schematic of the cavity-waveguide-QD system showing the input modes and decay mechanisms

The incident field injected through the input grating is given by ε_{in}. The fields scattered, transmitted and reflected from the cavity are represented by ε_{sc}, ε_T and ε_R respectively. The QD has a radiative decay rate γ_r. The coupling rate between the cavity and the forward propagating mode of the waveguide is $\kappa_{||}$. Similarly, the backward propagating mode of the waveguide also a coupling rate of $\kappa_{||}$ into the waveguide. The cavity also has out-of-plane losses resulting in a perpendicular loss rate given by $\kappa_\perp$. Hence, the total decay rate of the cavity mode is $\kappa = 2\kappa_{||} + \kappa_\perp$.

We can access the cavity mode through the in-plane coupling between the cavity and waveguide. They can also be accessed through the out of plane leaky mode. In general the cavity excitation is performed through the waveguide to reduce the direct laser scatter from the cavity. Light is injected into the waveguide through the input coupler grating (Figure 5), which scatters photons into the waveguide. The light propagating in the waveguide then interacts with the cavity-QD system scattering light directly from the cavity. Some part of the signal is also directly transmitted through the waveguide and can be collected from the output coupler grating. Thus by monitoring the spectral emissions from the direct cavity scatter and from the output coupler, all the properties of the cavity-QD system can be established, at the same time giving us an opportunity to probe the system indirectly. This is particularly useful to realize optical interconnects and switches based on cavity-QD systems.

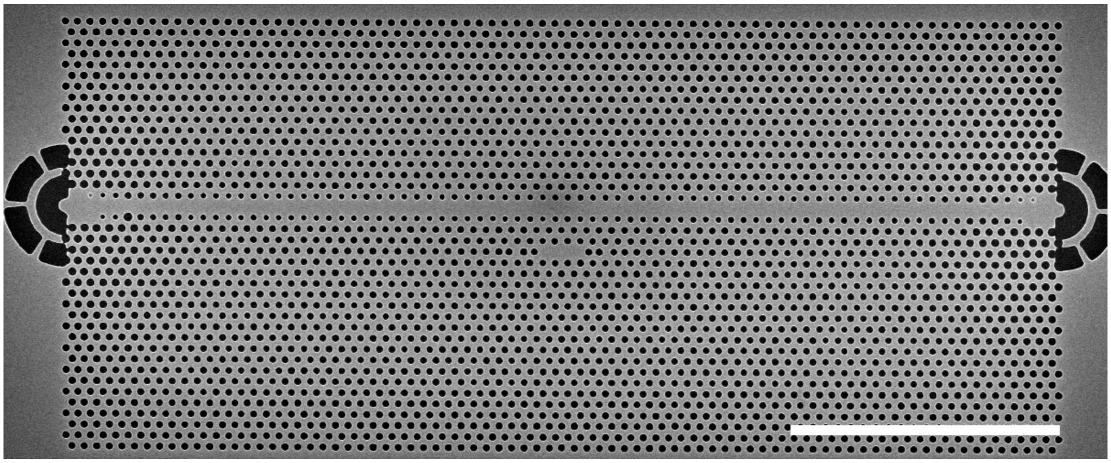

Figure 5 : SEM image of cavity-waveguide-QD system showing the input and output coupler gratings. The scale bar corresponds to 5μm.

1.6 Dipole Induced Transparency

The intensity of the scattered and transmitted light is given by the interaction between the cavity and waveguide. In addition to this, the intensities are also modified by the presence or absence of a quantum dot in the cavity. We can differentiate between the weak and strong coupling regimes to understand what happens to the scattered and transmitted intensities.

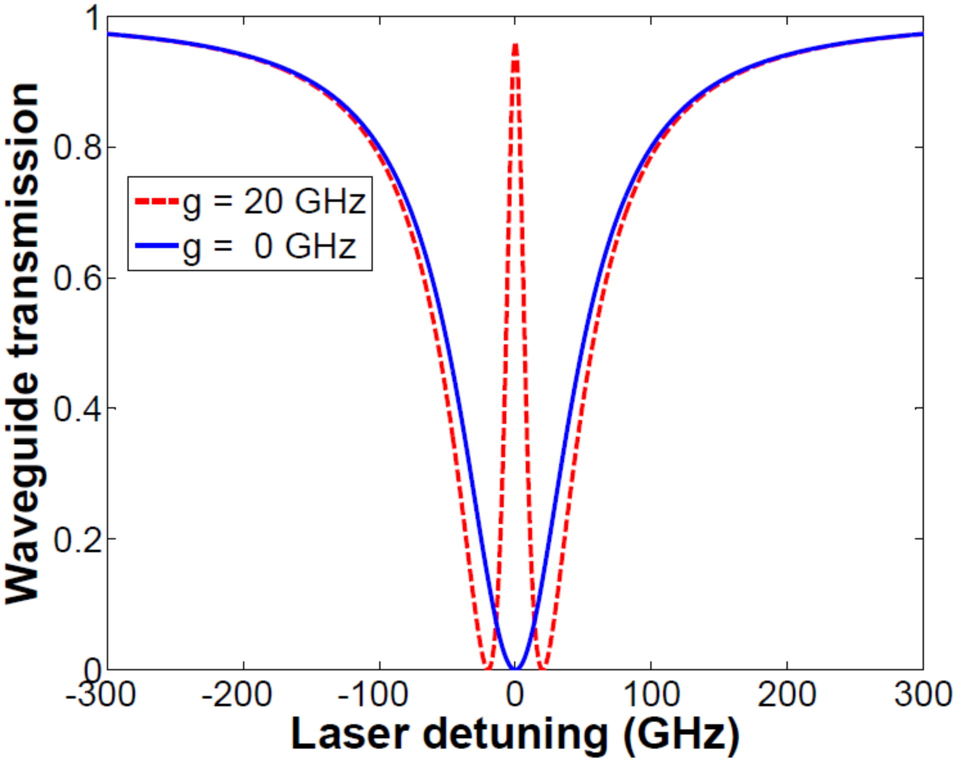

Figure 6 : Waveguide transmission with a QD in the cavity (red curve) and without a QD in the cavity (blue curve)

In strong coupling, the QD interacts with the cavity giving rise to the two polariton modes of the system. The system is no more in an independent cavity and QD state. An incoming photon resonant with the initial resonance of the cavity and QD, does not see the cavity because it is now in a superposition of a photonic and matter state. Thus, it passes straight through the waveguide without interacting with the cavity. This is called Dipole Induced Transparency because the presence of a QD in the cavity has made the waveguide transparent (Figure 6).

In the weak coupling regime, it is not directly evident what happens. The system exists in a cavity like and QD like state which are both driven together by the incoming photon. The destructive interference of the two driven cavity fields gives rise to Dipole Induced Transparency. This is equivalent to the destructive interference of an excited state of a 3 level atomic system in Electromagnetically Induced Transparency [24].

The intensity of the scattered and transmitted fields through the waveguide can be obtained through coupled mode theory. In the presence of a driving field ε_{in}, the Heisenberg equations of motion for the cavity field and dipole operator are given by

$$\begin{aligned}\frac{d\hat{\mathbf{b}}}{dt} &= -\left(i\Delta\omega + \frac{\kappa}{2}\right)\hat{\mathbf{b}} - \sqrt{\kappa_{\|}}\,\varepsilon_S - ig\hat{\sigma}_- \\ \frac{d\hat{\sigma}_-}{dt} &= -\left(i\left(\Delta\omega + \delta\right) + \frac{\gamma}{2}\right)\hat{\sigma}_- - ig\hat{\mathbf{b}}\end{aligned} \tag{1.6}$$

The equations of motion can be solved to obtain the transmitted field on resonance as

$$T = \left|1 - \frac{1}{1 + F_p}\right|^2 \tag{1.7}$$

where $F_p = 4g^2/\kappa\gamma$ is the Purcell Factor of the cavity. When the Purcell Factor is large, T=1 indicating that the waveguide is transparent.

1.7 Nonlinear switching of quantum dot absorption

The previous equations for the cavity field and dipole operator were obtained in the limit that the quantum dot predominantly exists in the ground state. This enables us to obtain a linear set of equations relating the two operators. In the presence of another field driving the cavity-QD system, two things are possible. If the driving field is resonant with the cavity and strong, the assumption that the QD predominantly exists in the ground state is no longer valid. We have to obtain a new set of equations for not only the cavity field and dipole operator, but also for the time evolution of population difference. In this case, the equations can be obtained to be

$$\begin{aligned}\frac{d\hat{\mathbf{b}}}{dt} &= -\left(i\omega_{cav} + \frac{\kappa}{2}\right)\hat{\mathbf{b}} - \sqrt{\kappa_{\|}}\,\varepsilon_S - ig\hat{\sigma}_- \\ \frac{d\hat{\sigma}_-}{dt} &= -\left(i\omega_{QD} + \frac{\gamma}{2}\right)\hat{\sigma}_- - ig\hat{\mathbf{b}} \\ \frac{d\hat{\sigma}_z}{dt} &= 2ig\left(\hat{\mathbf{b}}^\dagger\hat{\sigma}_- - \hat{\sigma}_+\hat{\mathbf{b}}\right) - \gamma\left(-1+\hat{\sigma}_z\right)\end{aligned} \tag{1.8}$$

It is apparent from the system of equations that it is no longer a linear system and an analytical solution is difficult to obtain. However, as a simple model we can assume that the population difference reaches a steady state and is a constant. The transmittivity of the cavity-QD system is then given by

$$T = \left|1 - \frac{1}{1-\sigma_z F_p}\right|^2 \tag{1.9}$$

The equation for *T* implies that when the QD is in the ground state, we get the same expression as earlier. If the QD is saturated i.e., then the transmittivity becomes 0. This happens because as the QD is saturated, light which was earlier prevented from entering the cavity can couple to the cavity and is reflected back into the reflected mode of the waveguide. This change in transmittivity of the cavity-QD system happens due to resonant nonlinearities of the QD.

When the driving laser is not resonant with the QD, two effects can occur simultaneously: the QD can be saturated due to the driving field off-resonantly and the QD undergoes a stark shift of its transition due to the off-resonant laser. Both these occur due to the enhanced nonlinearities of the QD within the cavity. It is not evident just by looking at Eqs 1.8 which nonlinearity dominates. In this work, we show that the main nonlinearity in a strongly coupled cavity-QD system driven off resonantly is the stark shift of the QD. We use this effect to shift the QD off cavity resonance with a pump laser and simultaneously probe the system with another weak laser to monitor the cavity response. Without the pump, we obtain the dressed states of the cavity-QD system as expected from a strongly coupled cavity-QD system. With the pump laser and the QD stark shifted, the probe monitors only the cavity response. The results of this work are given in chapter 4.

Chapter 2

Large optical stark shifts in quantum dots coupled to photonic crystal cavities

2.1 Overview

Photonic crystals are envisioned as an ideal platform for enhancing nonlinear optical effects to implement scalable all-optical signal processing. Nonlinearities in photonic crystals have already be used to demonstrate optical bistability [25,26], low-power all-optical switching [27,28], four wave mixing and second harmonic generation [29]. In addition, photonic crystal defect cavities provide extremely tight optical confinement in combination with high quality factors enabling large nonlinearities near the single photon level [10,30,31].

In this chapter, we investigate the optical Stark shift of a quantum dot (QD) strongly coupled to a photonic crystal cavity mode. When resonantly pumping the cavity we observe an extremely large optical Stark shift (20 GHz) for a resonantly detuned QD using low optical driving powers (60 μW). Stark shifts for the QD are observed directly by monitoring the emission of the QD through non-resonant energy transfer of the cavity field [32,33]. These Stark shifts are attained with extremely low cavity field energies of only 10 photons. The large optical Stark shifts demonstrated here provide a useful method for achieving low light-level nonlinear optics. They also provide an interesting approach for performing nonlinear spectroscopy on single QDs strongly coupled to optical microcavities. Experimental results are compared to theoretical predictions based on the solution to the full master equation and found to be in excellent agreement.

Measurements were performed on indium arsenide (InAs) QDs (with QD density 30 μm^{-2}) coupled to gallium arsenide (GaAs) photonic crystal structures. The cavity design used in this experiment was a three-hole linear defect (L3) cavity with three-hole tuning [34]. Figure 7a shows a scanning electron microscope image of a fabricated device. The parameter *a* was set to 240 nm and the hole diameter was set to 140 nm. The three holes at the edge of the cavity, labeled A, B, and C in the figure, were shifted by 0.176*a*, 0.024*a* and 0.176*a* respectively.

2.2 Cavity enhanced stark shift

The samples were first pumped with an 865 nm laser to excite the wetting layer and measure their fluorescence. The fluorescence spectrum from the sample taken at 14 K is shown in Figure 7b. The fluorescence exhibits a bright emission from the cavity mode along with emission from a nearby QD, as labeled in the figure. By fitting the cavity mode to a Lorentzian function we infer a quality factor (Q) of 7180. Figure 7c shows the spectrum as a function of sample temperature. As the sample is heated the resonance of the QD is red shifted and exhibits a clear anti-crossing behavior as it is tuned across the cavity mode, indicating that the cavity and QD are in the strong coupling regime. From the minimum separation point between the two lines, which occurs at 28 K, we calculate the cavity-QD coupling strength to be $g/(2\pi)$=12 GHz. Figure 7d shows the emission spectrum when the cavity is driven by a 300-kHz wavelength tunable laser diode tuned to resonance with the cavity mode instead of the 865 nm pump. Resonant excitation of the cavity results in clearly visible emission of the detuned strongly coupled QD [32,33,35,36]. Such non-resonant QD emission has been observed in previous works, and has been theoretically attributed to various energy transfer processes [37-41].

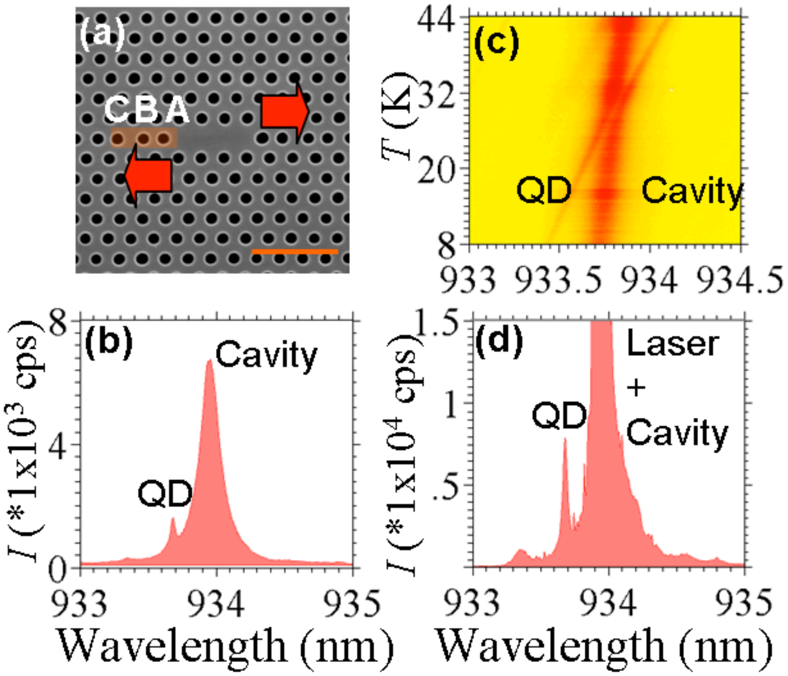

Figure 7 : (a) Scanning electron micrograph of fabricated L3 photonic crystal cavity. The three nearest holes at the edge of the cavity (labeled A, B, C) are shifted in the direction of the corresponding arrows. Scale bar: 1 μm. (b) Cavity-QD spectrum at low-power above-band (865 nm) laser excitation. (c) PL as a function of temperature showing strong coupling. (d) PL spectrum when the tunable excitation laser is resonant with the cavity. The strongly coupled QD line is labeled.

In Figure 8a we plot the cavity spectrum as a function of pump wavelength as the laser diode is tuned across the cavity mode. The measurements are taken at a temperature of 14 K, where the QD is blue shifted by 104 GHz from the cavity frequency, and the pump power is set to 50 μW. As the laser becomes resonant with the cavity mode, a clear emission-energy shift is observed due to optical Stark effect. The shift is only observed in a narrow spectral region near the cavity resonance, suggesting that the cavity plays a strong role in enhancing the field intensity to achieve a larger effect. When the laser is resonant with the peak of the cavity response, a maximum shift of 0.05 nm (18 GHz) is observed.

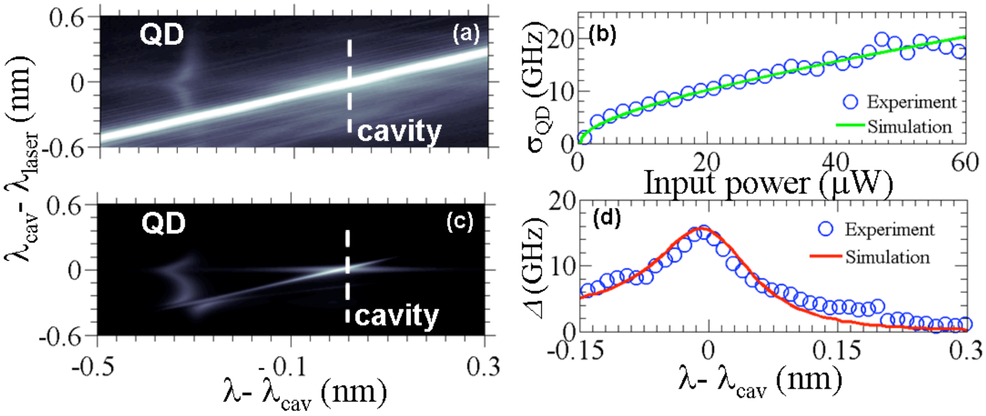

Figure 8 : (a) Cavity spectrum as a function of laser detuning from cavity (λ_{laser}-λ_c) at 14 K for a 50 μW pump power. (b) QD linewidth versus input power at the cavity mode resonance shown as blue circles, with fit from simulations shown by solid green line. (c) Calculated emission spectrum as a function of excitation wavelength. (d) Stark shift versus laser-cavity mode detuning for experimental data (circles) and theoretical calculations (solid line).

In addition to the wavelength shift, a clear broadening of the QD linewidth is observed with increasing excitation power. Such broadening has been previously demonstrated for a QD coupled to a photonic crystal cavity as well as bulk QDs, and has been attributed to increased stimulated emission of the QD in the presence of the incident field. Figure 8b plots the linewidth of the QD as a function of incident pump power, determined by fitting the measured QD spectrum to a Lorentzian function. We account for the finite spectrometer resolution by subtracting it out in quadrature using the relation σ_{QD}= $\sqrt{\sigma^2-\sigma_0^2}$, where σ is the measured linewidth, σ_{QD} is the actual QD linewidth, and σ_0 = 8.3 GHz is the spectrometer resolution. The linewidth is found to increase from 0.7 GHz to 20 GHz.

2.3 Estimation of coupling efficiency

The experimental results for the QD Stark shift and linewidth broadening can be compared to theoretical predictions based on a two-level quantum system coupled to a single mode optical resonator. Numerical calculations were performed by solving the full master equation using an open source quantum optics toolbox. Accurate comparisons of the numerical calculations and experimental results require an estimation of the experimental coupling efficiency of the excitation laser to the cavity mode. The power dependence of the QD linewidth provides us with a method to extract this coupling efficiency. We treat the coupling efficiency η as fitting parameter given by $\eta=P_{couple}/P_{inc}$, where P_{inc} is the experimentally measured incident power and P_{couple} is the amount of power that couples to the cavity mode. We first calculate the power spectrum of the cavity mode, defined as the Fourier transform of the two-time covariance function $\langle \mathbf{b}^{\dagger}(t+\tau)\mathbf{b}(t)\rangle$, as a function of P_{couple}. From the power spectrum we determine the center wavelength and linewidth of the QD using a Lorentzian fit. The parameter η is then optimized to achieve best agreement between simulation and theory.

For the simulations, we set the cavity decay rate to $\kappa/(2\pi)$=46 GHz (Q=7180) and the QD radiative lifetime and coherence time are set to $1/\gamma$=1 ns [22] and T_2 = 500 ps [42,43] respectively. The cavity-QD detuning is set to 104 GHz and the cavity-QD coupling strength is set to $g/(2\pi)$=12 GHz, as measured experimentally. The optimal cavity coupling efficiency is determined by numerical optimization to be η = 0.16%. Using this value, the simulated QD linewidth is plotted as a solid line in Figure 8b, and shows excellent agreement with the experimental data.

Having determined the coupling efficiency we can numerically investigate the Stark shift of the QD. In Figure 8c we plot the calculated cavity power spectrum as a function of excitation wavelength for the QD-cavity system assuming a 50 μW excitation power, where all simulation parameters are set to the same values used to calculate the linewidths in Figure 8b. Figure 8d plots both the experimentally measured QD center wavelengths (circles) obtained from the spectra in Figure 8a, along with the calculated center wavelength (solid line) obtained from Figure 8c. The calculated predictions are found to be in close agreement with the experimentally measured Stark shifts.

In order to ensure that what we are observing is due to optical Stark shift and not another anomalous effect, we change the sample temperature from 14 K to 40 K. At this temperature the QD is red-shifted from the cavity mode by 0.65 nm (230 GHz). Figure 9a plots the emission spectrum as a function of laser detuning at this temperature. When the laser is resonant with the cavity mode we once again observe a shift of the QD resonance, but this time the QD is red-shifted rather than blue-shifted due to the change of sign of the detuning, as one would expect from an optical Stark shift. Other effects, such as heating or production of free carriers would cause the QD to always shift in the same direction, while the Stark effect would cause them to shift away from the excitation laser as observed in the data. The calculated emission spectrum from the solution to the master equation is shown in Figure 9b, showing excellent agreement with our observations in Figure 9a. All simulation parameters were identical to those used in the calculations for Figure 8 except for the cavity-QD detuning, which was set to the new value of 230 GHz.

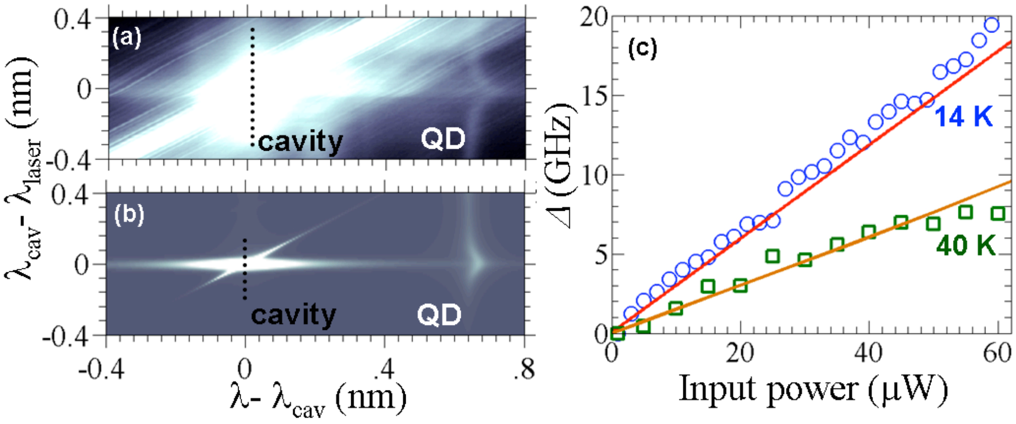

Figure 9 : (a) Cavity spectrum as a function of laser detuning from cavity (λ_{laser}-λ_c) at 40 K for a 50 μW pump power. (b) Calculated emission spectrum. (c) Stark-shift versus input power for QD at 14 K and 40 K when incident field is resonant with the cavity mode. Experimental data is shown by symbols, and simulated values are indicated by the solid lines.

We next investigate the pump power dependence of the QD Stark shift at both 14 K and 40 K sample temperature. The excitation laser is set to be resonant with the cavity mode, at the point of maximum Stark shift for the QD. The emission spectrum is then obtained as a function of incident laser power. For each spectrum, emission from the QD is fitted to a Lorentzian function to determine the center frequency. Figure 9c plots the magnitude of the measured Stark shifts for the QD at 14 K (circles) and 40 K (squares), corresponding to cavity-QD detunings of -0.3 nm and 0.65 nm respectively. The theoretically predicted shifts are also plotted using the same coupling efficiency of η=0.16% calculated from the linewidth data. In both cases, the shifts are found to increase linearly with incident field intensity. For a given pump power, a smaller Stark shift is observed at 0.65 nm detuning as compared to the -0.3 nm because the Stark shift is inversely proportional to detuning. This reduction in shift is also predicted by the theoretical model which is in good agreement with experimental data.

We fit the Stark shift to a linear function expressed as $\delta=\delta_p P$, where P is the incident power and δ_p= 0.9 pm/μW= 320 MHz/μW is the Stark shift per unit power at 14K. At 40 K, δ_p= 0.47 pm/μW= 166 MHz/μW. The excitation power can be expressed in terms of photon number in the cavity through the relation $n = P_{inc}\eta / \hbar\omega\kappa$. Using this relation the Stark shift can be written as $\delta=\delta_n n$ where δ_n=2.11 GHz/photon, indicating that the maximum Stark shift of 20 GHz observed is due to an average of approximately 10 photons in the cavity. Thus, this cavity-QD system provides nonlinearities near the single photon level.

2.4 Summary

In summary, we have shown that photonic crystal cavities can significantly enhance the optical Stark effect. Stark shifts as large as 20 GHz were observed with excitation powers of only 60 μW corresponding to a cavity energy of 10 photons. The excitation powers could be significantly reduced by improving our poor coupling efficiency (0.16%) using more directional cavity designs that enable efficient coupling from out-of-plane [44], better mode matching through planar structures [45], or fiber taper excitation [11]. The engineering of cavities with two modes may add additional flexibility where one cavity mode is used to achieve large optical stark shifts in order to tune a QD onto resonance with a second cavity mode, enabling possibilities for low light level integrated optical devices.

Chapter 3

Observation of strong coupling through transmission modification of a cavity-coupled photonic crystal waveguide

3.1 Introduction

We investigate strong coupling between a single quantum dot (QD) and photonic crystal cavity through transmission modification of an evanescently coupled waveguide. Strong coupling is observed through modification of both the cavity scattering spectrum and waveguide transmission. We achieve an overall *Q* of 5800 and an exciton-photon coupling strength of 21 GHz for this integrated cavity-waveguide structure. The transmission contrast for the bare cavity mode is measured to be 24%. These results represent important progress towards integrated cavity quantum electrodynamics using a planar photonic architecture.

Semiconductor quantum dots (QDs) coupled to photonic crystal structures provide a promising physical platform for studying strong atom-light interactions. Photonic crystal cavities exhibit both high quality factors (*Q*) and small mode volumes [34,46-49] enabling the study of cavity quantum electrodynamics in the strong coupling regime [22,31,50-52]. Strong coupling has important applications in the areas of nonlinear optics, quantum information processing [30,53], and spectroscopy [54].

Another advantage of photonic crystal structures is that they provide a method to integrate a large number of optical components in a compact device. Such devices can be used to implement complex photonic circuits where individual components communicate over optical channels. These channels can be realized using line-defect waveguides [34,55] that can transport light with low optical losses as well as slow group velocities creating strong interaction with other optical components over short distances [34,56]. By combining waveguides with optical cavities that are strongly coupled to quantum dots it becomes possible to create quantum interactions between the spatially separated QDs using light as a quantum interface [57-61], which forms the basis for universal quantum computation and quantum networking [62].

In order to take full advantage of the ability of photonic crystals to create integration we need to develop device structures where the cavity can be driven and can also emit into an integrated waveguide. Such devices have been routinely fabricated in passive silicon structures that do not contain QDs and used to probe the cavity properties [34,63]. To incorporate quantum dots, however, it is necessary to work in gallium arsenide (GaAs) material systems which suffer from higher losses and lower cavity Q, particularly in the near infrared wavelengths. The introduction of the waveguide causes a critical reduction in the resonator Q due to the new channel for optical losses, making it difficult to achieve the strong coupling regime. For this reason, previous investigations of coupled cavity-QD systems through planar waveguide transmission have been performed in the weak coupling regime [64].

In this chapter, we study strong coupling between an indium arsenide (InAs) QD and a photonic crystal cavity using a planar waveguide transmission measurement rather than photoluminescence. We design and fabricate a photonic crystal structure composed of a cavity evanescently coupled to a row defect waveguide, with a single QD resonantly coupled to the cavity mode. The cavity has a sufficiently high cavity Q to achieve strong coupling, while also maintaining sufficiently strong coupling to the waveguide to achieve a 24% transmission contrast. Strong coupling is observed by driving the cavity-QD system near resonance through the waveguide and measuring the waveguide transmission and cavity scattering spectrum. This approach provides a simple way to separate the pump and cavity signal in order to coherently measure the strongly coupled system. The results represent an important step towards development of integrated planar device structures where waveguides are used to create an optical interface between spatially separated QDs.

3.2 Device Design

The device structure used in this work is shown schematically in Figure 10a. The device is comprised of a photonic crystal cavity evanescently coupled to a row defect waveguide. The cavity design is a three-hole linear defect (L3) cavity with three-hole tuning [34]. As shown in Fig. 10a, the holes A, B, and C adjacent to the cavity are shifted by 0.176*a*, 0.024*a* and 0.176*a* respectively, where *a* is the lattice constant, in order to improve the overall *Q*. The lattice parameter *a* is set to be 240 nm, the diameter of the air holes is set to 140 nm, and the photonic crystal slab thickness is set to be 160 nm. The line defect waveguide is formed by removing a row of holes below the cavity.

The dispersion diagram for the transverse electric (TE) modes of the bare photonic crystal waveguide (no cavity) is shown in Figure 10b. Modes are plotted as a function of the in-plane crystal momentum k_x (in units of a/π) and mode frequency (in units of a/λ), while the solid red line represents the light line of the slab waveguide. The waveguide dispersion was calculated using finite difference time domain (FDTD) simulations (Lumerical FDTD). The band structure exhibits a TE bandgap between ω = 0.232 and 0.287. Below the light line, the even waveguide mode has a passband in the frequency range of $\omega \in [0.241, 0.262]$. At the edge of the Brillioun zone, the waveguide exhibits a slow group velocity region at a frequency of ω = 0.241. In order to couple the cavity strongly to the waveguide mode, it is important that the cavity resonance overlaps with the slow group velocity region of the waveguide, where the enhanced waveguide density of states can significantly increase the coupling between the two systems [56]. To achieve this condition, the size of the holes above and below the row defect is reduced by 4% relative to the other holes in the photonic crystal. Reducing these hole sizes serves to pull the band edge of the waveguide to lower energies so that it better overlaps with the cavity resonance. Using this device design we calculate the properties of the cavity by placing a point source dipole emitter with a broad spectral response at the high electrical field region of the cavity mode. From this calculation we determine the theoretical cavity Q to be 10,000, and the cavity resonance frequency to be 0.245. Figure 10c shows the calculated $\mathbf{H}_z$ mode profile of the cavity, which exhibits a clear coupling to the waveguide mode.

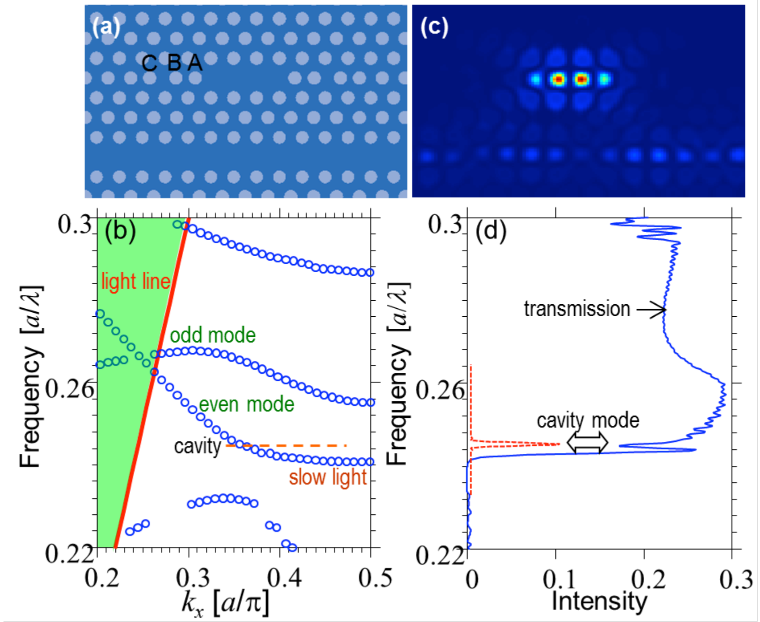

Figure 10 : (a) Schematic of simulated structure. (b) Simulated photonic band structure for photonic crystal waveguide with waveguide-edge holes reduced by 4%.

The light line is shown by solid red line. (c) Field profile ($\mathbf{H}_z$) of computed cavity-field mode, shown over the simulation region in (a). (d) Simulated transmission spectrum (solid blue line), along with the spectral response of the fundamental cavity mode (dashed red line) computed using a broadband source inside the cavity.

Figure 10d shows the calculated transmission of the waveguide (solid blue line) in the device structure shown in Fig. 10a as a function of optical frequency in units of a/λ. The waveguide transmission is calculated by placing a broadband point source at the mid-plane of the photonic crystal slab at one end of the waveguide and calculating the transmitted power at the other end. The transmission of the waveguide exhibits a broad pass band that cuts off sharply at a normalized frequency of 0.241, as expected from the waveguide dispersion diagram. The sharp cutoff denotes the waveguide stop band. An anti-resonance in the transmission spectrum is observed at the cavity frequency of 0.245 with a corresponding 29% reduction in transmission. The anti-resonance is due to both reflection and out-of-plane scattering from the cavity mode. In addition to the waveguide transmission, we also plot the calculated cavity spectral response when excited by a broadband point dipole source (red dashed line). These spectra show that the cavity spectrum is in agreement with the anti-resonance of the waveguide transmission, and also overlaps the slow group velocity regime of the waveguide mode.

3.3 Fabrication

The initial wafer for the device fabrication, grown by molecular-beam epitaxy, was composed of a 160-nm GaAs membrane with an InAs QD layer grown at the center (with QD density of approximately 10 μm^{-2}), on a 1-μm thick sacrificial layer of aluminum gallium arsenide ($Al_{0.78}Ga_{0.22}As$). Photonic crystals were defined on the

GaAs membrane using electron-beam lithography, followed by chlorine-based inductively coupled plasma dry etching. Selective wet etching was then used to remove the sacrificial AlGaAs layer, resulting in a free-standing GaAs membrane. Figure 11a shows a scanning electron micrograph (SEM) of a fabricated device, where the design parameters are identical to those simulated in Section 3.2. The total device length was set to 80*a*, which is sufficiently long to optically isolate the cavity from the input and output facets of the device. In order to inject and collect light from the waveguide in the out-of-plane direction, we employ grating couplers at the two ends of the waveguide, as originally proposed and demonstrated by Faraon *et. al* [64]. These couplers have been shown to couple as much as 50% of the light in the out-of-plane direction. A close-up of the cavity interaction region and grating coupler are shown in panels b and c respectively.

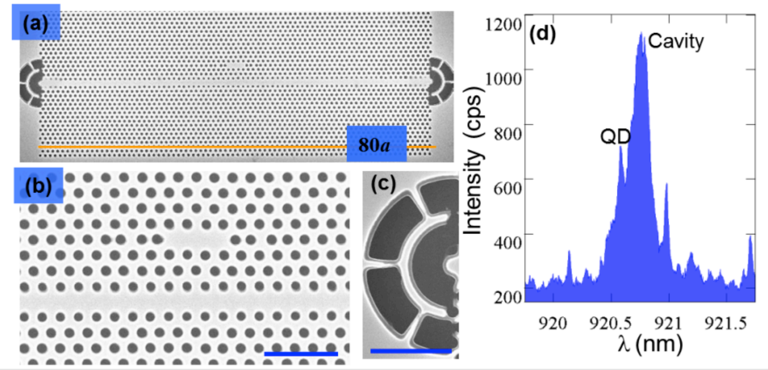

Figure 11 : (a) Scanning electron micrograph showing a typical fabricated device. (b) Closeup of the cavity-waveguide region, showing the design adjustments for optimal performance. (c) Closeup of the input grating coupler. Scale bars in (b) & (c) correspond to 1 μm. (d) Low power (5 μW) above-band excitation of the cavity.

3.4 Experimental Setup and Device Characterization

The sample was mounted in a liquid helium cryostat with temperature varying between 15 K and 35 K. Three light sources were used in the experiments. A Ti:Sapphire laser operating in continuous wave mode was used for above-band out-of-plane excitation in order to measure the photoluminescence properties of the device. A broadband light emitting diode operating between 900-1000 nm was used to investigate the transmission and scattering spectrum of the device in the weak field limit by exciting through the input grating and observing radiation at the cavity or at the outcoupler at low incident photon flux. Finally, a tunable external cavity diode laser (New Focus Velocity) enabled us to probe the system with high power narrowband field for power-dependent near-resonant excitation experiments. A polarization setup consisting of a half waveplate and polarizing beamsplitter was used to match the excitation source with the polarization of the waveguide mode. Emission was collected by a confocal microscope setup using a 0.7 NA objective lens, followed by spatial filtering to isolate the scatter from either the cavity or output coupler. The collected emission was then measured by a grating spectrometer with a wavelength resolution of 0.02 nm.

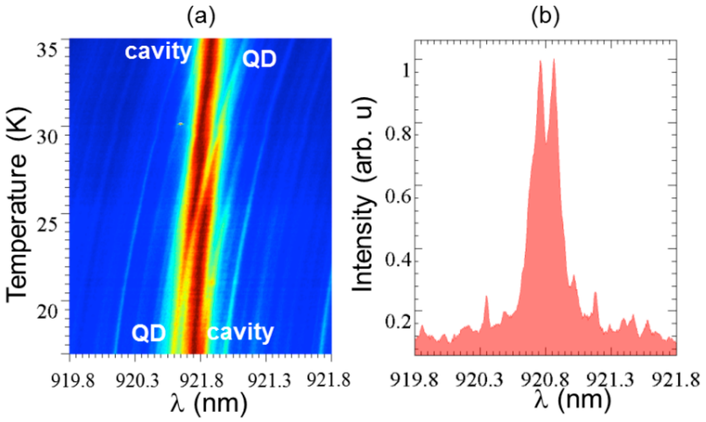

Figure 12 : (a) Temperature scan of the cavity QD system using above-band (780 nm) excitation showing an anti-crossing around 27 K due to strong coupling. (b) Cavity spectrum at the strong coupling point using low power excitation, with a measured splitting of 0.09 nm between the polariton peaks.

Devices were initially characterized using above-band (780 nm) excitation. Figure 11d shows the photoluminescence spectrum of the cavity when directly excited by the above-band pump. The spectrum shows a bright emission peak from the cavity mode at 920 nm, along with several nearby QDs. The QD we focus on in this work is labeled in the spectrum. By fitting the cavity to a Lorentzian function we determine the cavity Q to be 5800, which corresponds to a cavity decay rate of κ=56 GHz. In order to tune the QD onto the cavity resonance the temperature of the device was tuned from 17 K to 35 K. The photoluminescence spectrum as a function of sample temperature is show in Figure 12a. Near 27 K, the QD becomes resonant with the cavity mode resulting in significant enhancement of the cavity emission as well as a clear anti-crossing behavior, indicating that the QD and cavity are in the strong coupling regime. The minimum separation between the two polariton modes of the strongly coupled system occurs at a temperature of 27K. The cavity spectrum at this temperature is plotted in Figure 12b. This spectrum is fit to a double Lorentzian spectrum in order to calculate the vacuum Rabi splitting (VRS) which is given by 0.09 nm and corresponds to a frequency splitting of Δ=31.5 GHz. From the vacuum Rabi splitting we calculate the QD-cavity coupling strength g using the relation :

$$2g \approx \sqrt{\Delta^2 + (\kappa - \gamma)^2 / 4} \tag{3.1}$$

where $\gamma/2\pi = 0.1$ GHz is the QD spontaneous emission rate. From the above equation we determine that g=21 GHz, which satisfies the strong coupling condition $g > \kappa/4$ for κ=56 GHz.

3.5 Weak field transmission and scattering measurements

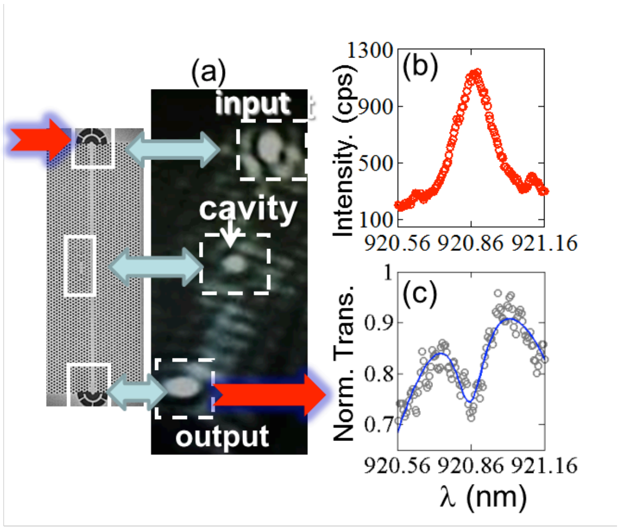

Figure 13 : (a) CCD image of the device under laser excitation showing radiation at the input and output gratings as well as the cavity region when the laser is tuned to the resonance of the cavity mode. An SEM of the typical device is also shown on the left for reference. (b) Photoluminescence spectrum of the cavity-QD system when the QD is detuned by 0.3 nm from the cavity mode. (c) Transmission measured at the same QD-cavity detuning condition as in (b) showing a dip corresponding to the cavity transmission.

Having characterized the photoluminescence properties of the cavity, we next probe the strongly coupled cavity-QD system through the scattering spectrum of the cavity and transmission spectrum of the waveguide by injecting light into the waveguide through the input grating coupler. Upon irradiating the input grating with a focused light source a clear radiation was observed from both the cavity and the output coupler, as shown in Figure 13a. This figure shows a CCD image of the device when the input coupler is excited by a narrowband laser source that is tuned to be resonant with the cavity, along with an SEM image of the fabricated structure as a reference. The scattered spot from the cavity and output coupler are indicated, and can be isolated by spatial filtering using a small aperture.

We first considered the emission from the output coupler, which is proportional to the light intensity transmitted through the waveguide, when the QD is not coupled to the cavity. To decouple the two systems we set the sample temperature to 14K where the QD is detuned from the cavity by 0.3 nm. This detuning is larger than the cavity linewidth so the system behaves as a bare cavity evanescently coupled to a waveguide. A PL spectrum obtained using high power above-band excitation at this temperature is shown in Figure 13b. At these pump powers all QDs saturate and enabling us to clearly isolate the cavity emission which is centered at a wavelength of 920.86 nm.

Figure 13c shows the normalized transmission spectrum of the waveguide, observed by now focusing a broadband LED on the input coupler and collecting emission only from the output coupler using a small aperture. The spectrum of the transmitted light is measured using the grating spectrometer. The transmission of the waveguide was found to significantly vary with wavelength due to the spectral response of the grating couplers as well as Fabry-Perot fringing effects caused by multiple reflections between the two couplers and the cavity. At the cavity resonance wavelength of 920.86 nm, we observe an anti-resonance in the transmission spectrum superimposed on the broader spectral response of the waveguide. This anti-resonance is due to the evanescent coupling of the cavity mode to the waveguide.

The transmitter power spectrum, denoted $S_T(\omega)$, can be compared to the theoretically predicted value based on cavity input-output formalism [65], which is given by

$$S_T(\omega) = |\varepsilon(\omega)|^2 \left| \frac{i2\Delta_c + \kappa(1-r_0)}{i2\Delta_c + \kappa} \right|^2 \qquad (3.2)$$

Here, $r_0 = 2\kappa_{||}/\kappa$ is the reflectivity of the bare cavity (no QD) on resonance where $\kappa_{||}$ is the decay rate of the cavity into the forward and backward propagating modes of the waveguide, $\Delta_c = \omega - \omega_c$ where ω and ω_c are the driving field frequency and cavity resonant frequency respectively, and $\varepsilon(\omega)$ is the amplitude of the incident driving field. In order to fit the data to the spectrum described in Eq. 3.2, we need to know the frequency dependence of the input field $\varepsilon(\omega)$, which is very difficult to characterize because it depends on the unknown spectral response of the gratings and Fabry-Perot fringing caused by multiple reflections. To attain an accurate measurement of this response we would need to remove the cavity-QD system and characterize the waveguide and grating couplers alone, something we cannot do. Instead, we perform a second order Taylor series expansion of the field given by $|\varepsilon(\omega)|^2 = c_0 + c_1(\omega - \omega_c) + c_2(\omega - \omega_c)^2$. The coefficients c_0, c_1, and c_2 are treated as fitting parameters to attain the best match to the experimental data.

Using r_0 and κ as additional fitting parameters, we fit the experimental transmission spectrum to Eq 3.2. The best fit, shown as a solid line in Fig. 13c, is attained for r_0=0.12 and κ=56 GHz. From these parameters, we calculate $\kappa_{||}$ to be 3.4 GHz corresponding to $Q_{||}$=95800. This high value for the planar Q suggests that we are operating in the undercoupled regime. The transmission of the waveguide on resonance is given by $T_c(\omega_c)=(1- r_0)^2=0.77$, in close agreement with the theoretical value of 0.71 calculated from FDTD simulations as described in section 3.2.

The sample temperature was next set to 27 K in order to tune the QD onto resonance with the cavity mode. The broadband diode was once again focused onto the input coupler, and Fig. 14a shows the spectrum from the light directly scattered out of plane by the cavity. This spectrum was obtained by spatially filtering emission scattered from the cavity region and measuring the spectrum using the grating spectrometer. The scattered power spectrum is plotted as a function of detuning between the incident field wavelength λ and the cavity resonant wavelength λ_c. Near the cavity resonance, significant enhancement of the scattered power is observed. However, instead of a single Lorentzian line, a doublet feature is observed in the cavity-radiated emission due to interaction with the strongly coupled QD. The central dip in the normalized scattering spectrum exhibits a peak-to-dip contrast of 49%, which is higher than the contrast of the photoluminescence spectrum at low excitation powers, measured to be 37%. This increased contrast is a manifestation of destructive interference between polariton modes.

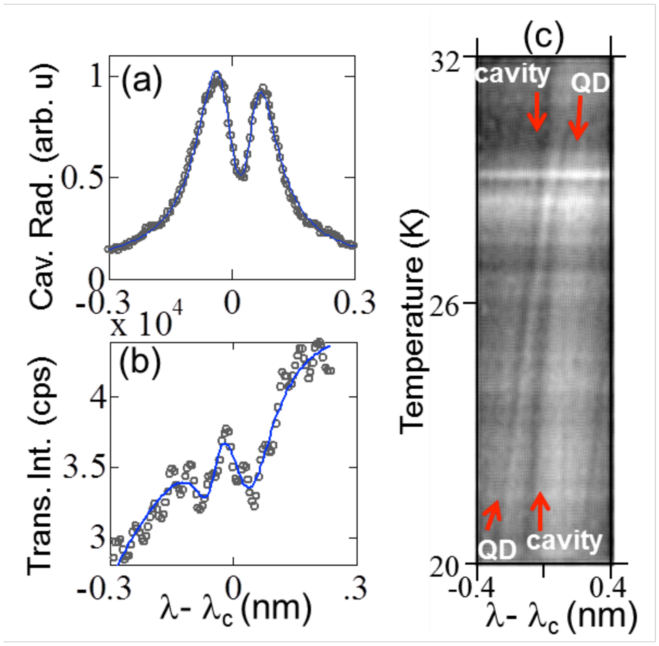

Figure 14 : (a) Scattering spectrum for QD-cavity system in the weak-field condition at 27 K. (b) Transmission spectrum of the cavity-QD system on resonance at 27 K. (c) Transmission measured as a function of temperature between 20- and 32K showing an anti-crossing between the anti-resonances corresponding to the two polaritons.

The measured scattering spectrum can be compared to the theoretical predictions based on a two-level atomic system coupled to a single cavity. The scattering spectrum for such a system has been previously investigated in several works [66-68] under the approximation that the atomic system only undergoes decay, but does not experience dephasing. Such approximation is unrealistic for InAs QDs where the coherence time can be significantly shorter than the excited state lifetime [69]. In the presence of dephasing, it has been shown that one cannot simply replace the dipole decay rate, denoted γ_a, by the standard semi-classical expression $\gamma_a=(\gamma_r+\gamma_{nr})/2+1/T_2$

where γ_r is the radiative decay rate, γ_{nr} is the non-radiative decay rate, and T_2 is the coherence time [70]. The correct expression for the scattered power spectrum is given by $S_S(\omega) = \eta\kappa_\perp n$ where $\kappa_\perp$ is the out-of-plane cavity decay rate, η is the photon detection efficiency which accounts for the collection optics as well as detector quantum efficiency, and n is the cavity photon number given by:

$$n = \frac{4}{4\Delta_c^2 + \kappa^2}\left(\frac{g^2|\rho_{21}|^2}{\Gamma}\left[\gamma_a + \frac{2g^2\kappa}{4\Delta_c^2 + \kappa}\right] + 2g\sqrt{\kappa}\,\mathrm{Im}\left[\varepsilon^*\rho_{21}\right] + \kappa|\varepsilon|^2\right) \qquad (3.3)$$

In the above equation γ_a is the previously defined semi-classical dipole decay rate, and $\Gamma = \gamma_r + \gamma_{nr} + 4g^2\kappa/\left(\kappa^2 + 4\delta^2\right)$ is the modified QD decay rate where $\delta = \omega_a - \omega_c$ and ω_a is the QD resonant frequency. The term ρ_{21} is the off diagonal dipole term of the reduced density matrix for the QD which, in the weak field limit, is given by

$$\rho_{21} = \frac{\Omega(i\Delta_c + \kappa/2)}{(i\Delta_a + \gamma_a)(i\Delta_c + \kappa/2) + g^2} \qquad (3.4)$$

where $\Delta_a = \omega - \omega_a$, and $\Omega = -ig\sqrt{\kappa}\varepsilon/\left(i\Delta_c + \kappa/2\right)$. We note that because $\rho_{21} \propto \varepsilon$ we have $n \propto |\varepsilon|^2$ as expected in the weak excitation limit where the system is a linear scatterer and so the scattering rate should be proportional to the input photon flux.

We fit the theoretical model given in Eq. 3.3 to the experimental data shown in Figure 14a. The fitting parameters used were g, γ_a, δ, and $s_0 = \eta\kappa_\perp|\varepsilon|^2$, which is the peak scattering rate with no QD. We also treat the spectrometer background level as an additional fitting parameter. The solid line plots the best fit curve to the data, which is attained for the parameter values $g = 17$ GHz, $\gamma_a = 6.3$ GHz, and $\delta = 3.7$GHz.

We next consider the transmission of the waveguide by collecting light at the output port, as shown in Figure 14b. The transmitted spectrum exhibits an anti-resonant doublet feature, where the minima of the anti-resonances correspond to the peak values of the corresponding resonances in Figure 14a. This doublet corresponds to mutual scattering from the two polariton modes of the cavity, and is the signature of strong coupling observed through the waveguide transmission.

The experimental measurements for transmission can be compared to the theoretical values which can be also be calculated using cavity input-output formalism. The input-output relation for the cavity is given by $\mathbf{a}_{\mathbf{out}} = \varepsilon(\omega) - \sqrt{r_0\kappa/2}\mathbf{a}$ where ε is once again the coherent input driving field amplitude, $\mathbf{a}_{\mathbf{out}}$ is the bosonic flux operator for the transmitted field, $\mathbf{a}$ is the bosonic annihilation operator for the cavity mode, and, as before, $r_0=2\kappa_{||}/\kappa$ is the reflectivity of the bare cavity (no QD) on resonance where $\kappa_{||}$ is the decay rate of the cavity into the forward and backward propagating modes of the waveguide. The transmitted flux is given by $\left\langle \mathbf{a}^{\dagger}_{\mathbf{out}}\mathbf{a}_{\mathbf{out}} \right\rangle = |\varepsilon(\omega)|^2 - \sqrt{2r_0\kappa}\,\mathrm{Re}\{\varepsilon^*(\omega)A\} + r_0\kappa n/2$, where $A = \langle \mathbf{a} \rangle$ and n is the cavity photon number given in Eq. 3.3. In the weak field limit we have

$$A = \frac{\sqrt{\kappa}\varepsilon(\omega)(i\Delta_a + \gamma_a)}{(i\Delta_c + \kappa/2)(i\Delta_a + \gamma_a) + g^2} \tag{3.5}$$

We again note that in the weak field limit the transmitted power is proportional to $|\varepsilon(\omega)|^2$. As before, we perform a second order Taylor series expansion of the incident field power spectrum given by $|\varepsilon(\omega)|^2 = c_0 + c_1(\omega - \omega_c) + c_2(\omega - \omega_c)^2$. The coefficients c_0, c_1, and c_2 are treated as fitting parameters to attain the best match to the experimental data.

The fitting parameters used to compare experiment to theory are the expansion coefficients for the background, along with g, δ, γ_a, ω_c, and r_0. The solid line in Fig. 14b shows the best fit curve for the data, which is attained for g=15.8 GHz, δ=-15.2 GHz, γ_a=7.2 GHz, and r_0=0.12. These numbers are consistent with the fitting for the scattered field, and the previously determined parameters using the bare cavity transmission. We note that in the transmission measurement the QD was slightly detuned from the cavity mode, but this detuning was small compared to the cavity linewidth.

In Figure 14c, we show experimental data from a temperature tuning experiment in which the strongly coupled QD was tuned across the cavity resonance. Here, the transmission of the waveguide was recorded at each temperature using the broadband LED source at the input coupler. At each temperature two anti-resonances can be observed, which correspond to the two polariton modes of the cavity-QD system. As the QD is tuned across the cavity frequency a clear anti-crossing can once again be observed as was shown in Figure 12a, but this time in the anti-resonances of the waveguide transmission. The minimum splitting between the two anti resonances, achieved at 27 K, is given by 0.1 nm which is consistent with values obtained from the cavity photoluminescence.

3.6 Waveguide transmission in the strong field limit

The quantum-optical state of the cavity-QD system is strongly intensity dependent. In the weak excitation regime (Fig. 14), the QD predominantly occupies the ground state, and the laser scan in the cavity radiation and transmission measurements show the dressed polariton states. As the excitation power is increased, the exciton becomes saturated and decouples from the cavity. In this limit the power spectrum of the scattered and transmitted fields are expected to approach those of the bare cavity mode.

To perform high power measurements, we measure the cavity spectrum using a tunable narrowband external cavity laser diode. This excitation source can inject high field intensity into a narrow spectral bandwidth in order to strongly excite the QD. The cavity spectrum is obtained by pumping the input coupler and sweeping the laser diode frequency. At each frequency the amount of scattered light is recorded. Fig. 15a shows a result of a wavelength sweep for several different excitation powers (5 μW, 60 μW and 90 μW from bottom to top) where we collect the scatter directly from the cavity. At a low pump power of 5 μW the spectrum is nearly identical to the low power spectrum attained by the broadband LED, shown in Fig. 14a. As the pump power is increased to 60 μW the contrast of the central dip is reduced, while at an even higher pump power of 100 μW the central dip is almost completely absent from the spectrum.

A similar behavior can be observed in the waveguide transmission. Fig. 15b and 15c plot the light intensity scattered from the output coupler for two different laser powers. Panel b plots the low power spectrum when the pump is set to 5 μW, while panel c plots the high power spectrum taken with a pump power of 125 μW. Once again, at low powers the transmission exhibits two anti-resonances corresponding to the two polaritons. The data is plotted along with the theoretical fit attained by setting g=15.8 GHz and γ_a=7.2 GHz, the values obtained by fitting the data in Fig. 14c, while leaving the remaining fitting parameters free. At high power a single resonance corresponding to the cavity mode is observed due to QD saturation. The high power data is also plotted along with the fit, where best fit value for r_0 is found to be 0.1, consistent with the values obtained from the data in Fig. 13c.

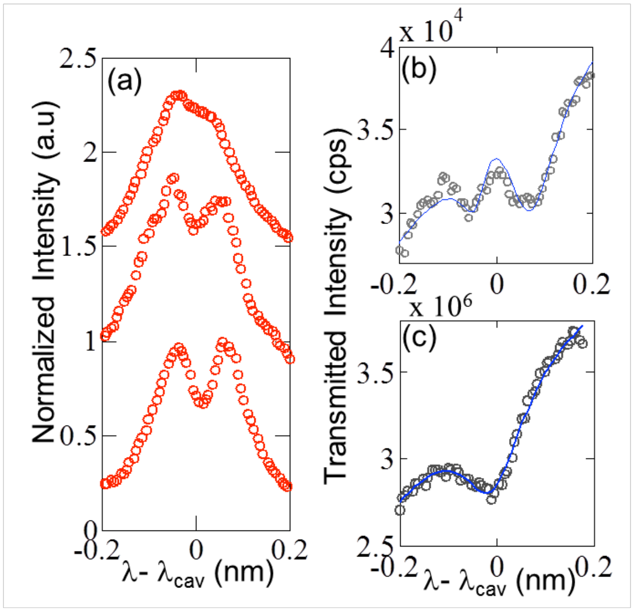

Figure 15 : (a) Cavity emission for increasing excitation powers of the input laser with incident powers, from top to bottom, of 100 μW, 60 μW, and 5 μW. (b) Waveguide transmission measurement at 5 μW. (c) Waveguide transmission at 125 μW. In (b) and (c) fitting curves are shown using solid lines, while the experimental data is shown using circles.

3.7 Summary

In conclusion, we have successfully demonstrated a fully integrated cavity waveguide system where the cavity mode is strongly coupled to a QD. The quantum state of the system is measured using a transmission setup where both input and collection occur away from the cavity region. A 24% reduction in waveguide transmission was observed on cavity resonance due to evanescent interaction between the waveguide and cavity modes. Strong coupling was observed through modification of the transmission of the waveguide resulting in a double anti-resonance at the locations of the two polariton energies. The waveguide transmission was also found to be extremely intensity dependent as expected due to saturation of the QD absorption. Improved devices with better contrast could be attained by using designs that achieve better overlap between the cavity and waveguide mode [71]. These results represent an important step towards complex integrated planar devices where interactions between multiple cavity-QD systems can be achieved using optical channels.

Chapter 4

An all-optical transistor with attojoule energy dissipation using a single quantum dot

4.1 All-optical transistor

All-optical transistors are expected to play an important role in future low power ultra-high bandwidth signal processing [1]. The majority of optical transistors to date achieve optical switching using weak atom-light interactions from a large ensemble of atomic systems [2-7], resulting in high power dissipation and large device size [8]. Here we demonstrate an ultra-compact all-optical transistor with only 14 attojoules of energy dissipation where the optical switching is implemented by a single atom-like system, a semiconductor quantum dot (QD). The device is composed of a QD coupled to a photonic crystal cavity-waveguide optical circuit, where the photonic crystal provides strong light localization creating extremely large optical nonlinearities, even with a single QD [9-12]. The energy dissipation of the demonstrated device is two orders of magnitude lower than previously reported photonic crystal transistors [13,14], and nearly an order of magnitude lower than electrical CMOS transistors [15]. We demonstrate switching speeds of up to 8.4 GHz, providing the potential for high bandwidth and low power consumption optical signal processing in an ultra-compact chip-based device.

The demand for faster and more energy efficient information technology has experienced a significant increase over the past few years. All-optical transistors are considered to be an important alternative for increasing information bandwidth. These devices enable optical signal processing without having to perform transduction to electrical current. A variety of all optical switching devices have been demonstrated using various device structures such as semiconductor quantum wells [2,3], semiconductor optical amplifiers [4-6], and nonlinear parametric processes [7]. These devices typically rely on weak nonlinearities from a large ensemble of atomic systems, and therefore require large device sizes and dissipate large powers [8]. Photonic crystals (PCs) have been shown as an effective method for significantly reducing optical device sizes [72,73]. PC optical transistors have been demonstrated using free carrier absorption and laser gain modulation, but these devices still operate in the 0.6-15 fJ range [13,14], well above the 0.1 fJ energy dissipation levels of typical CMOS electrical transistors [15].

Here we demonstrate all-optical transistor with only 14 attojoules of switching energy, where the nonlinearity is implemented by a single semiconductor quantum dot (QD) coupled to a planar photonic crystal cavity-waveguide circuit. Fig. 16a illustrates the device and operation principle. The device is composed of a photonic crystal cavity-waveguide structure, with a single quantum dot (QD) strongly coupled to the cavity. The signal beam and control beam, which are spectrally detuned, propagate together in the waveguide. The control beam determines whether the signal will be preferentially transmitted through the waveguide or scattered by the cavity. This switching is induced by the strong coupling between the QD and the photonic crystal cavity, which enables large optical nonlinearities at extremely low optical powers [12,57,64,74,75].

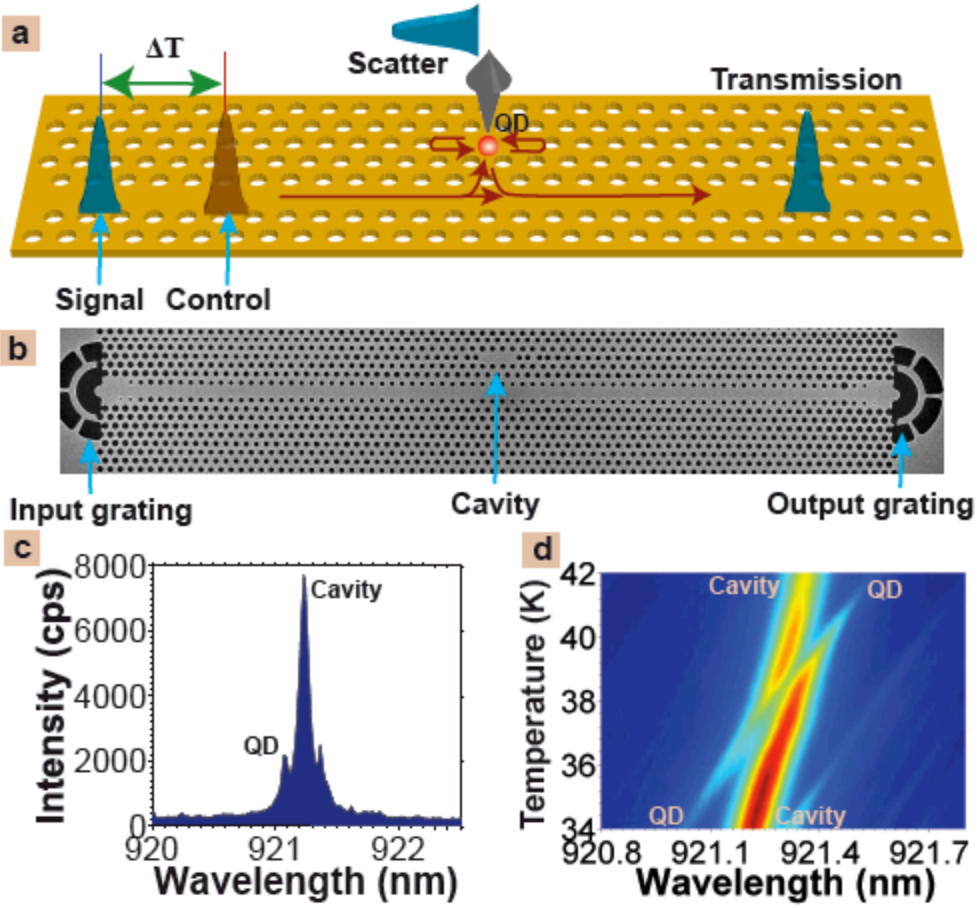

Figure 16: Description of all-optical switching device. (a) Schematic of cavity-waveguide system. The signal and control beam propagate through the waveguide with tunable time delay ΔT. (b) Scanning electron micrograph showing the fabricated device. An input grating enables light to be injected into the waveguide from the out-of-plane direction. The signal can be collected from the out-of-plane scatter of either the cavity or output grating. (c) Low power PL measurement of cavity, which exhibits an emission peak from the cavity along with several other weaker peaks corresponding to individual QDs. The QD studied in this chapter is labeled. (d) Cavity PL as a function of sample temperature which shows an anti-crossing between the QD and cavity emission, indicating strong coupling.

A scanning electron micrograph (SEM) image of a fabricated device is shown in Figure 16b. The initial wafer for the device fabrication, grown by molecular-beam epitaxy, was composed of a 160-nm GaAs membrane with an InAs QD layer grown at the center (with QD density of approximately 10 μm^{-2}), on a 1-μm thick sacrificial layer of aluminum gallium arsenide ($Al_{0.78}Ga_{0.22}As$). Photonic crystals were defined on the GaAs membrane using electron-beam lithography, followed by chlorine-based inductively coupled plasma dry etching. Selective wet etching was then used to remove the sacrificial AlGaAs layer, resulting in a free-standing GaAs membrane. The total device length was set to 80a, which is sufficiently long to optically isolate the cavity from the input and output facets of the device. In order to inject and collect light from the waveguide in the out-of-plane direction, we employ grating couplers at the two ends of the waveguide. The signal beam and control pulse are injected into the waveguide using a grating coupler [64], and drive the cavity evanescently. The signal pulse is collected either directly from the cavity (direct cavity scatter) or from the output coupler (transmitted waveguide signal) by spatial filtering.

4.2 Estimation of system parameters

The photoluminescence (PL) of the cavity is measured by exciting with a continuous wave pump laser at 780 nm wavelength, where both excitation and collection are performed in the out-of-plane direction. Figure 16c shows the cavity PL which exhibits an emission peak for the cavity mode, along with additional emission peaks for several QDs that are coupled to the cavity. The QD used for all measurements is labeled in the Figure 16c. By fitting the cavity mode to a Lorentzian, we estimate the cavity energy decay rate $\kappa/2\pi$ to be 28.0 GHz (Q~11900). Figure 16d shows the photoluminescence as a function of device temperature. As the temperature is increased, the QD identified in Figure 16c red-shifts and becomes resonant with the cavity mode. A clear anti-crossing is observed, indicating that the QD and cavity are in the strong coupling regime and form two dressed polariton modes. From the minimum splitting of the polaritons, which occurs at a temperature of 39 K, we calculate the cavity-QD coupling strength to be $g/2\pi$=13.4 GHz.

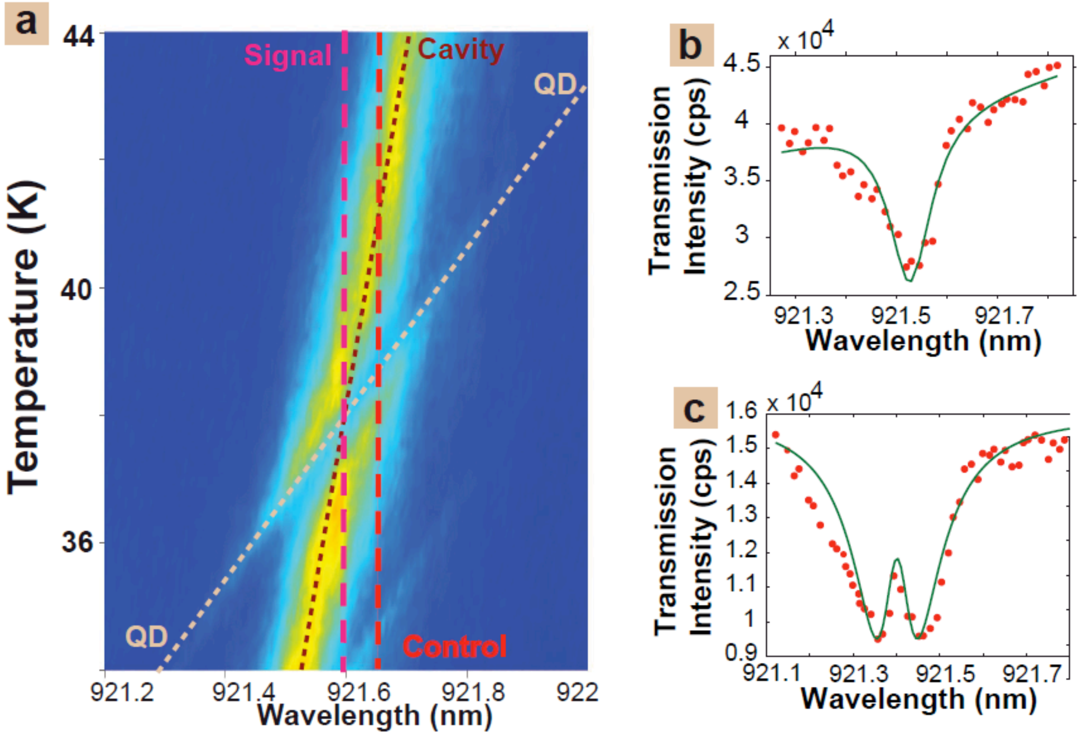

Figure 17 : Near resonant scattering and transmission properties of the device. (a) Cavity scatter under broadband LED excitation as a function of temperature. Dotted lines indicate temperature dependence of QD and cavity, dashed lines denote signal and control wavelengths. (b) Transmission of the bare cavity, which exhibits an anti-resonance due to increased scattering of the cavity mode in the out-of-plane and backward propagating direction. Green line is the theoretical fit to the spectrum. (c)

Transmission of the cavity with QD on resonance. Transmission exhibits a double anti-resonance due to scattering from the two polariton modes. Green line is the theoretical fit to the spectrum.

We next investigate the system under near-resonant excitation conditions using a broadband LED. Figure 17a shows the measured cavity scattering spectrum as a function of device temperature under broadband LED excitation. Similar to the PL spectrum in Figure 16d, an anti-crossing between QD and cavity modes is observed. At the QD resonant frequency the cavity scattering is suppressed due to strong coupling [57,75]. Figure 17b and Figure 17c show the waveguide transmission spectrum at a temperature of 51 K (QD off resonance) and 38 K (QD on resonance) respectively. The waveguide transmission exhibits an anti-resonant behavior when the QD is detuned due to increased cavity scatter. When the QD is resonant with the cavity, the transmission exhibits two shifted anti-resonances corresponding to the two polariton modes. In both conditions we fit to a theoretical weak field model [70,76] and the results of the fit are shown by the solid lines. From the relative contrast of the anti-resonance in Figure 17b we determine the coupling efficiency from the waveguide to the cavity to be 35%.

4.3 Optical switching with pulsed lasers

To demonstrate optical switching, we perform a temporal pump-probe measurement on the fabricated device. The pump and probe are generated by two synchronized Ti:Sapphire lasers. The pump laser has pulse duration of 80 ps. The probe laser initially emits 5 ps pulses that are filtered down to a bandwidth of 0.02 nm (7 GHz), corresponding to a 60 ps pulse duration, using a fiber Bragg grating. The bandwidth of the probe laser is chosen to be less than the spectral width of the dip induced by the QD (approximately *g* in strong coupling). The delay between the pump and probe is controlled electrically by a phase-locked loop in the synchronization circuit. The pump laser is used as the control while the probe laser is used as the signal. We set the signal pulse wavelength to 921.538 nm and the control pulse wavelength to 921.575 nm, so that when the QD is resonant with the cavity, the signal pulse is resonant with the QD and the control pulse is resonant with the lower polariton, as indicated by the dashed lines in Figure 17a. This configuration ensures that the control pulse maximally couples to the cavity mode. The collected signal photons are separated from the control pulse photons using a grating spectrometer.

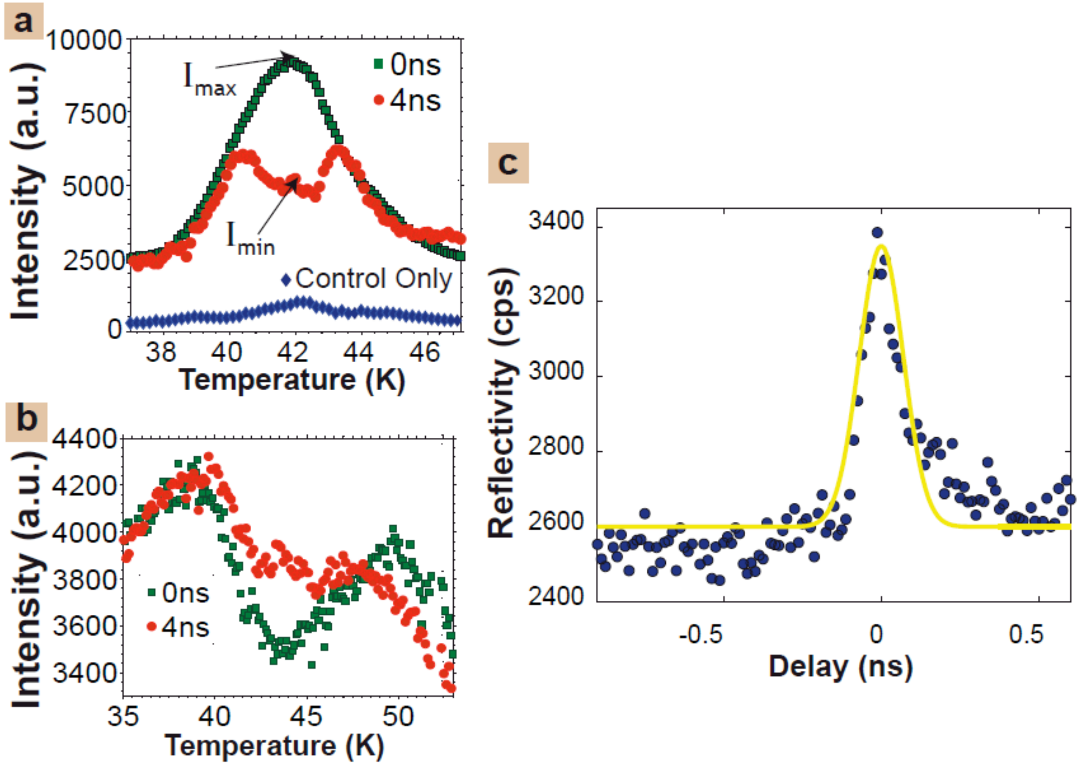

Figure 18 : Time domain characterization of optical switching. The signal scattering intensity as a function of sample temperature for two delays of 0 ns (green squares) and 4 ns (red circles) is shown for (a) at the cavity radiation port and (b) at the

transmission port (output coupler). The contribution of the control signal at the probe frequency due to both spectral overlap and non-resonant energy transfer is indicated as blue diamonds. (c) Cavity scattering intensity at the strong coupling point as a function of delay between the signal and control pulses. Solid line represents Gaussian fit to data.

Figure 18a shows the cavity scattering spectrum of the signal as a function of temperature when the delay between signal and control is set to both 0 ns and a 4 ns. At 4 ns delay, the pulses excite the cavity at different times and therefore do not interact. In this case the cavity scattering spectrum is suppressed when the QD is resonant with the signal energy (41.8 K) due to cavity-QD interactions. When the control and signal arrive simultaneously at the cavity (zero ns delay), the control pulse Stark shifts the QD off resonance [9,12], resulting in the observation of the bare cavity spectrum as the cavity temperature tunes across the signal frequency. Figure 18a also plots the case where there is only a control pulse (blue diamonds). In this case there is still some optical energy at the QD frequency due to spectral overlap between the control and signal as well as non-resonant energy scatter of the control pulse [32,33], but these contributions are small compared to the signal in both the on and off states. The switching contrast, defined as $\eta=(I_{max}-I_{min})/I_{max}$ where I_{max} and I_{min} are the scattering intensities at the QD resonant frequencies at zero and large delays respectively, is calculated to be 0.44. In Figure 18c, we show the behavior of the signal transmitted to the output coupler, which exhibits the conjugate effect where transmission is enhanced when the QD is resonant with the signal frequency.

4.4 Estimation of switching speed and switching energy

To measure the switching speed of the system, we fix the sample at the strong coupling point and plot the cavity scatter as a function of delay between pump and probe, as shown in Figure 18d. The scatter exhibits a sharp peak near 0 ns delay, which is fit to a Gaussian function. From the fit we determine that the switching occurs over a 118 ps time window corresponding to an 8.4 GHz switching rate.

We define the switching energy E_{switch} of the device as the amount of energy in the control pulse propagating in the waveguide needed to induce 90% of the maximum change in reflectivity. In order to calculate this value, we need to determine the efficiency with which light is injected into the waveguide mode. We have seen in chapter 2 that the coupling efficiency of light resonant with the cavity mode is accurately determined by monitoring the magnitude of the cavity-enhanced optical Stark shift experienced by a strongly-coupled QD. We use this technique to exactly measure the coupling efficiency of the input grating. From this measurement, we determine that 0.14% of light incident on the input grating couples to the propagating mode of the waveguide. This value enables us to precisely calculate the pulse energy propagating in the waveguide as a function of the pulse energy incident on the input grating.

Figure 19a plots the relative change in signal scattering intensity, defined as $\rho=(I_{max}-I)/(I_{max}-I_{min})$ where I is the scattering intensity and I_{max} and I_{min} are previously defined, as a function of control pulse energy for three different detunings between the control pulse frequency(ω_c) and QD frequency(ω_{QD}). At low control energies the scattered intensity approaches the nominal low field value I_{min} (ρ=1). As the control pulse intensity is increased, the scatter makes a smooth transition to the high field value I_{max}. For each curve, we fit the data to a theoretical mode given by

$$\rho(E) = \frac{1}{1+\left(E/E_{sat}\right)^2} \tag{4.1}$$

where E is the control pulse energy and E_{sat} is the saturation energy which is treated as a fitting parameter. The above model is consistent with the switching behavior of the device when the nonlinearity is created by optical Stark shift. The horizontal line represents 10 dB (90%) change in ρ, which defines the switching energy. At 12 GHz detuning (red circles), which is close to resonance with the lower polariton, we achieve a switching energy ($E_{switch}^{\min}$) of 14 aJ, corresponding to only 65 photons in the control pulse. The blue squares and green diamonds plot the cases where the pump is blue shifted and red shifted from the lower polariton. In both cases, a higher pumping intensity is required, which manifests itself in a shift of the switching curve to higher energies. Figure 19b plots the switching energy as a function of detuning of the control frequency from the QD frequency. A solid line plots the theoretical curve based on a semiclassical Stark shift model for the nonlinearity, which is in good agreement with experimental data.

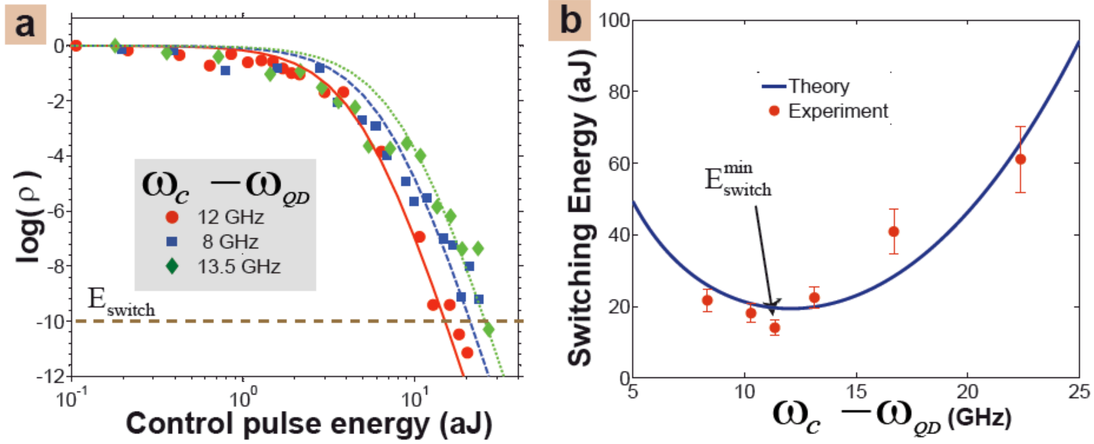

Figure 19 : Characterization of switching energy (a) Switching contrast δ as a function of energy of control pulse for three different detunings between the control pulse and QD frequencies. Lines indicate theoretical fit. Horizontal line indicates 10dB point of switch. (b) Switching energy as a function of spectral detuning between the control pulse and QD resonant frequency. Solid line indicates theoretical prediction using a simple Stark shift model. The minimum switching energy E^{min}_{switch} of 14 aJ corresponding a detuning of 12 GHz is indicated in the figure.

4.5 Characterization of Stark Shift and Saturation

To characterize the nonlinearity in the device, we perform continuous wave (CW) measurements on the fabricated device using a broadband LED emitting between 900-950 nm as the signal, and a tunable external cavity diode laser as the control. The external cavity diode laser is detuned by 0.12 nm from the cavity resonant frequency. Light is collected from the cavity radiation port, and measured using a grating spectrometer. This measurement technique is identical to the one used to obtain the data in Figure 17a, except that we have added the control field from the tunable laser in addition to the signal field.

Figure 20a shows the measured cavity scattering spectrum when only the signal field is injected and the QD is resonant with the cavity mode. The scattering spectrum exhibits a dip at the QD resonant frequency as predicted by semi-classical theory [57,75]. Figure 20b shows the cavity scatter when only the control field is present. A bright peak is observed due to direct scattering of the control, which saturates the spectrometer detector. In addition to this direct scatter, however, we observe direct emission from the two polariton modes due to non-resonant energy transfer processes [32,33]. In order to properly perform measurements using both signal and control fields, we need to separate out the signal scattering from the non-resonant energy transfer, which will inject noise into the measurement.

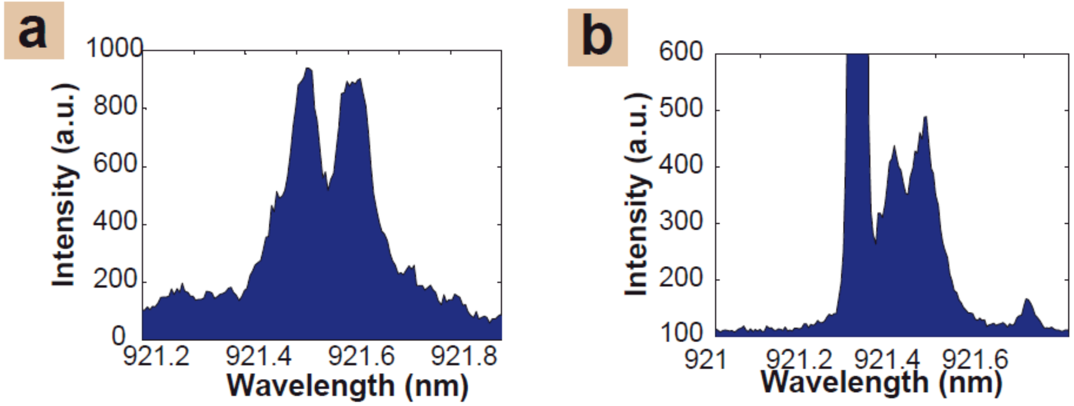

Figure 20 : (a) Scattering spectrum of the cavity-QD system at strong coupling performed with the broadband light source injected into the waveguide input coupler (b) Cavity scatter with only the control. The polariton modes are visible due to non-resonant energy transfer

We set the LED input power so that the signal field is stronger than the incoherent noise of the photons injected from the pump. Figure 21a shows the cavity scatter when both signal and control fields are injected into the input port of the device for three different control powers. At 1 μW of control power the control field is very weak and does not affect the cavity reflectivity, which exhibits a dip at the QD resonant frequency. We note that the contrast of the dip is reduced as compared to Figure 20a, because we are using a relatively large signal power that causes the QD to be partially saturated. We use this larger signal power to minimize the contribution of incoherent photons from the control. As the control field power is increased to 50 μW and 145 μW, we see a nonlinear modification in the cavity spectrum.

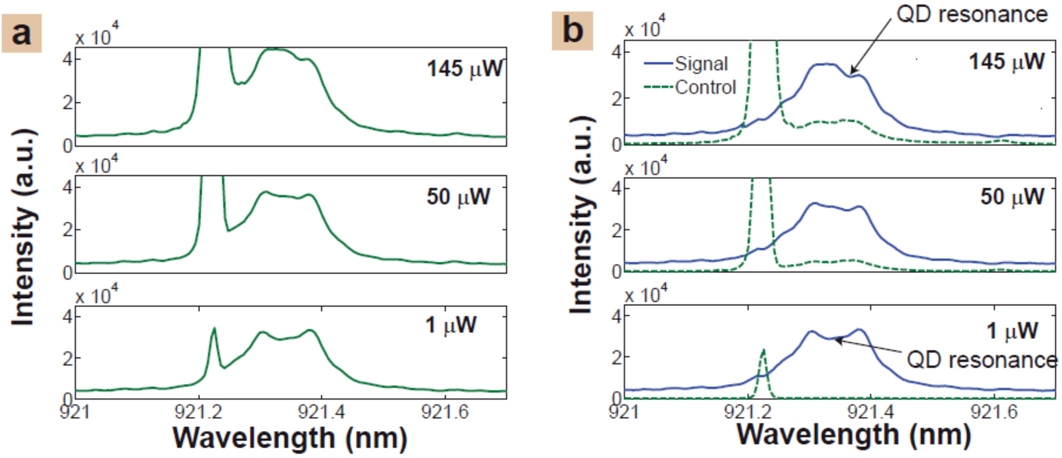

Figure 21 : (a) Cavity scattering spectrum for three different control field powers. (b) Dashed green line shows cavity scattering spectrum with only the control field (no signal). Solid blue line shows the scattering spectrum of only the signal, attained by subtracting the spectrum attained with only the control field from the spectrum shown in Fig. 20a at the equivalent control power level.

To determine the contribution of the signal relative to the non-resonant energy transfer from the control, we perform the scattering experiment at the three control powers using only the control. The dashed green line in Figure 21b shows the results of these measurements. The spectrum of the signal field is then determined by subtracting the total scattering spectrum in Figure 21a from the scattering spectrum using only the control field. This result is shown as a solid blue line in Figure 21b and represents the corrected signal field scattering spectrum. From the corrected signal field spectrum, we see that as the control field intensity is increased, the position of the peak is red shifted due to the optical Stark effect. In addition, a slight reduction in the contrast of the dip is observed which is due to QD saturation. These two nonlinear effects combine to change the cavity reflectivity. At the highest control power of 145 μW, we observe a Stark shift of 0.026 nm, corresponding to 9.2 GHz.

We note that when using CW measurements at high control powers of 145 μW, the incoherent photons from the pump are not negligibly small compared to the signal, even at relatively high signal powers that partially saturate the QD. The ratio of noise to signal photons at the cavity resonant frequency is measured to be 0.35. In contrast, when performing the pulsed experiment we see from Figure 18a, the noise to signal ratio is 0.18, which is lower than the CW case even though the signal is well below saturation. Furthermore, in the pulsed case the noise is mostly dominated by the spectral overlap between the two fields as opposed to non-resonant energy transfer. Thus, although noise injection from the control field can be a problem in CW measurements, it is much smaller for pulsed switching operation. We attribute the difference between these two cases to the fact that at CW operation, the signal and control photons usually hit the cavity at different times. In order to ensure that a control photon is exciting the cavity at the same time as the signal, we need much larger control intensities as compared to signal intensities. This can be seen in Figure 21a where the control saturates the spectrometer detector but the signal is well below saturation. In contrast, for pulsed operation where the pulse durations are close to the cavity decay time, the signal and control photons usually hit the cavity at the same time. We can therefore use control intensities that are closer to the signal levels, resulting in much lower ratios of noise to signal photons.

4.6 Determination of coupling rate between the waveguide and cavity

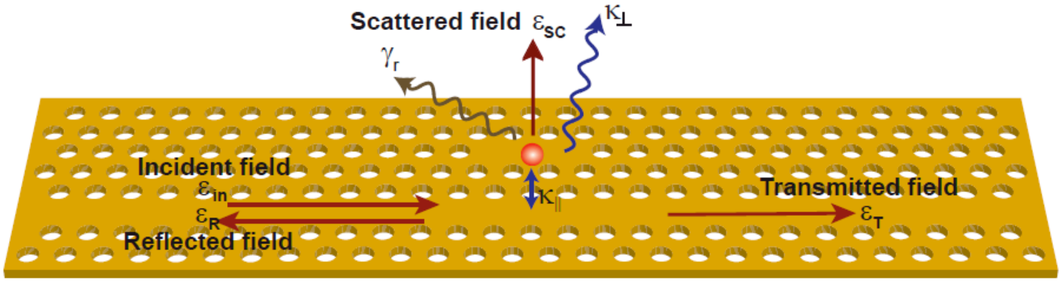

Figure 22 : Schematic of the switch

To determine the coupling rate between the cavity and the waveguide, we define the fields interacting with the cavity and parameters of the cavity-QD system as shown in the schematic in Figure 22. The incident field injected through the input grating is given by ε_{in}. The fields scattered, transmitted and reflected from the cavity are represented by ε_{sc}, ε_T and ε_R respectively. The QD has a radiative decay rate γ_r. The coupling rate between the cavity and the forward propagating mode of the waveguide is $\kappa_{||}$. Similarly, the backward propagating mode of the waveguide also a coupling rate of $\kappa_{||}$ into the waveguide. The cavity also has out-of-plane losses resulting in a perpendicular loss rate given by $\kappa_\perp$. Hence, the total decay rate of the cavity mode is $\kappa = 2\kappa_{||} + \kappa_\perp$.

Figure 23 shows the normalized transmission spectrum of the waveguide, observed by focusing the broadband LED on the input coupler and collecting emission from the output coupler using a small aperture. The spectrum of the transmitted light is measured using a grating spectrometer. We observe anti-resonance at 921.5nm in the transmission spectrum superimposed on the spectral response of the waveguide. This anti-resonance is due to the evanescent coupling of the cavity mode to the waveguide.

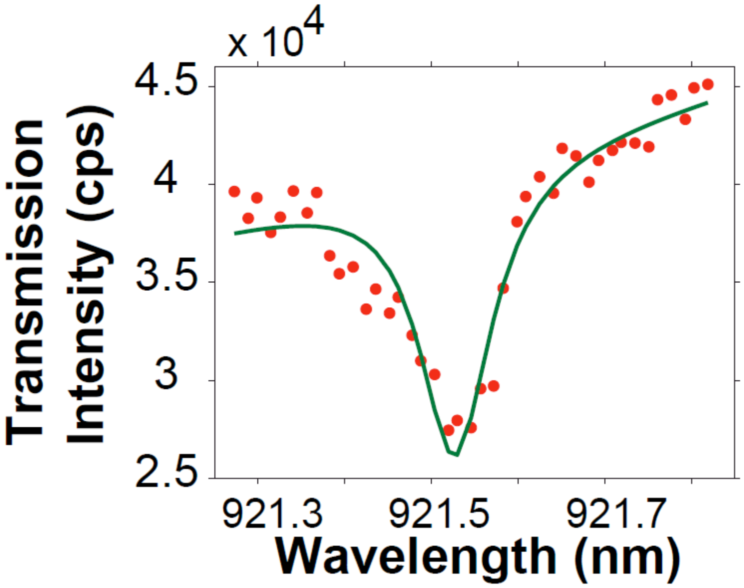

Figure 23 : Waveguide transmission, as measured from the field scattered by the output coupler, which exhibits an anti-resonance due to increased scattering of the cavity mode in the out-of-plane and backward propagating direction. Green line is the theoretical fit to the spectrum.

For large detuning between the cavity and QD, the transmission spectrum may be fitted to that of a bare cavity which is given by the equation [76]:

$$T_c(\omega) = |\varepsilon_{in}(\omega)|^2 \left| \frac{i2\Delta_{cav} + \kappa(1-r_0)}{i2\Delta_{cav} + \kappa} \right|^2 \tag{4.2}$$

where $r_0=2\kappa_{||}/\kappa$ is the reflectivity of the bare cavity (no QD) on resonance, $\Delta_{cav}=\omega-\omega_{cav}$ where ω and ω_{cav} are the driving field frequency and cavity resonant frequency respectively, and $\varepsilon_{in}(\omega)$ is the electric field amplitude of the incident driving field in units of photons per second. The incident driving field $\varepsilon_{in}(\omega)$ can vary with ω due to the spectral response of the grating couplers as well as Fabry-Perot fringing effects caused by multiple reflections between the two couplers and the cavity. In order to account for this spectral dependence, we perform a second order Taylor series expansion of the input power spectrum given by $\left|\varepsilon_{in}(\omega)\right|^2=c_0+c_1(\omega-\omega_{cav})+c_2(\omega-\omega_{cav})^2$. The coefficients c_0, c_1, and c_2 are treated as fitting parameters to attain the best match to the experimental data.

Using r_0 and κ as additional fitting parameters, we fit the experimental transmission spectrum to Eq. 5.2. The best fit, shown as a solid line in Figure 23, is attained for $r_0=0.20$ and $\kappa=29$ GHz. From the value for r_0 and κ, we estimate the in-plane decay rate of the cavity to be $\kappa_{||}=2.9$ GHz corresponding to an in-plane cavity Q of 112400. The percentage of light propagating in the waveguide that couples to the cavity can also be estimated to be $\eta_{cav-wg}=1-(1-r_0)^2=36\%$.

Figure 24 plots the normalized transmission spectrum of waveguide with the QD on resonance with the cavity. In this case, the transmitted spectrum exhibits an anti-resonant doublet feature. This doublet corresponds to mutual scattering from the two polariton modes of the cavity, and is the signature of strong coupling observed through the waveguide transmission. To obtain a theoretical fit to the transmission spectrum with the QD on resonance, we need to take into consideration the dephasing of the QDs due to the short coherence times of InAs QDs and temperature of operation of the switch.

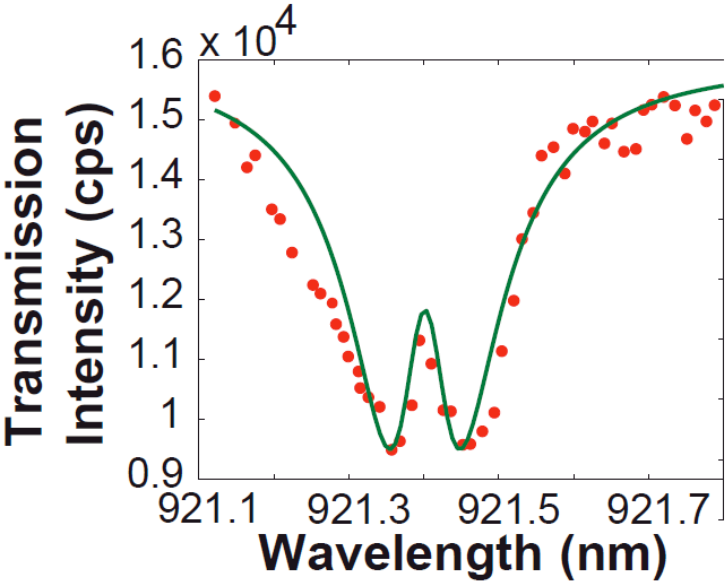

Figure 24 : Waveguide transmission, as measured from the field scattered by the output coupler, with the QD on resonance with the cavity. The spectrum exhibits two anti-resonances corresponding to the two polaritons. Green line is the theoretical fit to the spectrum.

The theoretical values for the transmitted flux can be calculated using cavity input-output formalism. [70] The input-output relation for the cavity is given by $\hat{\mathbf{a}}_{\mathbf{out}} = \varepsilon_{in}(\omega) - \sqrt{r_0\kappa/2}\hat{\mathbf{b}}$ where ε_{in} is the coherent input driving field amplitude, $\hat{\mathbf{a}}_{\mathbf{out}}$ is the bosonic flux operator for the transmitted field and $\hat{\mathbf{b}}$ is the bosonic annihilation operator for the cavity mode. The transmitted flux is then given by

$\left\langle \mathbf{a}_{\mathbf{out}}^{\dagger}\mathbf{a}_{\mathbf{out}}\right\rangle = \left|\varepsilon_{in}(\omega)\right|^{2} - \sqrt{2r_0\kappa}\,\mathrm{Re}\left\{\varepsilon_{in}^{*}(\omega)A\right\} + r_0\kappa n/2$, where $A = \langle \mathbf{a}\rangle$ and n is the cavity photon number given by

$$n = \frac{4}{4\Delta_{cav}^{2}+\kappa^{2}}\left(\frac{g^{2}\left|\rho_{21}\right|^{2}}{\Gamma}\left[\gamma_{QD}+\frac{2g^{2}\kappa}{4\Delta_{cav}^{2}+\kappa}\right]+2g\sqrt{\kappa}\,\mathrm{Im}\left[\varepsilon_{in}^{*}\rho_{21}\right]+\kappa\left|\varepsilon_{in}\right|^{2}\right) \tag{4.3}$$

In the above equation $\gamma_{QD}=(\gamma_r+\gamma_{nr})/2+1/T_2$ where γ_r is the radiative decay rate, γ_{nr} is the non-radiative decay rate, and T_2 is the coherence time and $\Gamma = \gamma_r + \gamma_{nr} + 4g^{2}\kappa/\left(\kappa^{2}+4\delta^{2}\right)$ is the modified QD decay rate where $\delta = \omega_{QD} - \omega_{cav}$ and ω_{QD} is the QD resonant frequency. $\Delta_{cav} = \omega - \omega_{cav}$ where ω and ω_{cav} are the driving field frequency and cavity resonant frequency respectively. The term ρ_{21} is the off diagonal dipole term of the reduced density matrix for the QD which, in the weak field limit, is given by

$$\rho_{21} = \frac{\Omega(i\Delta_{cav}+\kappa/2)}{(i\Delta_{QD}+\gamma_{QD})(i\Delta_{cav}+\kappa/2)+g^{2}} \tag{4.4}$$

where $\Delta_{QD} = \omega - \omega_{QD}$ and $\Omega = -ig\sqrt{\kappa}\varepsilon/\left(i\Delta_{cav}+\kappa/2\right)$. In the weak field limit we have

$$A = \frac{\sqrt{\kappa}\varepsilon_{in}(\omega)(i\Delta_{QD}+\gamma_{QD})}{(i\Delta_{cav}+\kappa/2)(i\Delta_{QD}+\gamma_{QD})+g^{2}} \tag{4.5}$$

We perform a second order Taylor series expansion of the incident field power spectrum given by $\left|\varepsilon_{in}(\omega)\right|^{2} = c_0 + c_1(\omega-\omega_{cav}) + c_2(\omega-\omega_{cav})^{2}$. The coefficients c_0,

c_1, and c_2 are treated as fitting parameters to attain the best match to the experimental data.

The fitting parameters used to compare experiment to theory are the expansion coefficients for the background, along with g, γ_{QD}, ω_{cav}, and r_0. The solid line in Figure 24 shows the best fit curve for the data, which is attained for g=13.0 GHz, γ_a=6 GHz, and r_0=0.20. The values for g is consistent with the value of g=13.4 GHz obtained earlier by estimating g from the relative separation between the polaritons in the cavity scattering spectrum. Similarly, the value for r_0 is also consistent with the previously determined value of r_0=0.20 obtained using the bare cavity transmission.

4.7 Determination of coupling efficiency of input grating

In order to determine the fraction of light coupled from free space to propagating modes of the waveguide, we use optical Stark shift measurements. In chapter 2, we have shown that by measuring the optical Stark shift of a QD resonantly detuned from the cavity we can accurately determine the coupling efficiency of an external field driving the cavity mode. As we show below, this method can be extended in a straightforward way for a waveguide-driven cavity in order to determine the efficiency from before the grating coupler to the waveguide mode. The measurement proceeds by setting the sample temperature to 45 K where the QD is red shifted from the cavity mode by 55 GHz. A tunable external cavity laser diode is focused onto the input grating. In Figure 25a, we plot the scattering spectrum from the cavity as a function of laser detuning from the cavity resonant frequency, where the laser is tuned across the cavity resonance with a laser pump power of 120 μW. The spectrum exhibits a strong direct scattering of the laser, along with a weak emission from the QD caused by non-resonant energy transfer [32,33]. We use this non-resonant signal to monitor both the center wavelength and linewidth of the QD. As the laser becomes resonant with the cavity mode, we observe both a clear shift and broadening of the resonance of the QD. The shift is caused by the optical Stark effect, while broadening is caused by stimulated emission of the QD [77].

To determine the stark shift of the QD as a function of pump power, we fix the excitation laser to be resonant with the cavity mode, and monitor the QD emission via non-resonant transfer of energy from the cavity to the QD. The scattering spectrum is then recorded for increasing values of the pump laser power. For each spectrum corresponding to an input pump power, the emission from the QD is fit to a Lorentzian function to determine the center frequency. The experimental result of stark shift of the QD as a function of pump power is shown in Figure 25b. The amount of Stark shift is directly proportional to the incident photon flux propagating in the waveguide, and can therefore be used to determine the photon flux as a function of measured incident field power before the grating.

In order to determine the relation between the photon flux and the Stark shift, we compare the experimental results to theoretical predictions based on a two-level quantum system coupled to a single mode optical resonator. The theoretical predictions are obtained by solving the full master equation given by $\dot{\rho} = \frac{i}{\hbar}[\rho, \mathbf{H}] + \mathbf{L}\rho$, where **H** is the Hamiltonian of the system and **L** is Liouvillian superoperator representing the losses due to the Markovian processes. The Hamiltonian of a cavity coupled QD in the presence of a driving field, **H** is given by

$$\mathbf{H} = \hbar\omega_{cav}\hat{\mathbf{b}}^{\dagger}\hat{\mathbf{b}} + \hbar\omega_{QD}\hat{\sigma}_{+}\hat{\sigma}_{-} + \sqrt{\kappa_{\parallel}}\varepsilon_{in}\left(\hat{\mathbf{b}}^{\dagger}e^{i\omega_{c}t} - \hat{\mathbf{b}}e^{-i\omega_{c}t}\right) + \hbar g\left(\hat{\mathbf{b}}^{\dagger}\hat{\sigma}_{-} - \hat{\mathbf{b}}\hat{\sigma}_{+}\right) \quad (4.6)$$

where ω_{cav} and ω_{QD} are the cavity and quantum dot frequencies respectively. The cavity field operator and vacuum Rabi frequency are given by $\hat{\mathbf{b}}$ and g respectively while the dipole lowering operator is $\hat{\sigma}_{-}$. $\kappa_{\parallel}$ is the coupling rate between the cavity and the forward propagating mode of the waveguide. The parameter ε_{in} represents the field amplitude of the driving laser propagating in the waveguide. In the Lindblad form, the Liouvillain **L** can be written as

$$\begin{aligned} L(\rho) &= L_{cav}\left(\rho\right) + L_{QD}\left(\rho\right) + L_{dephase}\left(\rho\right) \\ &= \kappa\left(2\hat{\mathbf{b}}^{\dagger}\rho\hat{\mathbf{b}} - \hat{\mathbf{b}}^{\dagger}\hat{\mathbf{b}}\rho - \rho\hat{\mathbf{b}}^{\dagger}\hat{\mathbf{b}}\right) + \gamma_{r}\left(2\hat{\sigma}_{+}\rho\hat{\sigma}_{-} - \hat{\sigma}_{+}\hat{\sigma}_{-}\rho - \rho\hat{\sigma}_{+}\hat{\sigma}_{-}\right) \\ &\quad + \gamma_{dephase}\left(2\hat{\sigma}_{+}\hat{\sigma}_{-}\rho\hat{\sigma}_{-}\hat{\sigma}_{+} - \hat{\sigma}_{+}\hat{\sigma}_{-}\rho - \rho\hat{\sigma}_{+}\hat{\sigma}_{-}\right) \end{aligned} \quad (4.7)$$

where $L_{cav}\left(\rho\right)$represents decay of the cavity mode with total decay rate κ and $L_{QD}\left(\rho\right)$ is the Lindblad operator for spontaneous emission of the QD with decay rate γ_{r}. The non-resonant energy transfer observed experimentally is introduced into the calculations by a pure dephasing process given by $L_{dephase}\left(\rho\right)$, where $\gamma_{dephase}$ is the dephasing rate. We treat the coupling efficiency η as fitting parameter given by $\eta = P_{wg}/P_{inc}$, where P_{inc} is the experimentally measured incident power and

$P_{wg} = \hbar\omega\varepsilon_{in}^{2}$ is the optical power propagating in the waveguide, where we use the phase convention such that ε_{in} is a real number.

We first use the master equation to calculate the power spectrum of the cavity mode, defined as the Fourier transform of the two-time covariance function $\left\langle \hat{\mathbf{b}}^{\dagger}\left(t+\tau\right)\hat{\mathbf{b}}\left(t\right)\right\rangle$, as a function of P_{wg}. From the power spectrum we determine the center wavelength and linewidth of the QD using a Lorentzian fit. The parameter η is then numerically optimized to achieve best agreement between simulation and theory. All calculations are performed using an open source quantum optics toolbox. For the simulations, we set the cavity decay rate to $\kappa/2\pi=28$ GHz, the coupling rate between the waveguide and cavity to be $\kappa_{\|}/2\pi = 2.9$ GHz and the QD radiative lifetime and coherence time are set to $2\pi/\gamma_r = 1$ ns and $T_2 = 500$ ps respectively. The cavity-QD detuning is set to 55 GHz and the cavity-QD coupling strength is set to $g/2\pi=13.4$ GHz, as measured experimentally. The optimal cavity coupling efficiency determined by numerical optimization is estimated to be $\eta = 1.4\text{x}10^{-3}$.

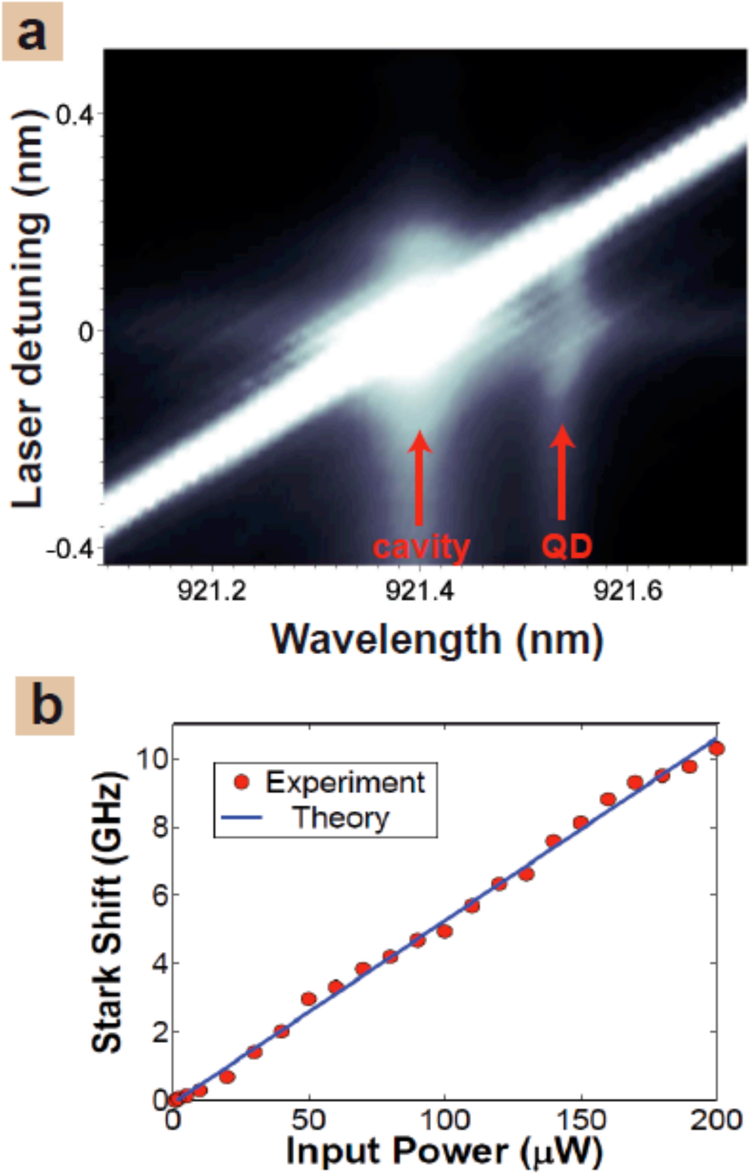

Figure 25 : (a) Cavity spectrum as a function of laser detuning from cavity at 45 K for a 120 μW pump power. (b) Stark shift of QD versus input power at the cavity mode resonance shown as red circles, with fit from simulations shown by solid blue line.

4.8 Analytical model for scattered signal power and switching energy

We compare our experimental results to a simple analytical model based on optical Stark shift of the QD induced by the control pulse. We treat the effect of the control using a semi-classical atom-light interaction model. Treating the interaction in the reference frame rotation with the control field, the Hamiltonian describing the interaction between the control field and the QD is given by $\mathbf{H_c} = \hbar\Omega_c(\sigma_+ + \sigma_-)$, where $\Omega_c = g\sqrt{n_c}$ and n_c is the number of control photons injected into the cavity. Using time-independent first order perturbation theory, the quantum dot resonant frequency is given by

$$\omega_a = \omega_{QD} + \frac{\left|\langle g|\mathbf{H_c}|e\rangle\right|^2}{\mathrm{h}^2\Delta} = \omega_{QD} + \frac{g^2 n_c}{\Delta} \tag{4.8}$$

where ω_{QD} is the quantum dot resonant frequency without any control field, $\Delta=\omega_{QD}-\omega_c$, and ω_c is the control field frequency.

The expression for the scattering spectrum of the signal field can be calculated directly from the Heisenberg equations of motion in the weak field limit [57,75]. These equations are given by

$$\begin{aligned} \frac{d\hat{\mathbf{b}}}{dt} &= -\left(i\left(\omega_{cav} - \omega_s\right) + \frac{\kappa}{2}\right)\hat{\mathbf{b}} - \sqrt{\kappa_{\|}}\,\varepsilon_S - ig\hat{\sigma}_- \\ \frac{d\hat{\sigma}_-}{dt} &= -\left(i\left(\omega_a - \omega_s\right) + \gamma_{QD}\right)\hat{\sigma}_- - ig\hat{\mathbf{b}} \end{aligned} \tag{4.9}$$

where ω_{cav} and ω_s are the frequencies of the cavity and signal respectively. The term γ_{QD} is as defined in Section II $\gamma_{QD} = \frac{\gamma_r + \gamma_{nr}}{2} + \frac{1}{\mathrm{T}_2}$ where γ_r is the radiative decay rate of the QD, γ_{nr} is the non-radiative rate and T_2 is the coherence time of the QD. The above equations are expressed in the frame of reference rotating with the signal field.

We treat the control field as a perturbation into the equations and insert it for the QD resonant frequency. We also assume that the signal field is too weak to induce nonlinearity, so that all nonlinearities are induced only by the control as described by the Stark shift model. The scattered field is given by $\varepsilon_{Sc} = \sqrt{\kappa_{\perp}}\langle\mathbf{b}\rangle$. Inserting the steady state solution to the Heisenberg equations of motion we obtain an expression for the normalized power spectrum of the scattered field given by

$$S(\omega_s) = \left|\frac{\varepsilon_{Sc}}{\varepsilon_s}\right|^2 = \frac{\kappa_{\|}\kappa_{\perp}}{\left|\kappa/2 + \dfrac{g^2}{i(\omega_s - \omega_a) + \gamma_{QD}}\right|^2} \tag{4.10}$$

In order to perform calculations, we need a relationship between the cavity photon number n_c and the incident control filed ε_c. An exact analytical expression for this relation is difficult to attain because the control field would induce nonlinearities that would not only affect the coupling between the signal field and cavity, but would also affect how much control field couples to the cavity. In order to attain a simple analytical model, we assume the control field can strongly modify the coupling between the signal and the cavity, but does not strongly affect the coupling between the control field and cavity. This assumption is realistic because the signal is resonant with the QD, so even a small Stark shift will have a major change on the signal scattering rate. In contrast, the control is highly detuned from the QD, so if we consider only small Stark shifts relative to the cavity linewidth (which is the regime we are primarily interested in), the control field will not strongly affect its own cavity coupling rate. In this limit we can use the weak field relation between the incident control field and the cavity photon number given by [57,70]

$$n_c = \left\langle \hat{\mathbf{b}}^{\dagger}\hat{\mathbf{b}} \right\rangle = \frac{\kappa_{\parallel}\varepsilon_c^2}{\left| i\Delta + \frac{\kappa}{2} + \frac{g^2}{i\left(\Delta+\delta\right)+\gamma_{QD}} \right|^2} \tag{4.11}$$

where $\delta = \omega_{QD} - \omega_{cav}$. Using the above approximation we attain the following expression for the scattered power spectrum as a function of the control field

$$\begin{gathered} S = \frac{4\kappa_{\parallel}\kappa_{\perp}}{\kappa^2} \cdot \left(1 - \frac{C\left(C+1\right)}{\left(C+1\right)^2} \cdot \frac{1}{1+\left(\frac{P_c}{P_0}\right)^2} \right) \\ P_0 = \mathrm{h}\omega_c 2\Delta\left(\frac{1}{C}+1\right) \frac{\left\{ \left(g^2 - \Delta^2 + {}^{\kappa\gamma_{QD}}\!/_{2} \right)^2 + \left({}^{\Delta\kappa}\!/_{2} + \Delta\gamma_{QD} \right)^2 \right\}}{\kappa_{\parallel}\kappa\left(\Delta^2 + \gamma_{QD}^2\right)} \end{gathered} \tag{4.12}$$

where $P_c = \mathrm{h}\omega_c\varepsilon_c^2$ is the incident control power and P_0 is the detuning dependent control power which changes the scattered intensity by 50%. C is the atomic cooperativity of the cavity-QD system and is given by $C = 2g^2 / \gamma_{QD}\kappa$.

In Fig. 19a, we plot the relative change in signal scattering intensity $\rho=(I_{max}-I)/(I_{max}-I_{min})$. Using the expression for S in Eq 4.12, where S_{max} is the scattering power spectrum on resonance with the QD for infinite control power and S_{min} is the scattering power spectrum with no control power, we attain the following expression for ρ as

$$\rho = \frac{S_{max} - S}{S_{max} - S_{min}} = \frac{1}{1+\left(\frac{P_c}{P_0}\right)^2} \tag{4.13}$$

We are specifically interested in the control power which changes ρ by 90% also equivalent to a 10dB change in ρ. By substituting for ρ as 0.1 in Eq 4.13, this happens when $P_c = 3P_0$.

In conclusion, we have demonstrated an all-optical switch using a waveguide coupled to strongly interacting cavity-QD system. Extremely low switching energies of 14 aJ were demonstrated. The results demonstrated here indicate that strong interactions between a QD and photonic crystal cavity can enable extremely low energy and high bandwidth optical signal processing. These results have a broad range of applications in optical communication and optical computation. Furthermore, improvements in the coupling between the cavity and waveguide could enable optical switching at the single photon level, which is of great importance in quantum optics and quantum information.

Chapter 5

An All-Optical Switch using Quantum Dot Saturable Absorbers in a DBR Microcavity

5.1 Introduction

We propose and analyze an all optical switch based on quantum dots embedded in a DBR cavity. The quantum dots behave as saturable absorbers that modify the cavity reflectivity. The device exploits the guided in-plane modes of the DBR to fully separate the control pulse from the input signal. We analyze the performance of the switch under realistic experimental conditions. We calculate the signal loss and switching intensity of the device, specializing to the case of InAs quantum dots embedded in GaAs/AlGaAs DBR structure, and show that the switching power can be as low as 19 μW. Noise injection due to spontaneous emission and switching speeds is also analyzed and showed to be small. Room temperature operation of the switch in the presence of non-radiative mechanisms is shown to increase the switching speeds upto 4350 GHz with low energy consumption per cycle.

The rapid growth of internet data traffic provides difficult challenges for optical communication networks. Currently, such networks rely on transduction of optical to electronic signals in order to route data, which imposes limitations on transmission speed and power consumption. Methods for all-optical signal routing could potentially help to overcome some of these limitations by eliminating the need for electrical transduction in specific applications. For such all-optical routing to become a reality requires optical switching devices that can operate with low power dissipation with practical optical signal levels.

A variety of technologies to realize all-optical switches have been proposed and implemented to date. Some important examples include semiconductor optical amplifiers (SOAs) [78-81], highly nonlinear fibers (HNLFs) [82,83], and periodically poled lithium niobate (PPLN) [84,85]. Optical switching based on quantum well saturable absorbers in vertical microcavities have been used for high-contrast switching [86], switching at high repetition rate [87] and multiwavelength configurations. More recently, nanophotonic structures such as photonic crystals have been proposed to develop more compact devices that can potentially operate at lower power levels [88-91]. Nonlinear properties of carbon nanotubes have also been utilized in optical switching based on saturable absorption [92,93].

The performance of optical switching devices has been a subject of some debate. All-optical switching energies in the attojoule regime have been reported in the literature [7]. However, it has recently been shown that when one accounts for the total power consumption of the device, including the necessary supply power to drive active elements such as optical amplifiers, the power consumption does not scale nearly as favorably as these reported numbers might indicate [8].

One method to reduce the power dissipation of optical switches is to make use of resonant Distributive Bragg Reflector (DBR) structures. Recent experimental [94] and theoretical work [95] has studied the use of semiconductor quantum dots inside DBR microcavities to achieve high speed optical switching. These works considered off-resonant nonlinearities in which the pump laser was tuned to half the bandgap energy and intersubband relaxation of the higher excited states of the QD. Such processes have the advantage of quick optical response, which enabled optical switching on the time scale of 23 ps.

In this chapter, we investigate the use of resonant nonlinearities based on saturable absorption in order to achieve optical switching in a device composed of semiconductor quantum dots inside a DBR microcavity. Saturable absorption is a resonant nonlinearity that can be extremely strong even with low optical powers.

In addition, the DBR cavity supports in plane waveguide modes that can guide the control signal and make it fully separable from the reflected signal, providing a simple two-port device with minimal nanofabrication processing. We analyze the proposed switch using the transfer matrix method where the effect of the quantum dots is incorporated into the model from the analytical solution to the optical Bloch equations. Calculations are performed for the specific case of indium arsenide (InAs) QDs in a GaAs/AlGaAs DBR structure. We show that the switch can operate with switching powers as low as 19 μW, and the total power dissipation of the switch can be as low as 12 μW, well below that of actively driven devices such as SOAs. We also analyze the performance of the switch at room temperature and show that room temperature operation of the switch in the presence of non-radiative mechanisms can result in higher switching speeds(upto 4350 GHz) and low energy consumption per switching cycle (10.02 fJ).

The chapter is organized as follows. In section 5.2 we use transfer matrix calculation to analyze the performance of the switch as implemented by a DBR cavity with embedded QDs. Section 5.3 we investigates noise injection into the signal port due to the spontaneous emission of the QDs. In section 5.4 we investigate switching speed.

5.2 Analysis of optical switching

A schematic of the proposed optical switch is shown in Figure 26. The device is composed of two DBR mirrors made from quarter wavelength thick alternating layers of different dielectric materials. The two mirrors are separated by a cavity spacer region, which forms a DBR microcavity. QDs are embedded inside the cavity spacer, and serve as saturable absorbers that create an intensity dependent cavity reflectivity. In our calculations we will specifically consider the case of a DBR made of gallium arsenide (GaAs) and aluminum arsenide (AlAs) layers with indium arsenide (InAs) QDs embedded in the spacer. This type of DBR structure has been demonstrated in many works both in the form of planar cavities, and micropost cavities [96-98].

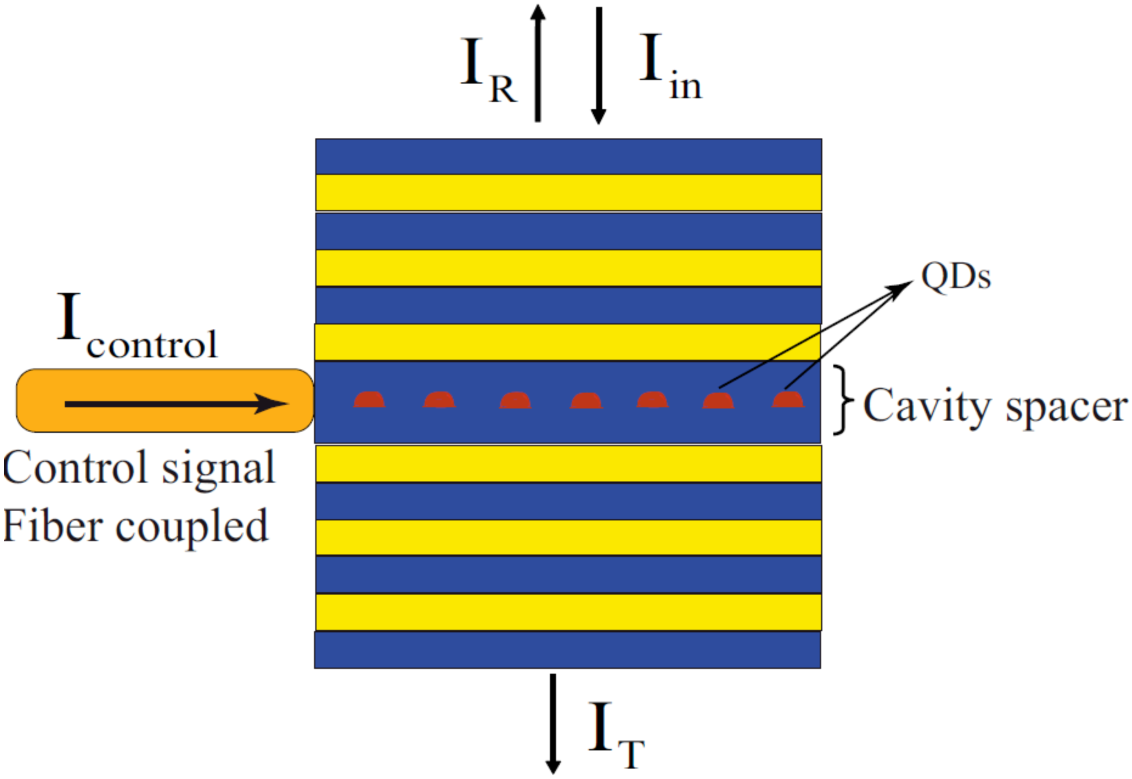

Figure 26 : Schematic of the DBR-QD switch

The switch is excited by two independent optical signals, an input signal and a control signal, as shown in Figure 26. The two signals are selected to have the same carrier frequency. The input is incident from the top of the DBR, and is assumed to be of low intensity so that it does not saturate the QDs. The control is launched directly into the planar waveguide modes of the structure, which can be achieved by directly attaching a fiber to the side of the DBR as demonstrated in recent work [96]. The control signal is sufficiently intense to saturate the QDs and therefore modify the amount of absorption in the cavity. Because the signal and control pulse travel in orthogonal directions, they are fully separable and do not exhibit cross-talk, with the exception of spontaneous emission noise which will be analyzed later.

To analyze the proposed device we use the transfer matrix method to calculate the reflection and transmission coefficients of the DBR [99]. The properties of the QDs embedded in the cavity spacer are incorporated into the transfer matrix model through the susceptibility of the cavity spacer which is given by $\chi_{spacer} = \chi_{GaAs} + \chi_{QD}$, where χ_{GaAs} is the susceptibility of bare GaAs and χ_{QD} is the contribution due to the quantum dots. We consider the interactions of the QD ensemble with the field $E = E_{input} + E_{control} = \hat{e}E\cos\omega t$ where E_{input} is the input field, $E_{control}$ is the control field, and $\hat{e}$ is a unit vector in the direction of the polarization. Each QD is a two-level quantum system whose interactions with the electric field is determined by the optical Bloch equations

$$\frac{d\rho_{11}^{i}}{dt} = -\frac{i\Omega}{2}(\rho_{12}^{i} - \rho_{21}^{i}) + A\rho_{22}^{i} \tag{5.1}$$

$$\frac{d\rho_{22}^{i}}{dt} = \frac{i\Omega}{2}(\rho_{12}^{i} - \rho_{21}^{i}) - A\rho_{22}^{i} \tag{5.2}$$

$$\frac{d\rho_{21}^{i}}{dt} = -(\beta + i\Delta_{i})\rho_{21}^{i} - i\frac{\Omega}{2}(\rho_{22}^{i} - \rho_{11}^{i}) \tag{5.3}$$

In the above equations, ρ_{11}^{i} and ρ_{22}^{i} are the diagonal population terms of the ground state (state 1) and the excited state (state 2), while ρ_{21}^{i} is the off diagonal term that gives the dipole moment. We define $\Omega = \mu E / \hbar$ as the Rabi frequency where μ is the QD dipole moment. In addition, $\Delta_i = \omega_i - \omega$ where ω_i is the resonant frequency of the i'th QD, $A = \mu^2 \omega^3 / 3\pi\hbar\varepsilon c^3$ is the Einstein A coefficient, and $\beta = A/2 + 1/T_2$ where T_2 is the dipole dephasing time.

The Bloch equations can be solved in the steady state to get the QD polarizability α_{QD}^{i} given by

$$\alpha_{QD}^{i} = \frac{i3\pi\varepsilon c^3 A}{2\omega^3(\beta + i\Delta_i)} \frac{1}{1 + I / I_{sat}^{i}} \tag{5.4}$$

where $I = I_{input} + I_{control}$ is the total electric field intensity at the QD (we assume there is no phase relation between the input and control pulse so their intensities simply add) and the saturation intensity I_{sat}^{i} is given by

$$I_{sat}^{i} = \frac{\hbar\omega^3(\beta^2 + \Delta_i^2)}{6n\pi c^2 \beta} \tag{5.5}$$

Due to the large inhomogeneous broadening of the QD ensemble, each QD is detuned differently from the optical fields and thus has a different polarizability and saturation intensity. For this reason we cannot simply multiply the polarizability by the QD density to get the susceptibility. Instead, we must use the more general definition

$$\chi_{QD} = \lim_{\delta v \to 0} \frac{\sum_i \alpha_{QD}^i}{\varepsilon_0 \delta v} \tag{5.6}$$

where δv is the volume of a small volume element inside the cavity spacer. We define $N = N_{tot} / V\Gamma$ as the number of QDs per unit volume per unit frequency, where N_{tot} is the total number of QDs in the cavity, V is the volume of the cavity spacer region, and Γ is the inhomogeneous linewidth of the QD ensemble. Using this definition we can convert the sum to an integral to obtain

$$\chi_{QD} = i\frac{3\pi^2 n^2 ANc^3}{2\omega^3}\frac{1}{\sqrt{1+I/I_{sat}}} \tag{5.7}$$

where the saturation intensity I_{sat} is given by $I_{sat} = \frac{\hbar\omega^3\beta}{6n\pi c^2}$. The expression for I_{sat} given in Eq (5.7) represents the saturation intensity of a collection of inhomogeneously broadened QDs and is thus independent of detunings of the QDs. The expression for χ_{QD} is obtained in the limit that the inhomogeneous broadening of the QDs is large compared to the spontaneous emission rate of the QD. This is especially valid for InAs QDs in which the inhomogeneous broadening may be as large as 20nm (7.4 THz) even though emission rate is only 1 GHz. The susceptibility is purely imaginary, indicating that the QDs behave only as absorbers. The real part of the susceptibility cancels out provided that that spectral distribution of QDs is symmetric about the frequency of the optical signal. If the distribution is asymmetric there will be a small real component to the susceptibility that will result in a small shift of the cavity resonance. Having defined the QD susceptibility, we can define the relative permittivity in the cavity spacer region as $\text{Ú}_{cav} = 1 + \chi_{GaAs} + \chi_{QD}$. We insert this number into the transfer matrix calculation to account for QD absorption.

We first analyze the case of a bare DBR structure that does not contain any QDs ($\chi_{QD} = 0$). We select the DBR to be composed of alternating layers of 62.5nm thick GaAs (n=3.6) and 78nm thick AlAs (n=2.9). The cavity spacer is made up of GaAs and has a thickness of 125nm. The reflectivity of the structure depends on the number of DBR layers n_l. Figure 27a plots the reflectivity of the DBR cavity for $n_l = 4$ and $n_l = 10$. The alternating quarter wavelength layers create a broadband stop band (810-1100 nm for n_l=10), and the cavity resonance appears as a dip in reflectivity within the stop band. The resonance frequency is determined by the index of refraction and thickness of the cavity. For the parameters we selected, the resonance frequency appears at 900 nm. By increasing the number of DBR layers we increase the mirror reflectivity resulting in a sharper resonance. This can be seen qualitatively in Figure 27a. The cavity linewidth is most easily quantified by the quality factor $Q = \Delta\omega / 2\omega_c$, where ω_c is the cavity resonant frequency and $\Delta\omega$ is the full-width half-maximum linewidth of the cavity resonance. The quality factor is plotted as a function of DBR layers in Figure 27b.

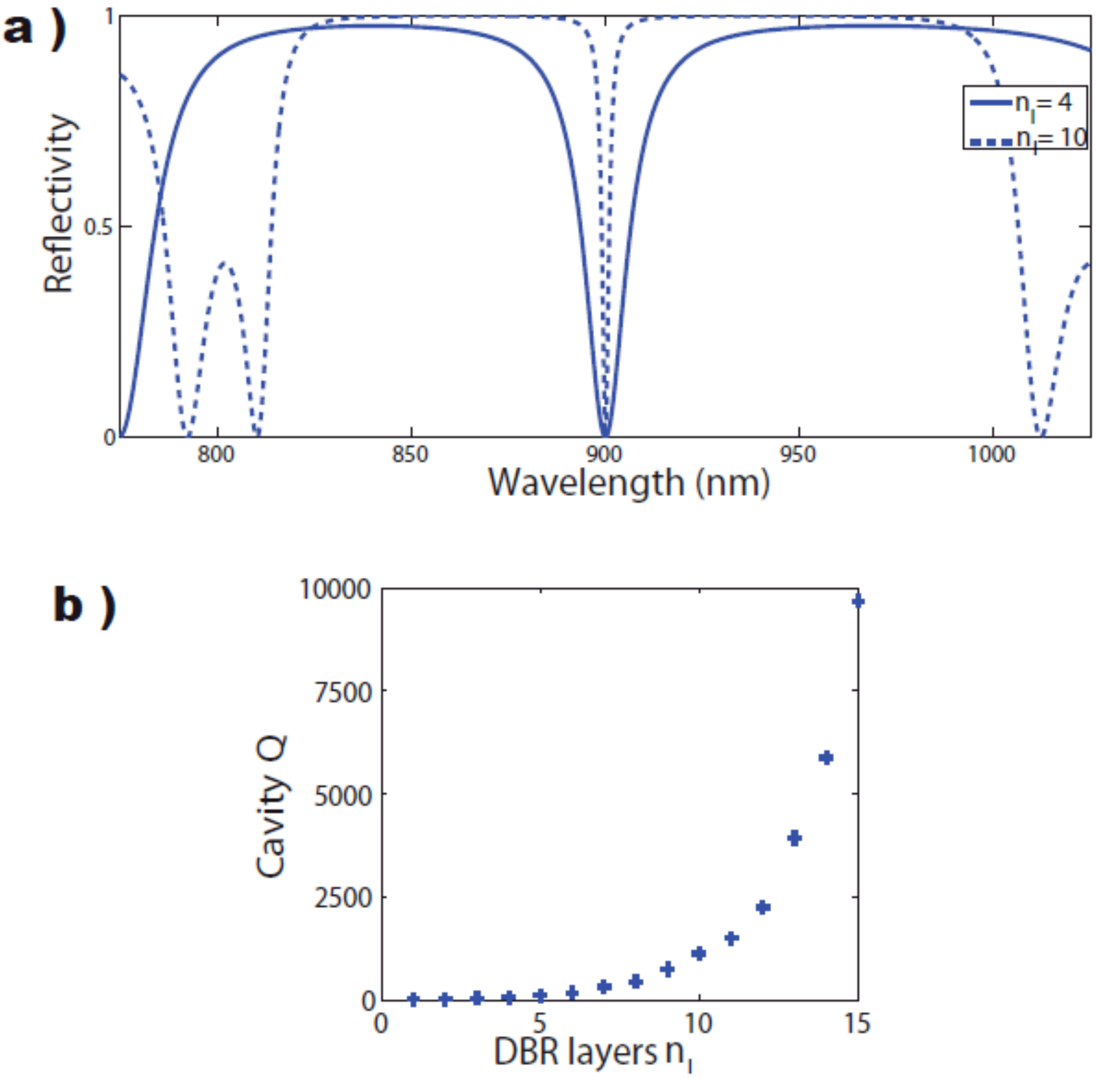

Figure 27 : a) Reflectivity of the bare DBR cavity for n_l = 4 and n_l = 10 b) Cavity Q of the DBR as a function of number of DBR layers

Next, we introduce QDs into the cavity and calculate the effect on the reflectivity. We specifically consider the case of InAs QDs where $A = 1\,\text{GHz}$ [22,100]. The properties of InAs QDs emitting at other wavelengths, specifically at 1.3 and 1.55µm have also been studied for passive modelocking of lasers using saturable absorption [101,102]. The dephasing time is highly temperature dependent, for our calculations we consider the low temperature behavior (~10-30 K) where phonon broadening is not significant and $T_2 = 500$ ps [103]. Based on these values, the saturation intensity is $I_{sat} = 3.94 \times 10^{-2}$ W/cm^2. We first analyze the switch when the control pulse is in its off state ($I_{control} = 0$). Figure 28 plots the reflectivity of DBR cavity as a function of the number of DBR layers n_l. The intensity of the signal pulse is assumed to be sufficiently weak so the $I_{signal} / I_{sat} \approx 0$. In the limit of low QD density, the DBR structure has low reflectivity because all of the light is transmitted. As the QD density is increased, the DBR makes a continuous transition from highly transmitting to highly reflecting. This transition is caused by the increased absorption inside the cavity.

Increasing the number of DBR layers affects the reflectivity in two ways. First, as the number of DBR layers increases the density of QDs required to modify the cavity reflectivity decreases. Second, the maximum reflectivity achieved in the high density regime, defined as R_∞, also increases with the number of QDs. An estimate of the density of QDs required per unit frequency can be obtained by requiring the reflectivity of the OFF state(R_{OFF}) to be 90% of its asymptotic high density limit. For $n_l = 12$, we require $N = 0.064$QDs/μm^3/GHz to achieve this reflectivity.

We next consider the cavity properties when a control pulse is present (i.e. the switch is in its ON state). The control pulse will serve to saturate the QD population creating an intensity dependent absorption. Figure 29 shows the cavity reflectivity as a function of control intensity for several different DBR layers. In each case the QD density is selected so that the unsaturated cavity reflectivity is set to $0.9R_\infty$. For

$n_l = 8$ and $n_l = 12$, the maximum reflectivities are set to $0.9R_\infty = 0.872$ and 0.896 respectively. For low control intensities, the QDs are unsaturated and reflectivity for each of the DBR layers is $0.9R_\infty$. As the control pulse intensity is increased there is a sharp transition from high reflectivity to low reflectivity (i.e. high transmission). Despite the fact that the 8 layer and 12 layer cavities have different cavity Q, the switching curves look nearly identical. In fact, if we plotted the switching curves for higher number of DBR layers they would look indistinguishable from the 12 layer cavity. In the high finesse limit the switching intensity becomes completely independent of the cavity Q. We define this Q independent switching intensity as I_{switch}. In the high finesse limit, the ratio between I_{switch} and I_{sat} remains a constant defined as J. From the saturation curves in Figure 29, J can be obtained to be 1603. Thus, $I_{switch} = JI_{sat} = 63.16$ W/cm^2 for the GaAs DBR system.

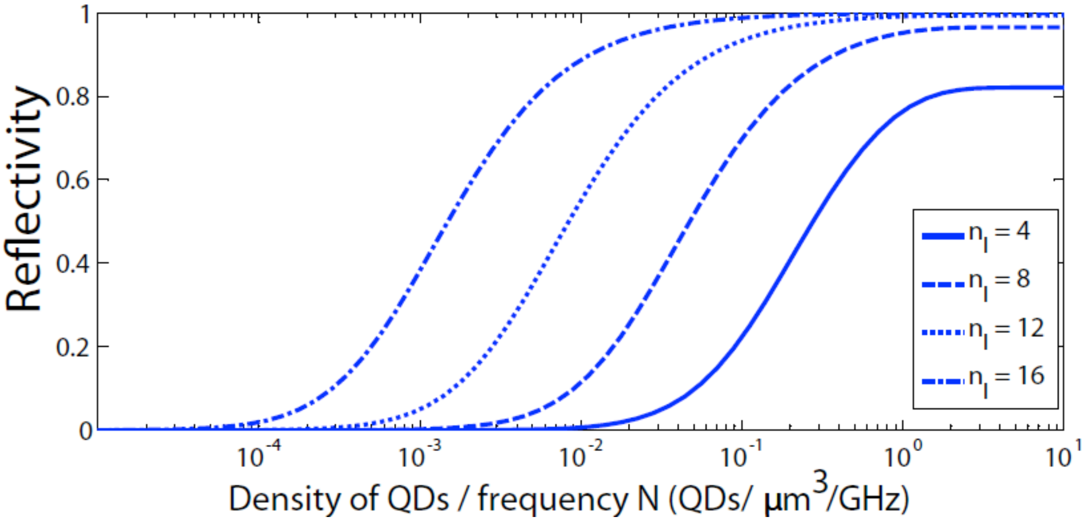

Figure 28 : Reflectivity vs density of QDs/unit frequency for different DBR layers (control pulse = OFF)

For the switch to be fully in its ON state we must have $I_{control} > I_{switch}$ throughout the length of the device. Because the QDs are absorbing, the control pulse intensity will decay as it propagates along the planar waveguide mode of the DBR. The position dependent control pulse intensity obeys the propagation equation

$$\frac{dI_{control}}{dz} = \frac{\alpha_0 I_{control}}{\sqrt{1 + \frac{I_{control}}{I_{sat}}}} \tag{5.8}$$

An analytical solution for the above equation can be attained in the highly saturated regime where I / I_{sat} ? 1. In this limit

$$I_{control}(z) = \left[\sqrt{I_{control}(0)} - \frac{\alpha_0 z}{2} \sqrt{I_{sat}} \right]^2 \tag{5.9}$$

where $I_{control}(0)$ is the intensity at the input facet to the device and $I_{control}(z)$ is the intensity a distance z away from the input facet. For a device of length L, the condition $I_{control}(L) = I_{switch}$ ensures that the switching condition is satisfied throughout the device. From the above equation we attain

$$I_{control}(0) = \left(\sqrt{I_{switch}} + \frac{\alpha_0 L}{2} \sqrt{I_{sat}} \right)^2 \tag{5.10}$$

In order to minimize the switching intensity we want to make L small in order to approach the minimum input intensity of $I_{control} = I_{switch}$. However, reducing L results in a smaller device which requires a tighter focus spot size for the input field. If the input field is focused too tightly it will not be able to efficiently couple to the DBR modes of the cavity. The choice of the dimensions of the device must be based on the minimum spot size to which the input signal can be focused without losing coupling to the DBR structure.

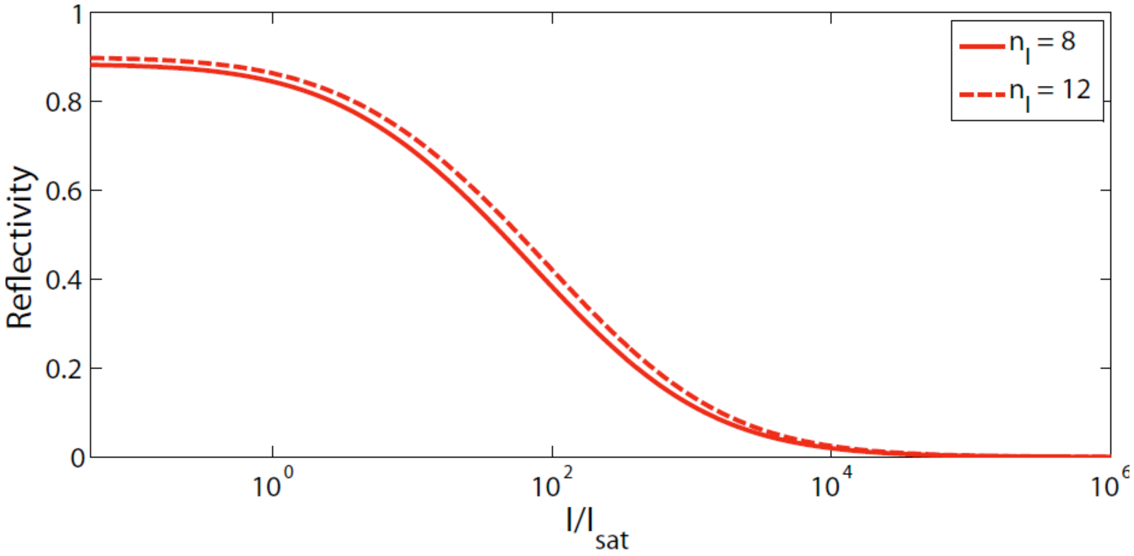

Figure 29 : Reflectivity as a function of the control pulse (control pulse = ON) for n_l = 8,12

The loss in coupling efficiency of the input signal to the DBR with reduction in spot size can be understood as follows. The modes of the DBR are plane wave modes, while a focused spot is composed of a superposition of plane waves propagating at different angles. If the input field is not propagating at normal incidence the cavity resonant frequency is shifted. Figure 30 plots the shift of the cavity resonant frequency as a function of angle of incidence of the plane wave. Each component of the focused beam will see a different resonance frequency. The component of the focused beam traveling at normal incidence will couple to the cavity mode. But at as some critical angle of incidence, defined as θ_c, the cavity resonance will have shifted by more than a linewidth, and plane waves with a greater incidence angle than this critical value will not couple well to the cavity. This critical angle is marked in Figure 30 for n_l of 8, 12 and 16 as 0.036, 0.07 and 0.15 radians respectively.

In order for a focused beam to couple well to the DBR cavity, the majority of its angular components must be within the critical angle. For a Gaussian beam the angular spread is given by $\Delta\theta = \lambda / \pi w_0$, where w_0 is the focused beam waist. Efficient coupling to the cavity will occur when $\Delta\theta < \theta_c$, which puts a minimum limit on ω_0 given by $w_0 = \lambda / \pi\theta_c$For $n_l = 16$, the minimum spot size is 10μm, and this number decreases as the number of DBRs is reduced. Therefore, we set $L = 100\mu$m for all subsequent calculations which ensures that the spot size is much larger than the minimum spot size. This spot size will result in 1% of the light being reflected for $n_l = 16$.

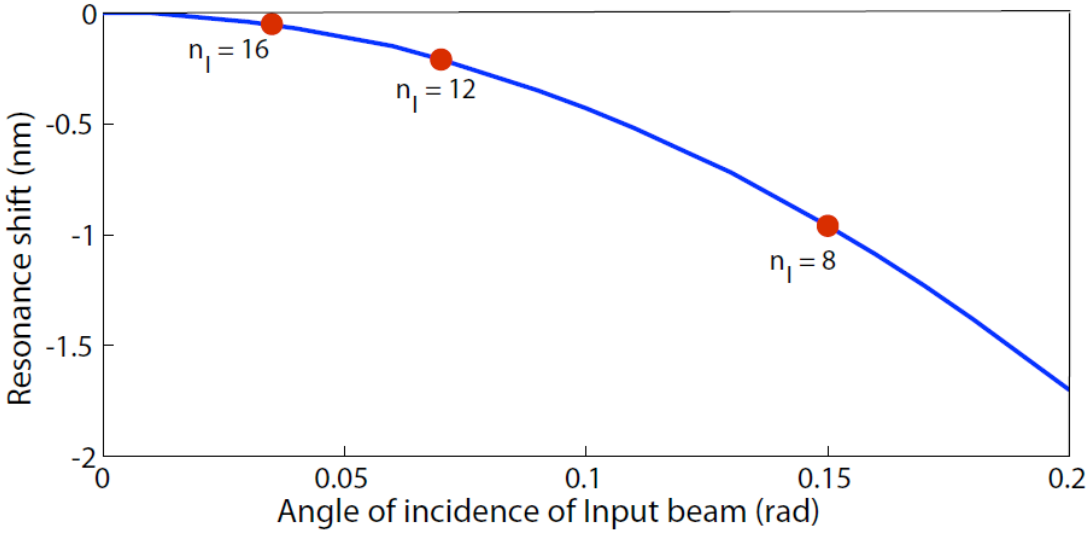

Figure 30 : Shift in the resonance frequency of the DBR cavity with change in the incidence angle between the input signal and DBR cavity. The maximum divergence angle for the input beam incident on a cavity with n_l=8,12 and 16 are indicated by red circle in the plot

Figure 31 plots $I_{control}(0)/I_{sat}$ as a function of the number of DBR layers n_l using a device size of $L = 100\mu$m. For each n_l, the QD density is selected so that the reflectivity is given by $R = 0.9R_\infty$. As the number of DBR layers is increased the input control intensity decreases because we can achieve the same level of reflectivity with a lower QD density, resulting in lower optical losses along the waveguide modes. In the high finesse limit the input control signal reaches the asymptotic limit $I_{control}(0) \approx I_{switch}$.

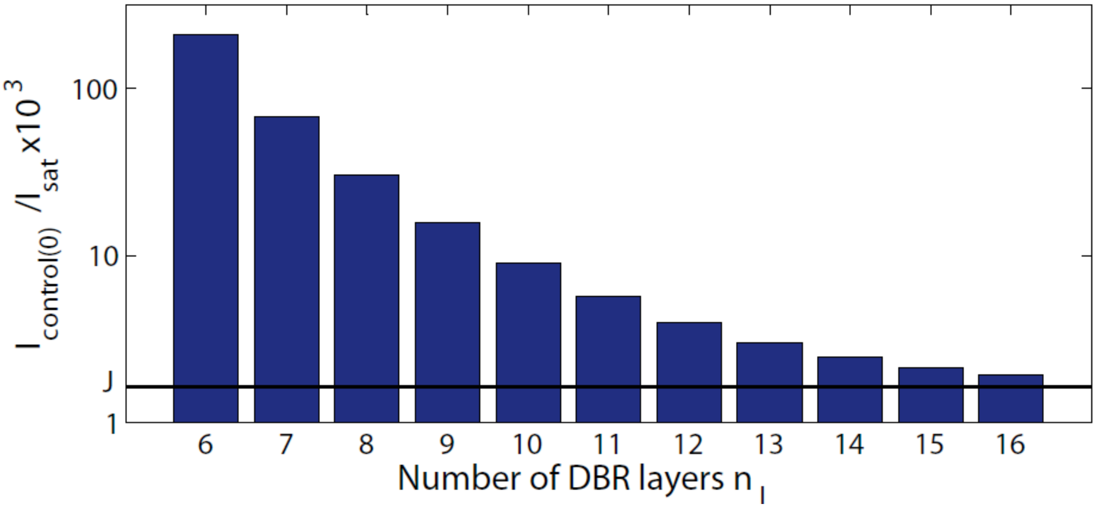

Figure 31 : Input control power as function of number of DBR layers

In most optoelectronic applications the important parameter is the total control power, not the control intensity. The control power depends on the transverse mode confinement of the DBR waveguide. We determine these modes using numerical finite difference time domain (FDTD) simulation. Our simulations were performed using MEEP, an open source FDTD solver [104]. The calculated waveguide modes are shown in Figure 32a.

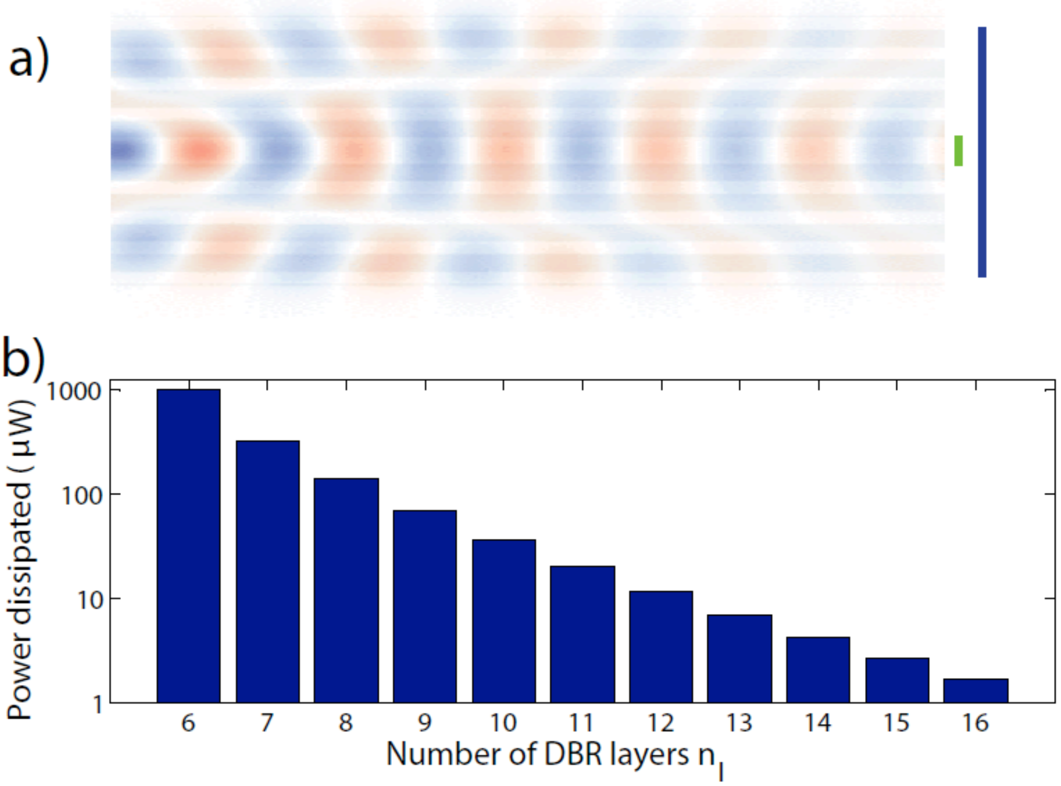

Figure 32 : (a) Guided mode of the control pulse with the DBR layers (b) Power dissipation of the DBR switch as a function of number of DBR layers.

The mode calculations indicate that the control pulse is not localized to the cavity spacer region. Instead, a significant fraction of the control intensity propagates in the DBR mirrors. The fraction of control power propagating in the cavity region is determined by normalizing the power flowing in the cavity spacer (denoted by the green line) to the total power traveling in the DBR (denoted by the blue line), which is given by $\eta = 0.41$. The total control power required to create field intensity $I_{control}$ is then $P_{control} = CI_{control}$. The parameter C is equivalent to the cross-sectional area over which the control signal is confined within the DBR cavity. Thus, $C = Lh/\eta = 3\times10^{-5}\ \text{mm}^2$ where h is the height of the cavity spacer region. From the values for C and $I_{control}$, $P_{control} = CI_{control} = 46.8\mu$W when $n_l = 12$. In the limit of large n_l, the control power drops to $CI_{switch} = 18.9\mu$W.

The total amount of power dissipated in the device is given by

$$P_{diss} = P_{signal} + P_{control} - P_{out} \tag{5.11}$$

where P_{signal} and $P_{control}$ are the total incident signal and control powers and P_{out} is the total power exiting the device (i.e. the amount of signal and control power exiting the switch). Under normal switch operation most of the signal will either be transmitted or reflected, so the majority of the power dissipation occurs in the control pulse. Then, the power dissipation is given by

$$P_{diss} = C\left(\sqrt{I_{sat}I_{switch}} + (\alpha_0 L/2)^2 I_{sat}\right) \tag{5.12}$$

Figure 32b plots the power dissipation as a function of n_l. A steady reduction in power dissipation can be attained by increasing the number of DBR layers. For $n_l = 12$, the power dissipation is 11.6μW. This power dissipation is very low when compared to the power dissipation of SOAs, which dissipate at least 10mW. The significantly lower power dissipation is achieved because, unlike SOA's, saturable absorption does not require an external power supply to maintain population inversion. This is one of the main advantages of using direct resonant nonlinearity.

5.3 Noise injection from spontaneous emission

One of the advantages of using the planar waveguide modes of the DBR to inject the control pulse is that it is fully separable from the input signal. However, spontaneous emission from the saturated QDs can serve to inject some of the control signal into the reflected and transmitted ports. For good switching operation, this injected noise should be small compared to the input signal power.

To calculate the noise power injected by spontaneous emission we consider the worst case in which each QD that is in the excited state scatters one photon per radiative lifetime. The total power scattered by the QDs into the input and output modes is then the sum of the spontaneous emission of all the QDs. The power scattered by the i'th QD within a frequency range of $\Delta\omega$ is given by

$$P^i_{noise} = \hbar\omega ANV\rho^i_{22}\Delta\omega \tag{5.13}$$

where ρ^i_{22} is the average population of the upper state for the i'th QD. From the steady state solutions to the equations of motion for the density matrix given in Eqs.5.1-5.3, the upper state population can be solved to be

$$\rho^i_{22} = \frac{\dfrac{I}{2I^i_{sat}}}{1+\dfrac{I}{I^i_{sat}}} \tag{5.14}$$

where I^i_{sat} is saturation intensity of the i'th QD given by Eq 5.8. The total spontaneous emission noise is then obtained by summing over all the QDs within the cavity over the inhomogeneous linewidth Γ of the QDs. The intensity I depends on the position of the QD along the device. However, we can attain an upper bound for the spontaneous by setting $I = I_{control}(0)$. The total scattered power can is then given by

$$P_{noise} = \hbar\omega ANV\beta \frac{I_{control}(0)/I_{sat}}{\sqrt{1+I_{control}(0)/I_{sat}}} \tan^{-1}\left(\frac{\Gamma/\beta}{\sqrt{1+I_{control}(0)/I_{sat}}}\right) \qquad (5.15)$$

In the limit that the inhomogeneous linewidth Γ is much larger than the spontaneous emission rate of the QDs, the expression for spontaneous emission noise simplifies to

$$P_{noise} \approx \pi\hbar\omega ANV\beta\sqrt{I_{control}(0)/I_{sat}} \qquad (5.16)$$

For a cavity with dimensions of $100\mu\text{m}\times 100\mu\text{m}$ with a cavity spacer thickness of 125nm, containing a QD density of 0.064 QDs/μm^3/GHz (for $n_l = 12$) at an emission wavelength of 900 nm the total scattered power P_{noise} is $4.14\mu\text{W}$. However, not all of this power is injected into the reflected or transmitted ports of the device. A large fraction of the power will be injected into the waveguided modes and will not contribute to cross talk.

In order to determine the fraction of scattered power that exits to the top and bottom of the DBR we perform FDTD simulations of a single dipole inside cavity. From the simulation we determine the ratio of power emitted out-of-plane to power emitted in-plane to be $\eta = 0.01$. Thus, the DBR structure serves to reduce the degree of crosstalk by a factor of 100, reducing the scattered power to 41.4 nW.

The degree of crosstalk can be further improved by spatial filtering of the scattered power. The out-of-plane radiated power escapes from the top of the DBR with an isotropic radiation pattern that diverges in 180° angle. Since the input beam has a wavelength of 900nm and is incident on a 100 µm x 100 µm area device, the angular divergence of the Gaussian beam is $\theta = \frac{\lambda}{\pi w_0} = 0.0029$ rad, much smaller than the π

divergence area of the scattered out-of-plane spontaneous emission. By spatial filtering we can therefore reduce the amount of crosstalk be an additional faction Ú$= 0.0029/\pi = 9.23\times10^{-4}$. The total amount of scattered power drops from 4.14 nW to 38.2 pW. When comparing this number to the maximum signal intensity 50.2 μW, we see that the scattered noise power is negligible compared to the signal. In fact, the scattered noise power is only a factor of approximately 10 above the shot noise power of the maximum input signal which is 3.3 pW. Thus, the scattered emission is not only small, it would even be difficult to detect.

5.4 Switching Speeds

The majority of our discussion has focused on reduction of switching power and power dissipation, which is the primary motivation for using resonant nonlinearities. However, resonant nonlinearities can result in slow switching speeds because the recovery of the switch is limited by the excited state decay rate of the QD. To this point we have only accounted for decay of the excited state through spontaneous emission, as can be seen in Eq. 5.1 and Eq. 5.2. In this case the switching speed is limited to the spontaneous emission lifetime which is 1 ns for InAs QDs. However, it is possible to speed up the excited state decay rate by introducing non-radiative decay mechanisms. Non-radiative decay can be intentionally introduced during the growth process through low temperature (LT) growth of GaAs [105], low temperature growth of InAs QDs on LT GaAs and ion-implantation of As atoms onto GaAs surface [106-108]. Due to higher concentration of As within the crystal, they give rise to fast defect levels. Both these techniques have been shown to reduce the carrier lifetimes to 230fs. However, they also have the disadvantage that they lead to degradation of *Q* of the DBR cavity and addition of nonsaturable absorption. Techniques for reduction of nonradiative lifetime of InAs QDs have also been demonstrated [95,109-111]. Another method would be to operate at higher temperature, which has the advantage of simplicity but the disadvantage of introducing large dephasing as well. In the presence of non-radiative decay, the switching rate is giving by

$$\frac{1}{\tau_{switch}} = A_{rad} + A_{nr} \tag{5.17}$$

where A_{rad} (A_{nr}) is the radiative (non-radiative) decay rate. We then have $\beta = 1/\tau_{switch} + 1/T_2$. Increasing the non-radiative decay rate will serve to increase the switching speed, but at the same time result in greater power dissipation due to increased β.

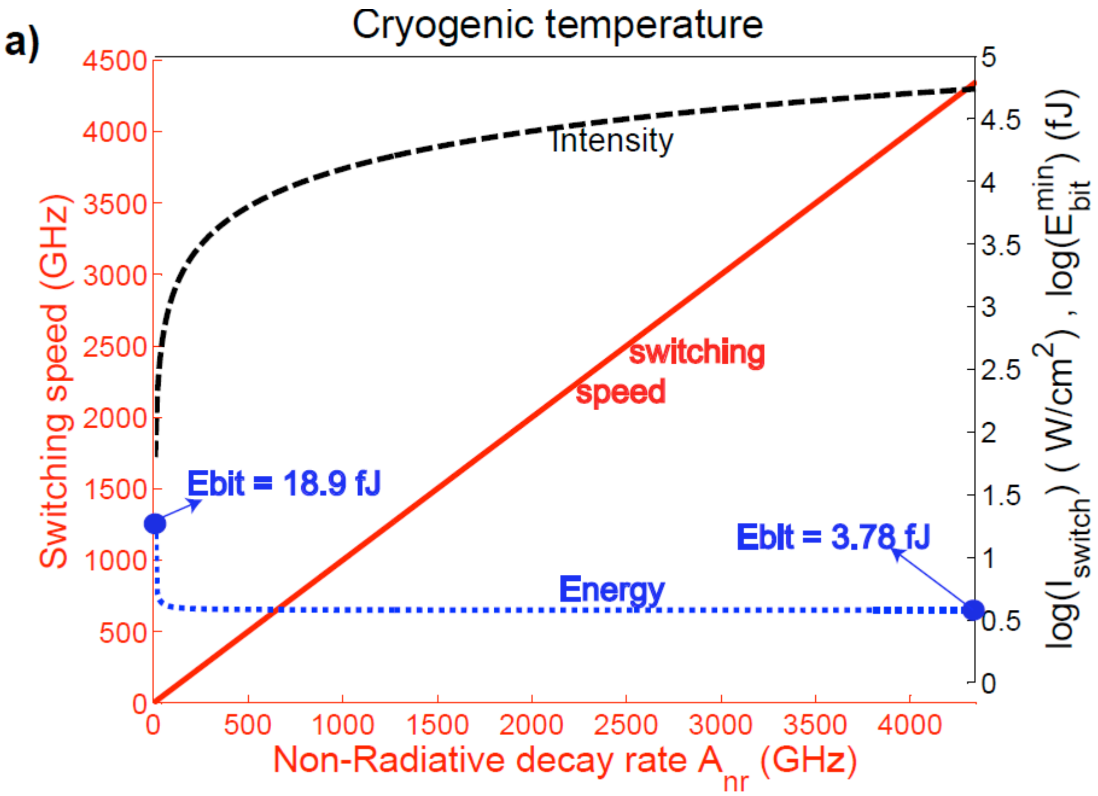
a)
Cryogenic temperature
Switching speed (GHz)
4500
4000
3500
3000
2500
2000
1500
1000
500
0
Intensity
switching
speed
Ebit = 18.9 fJ
Ebit = 3.78 fJ
Energy
0
500
1000
1500
2000
2500
3000
3500
4000
Non-Radiative decay rate A_{nr} (GHz)
5
4.5
4
3.5
3
2.5
2
1.5
1
0.5
0
$\log(I_{switch})$ (W/cm^2) , $\log(E_{bit}^{min})$ (fJ)

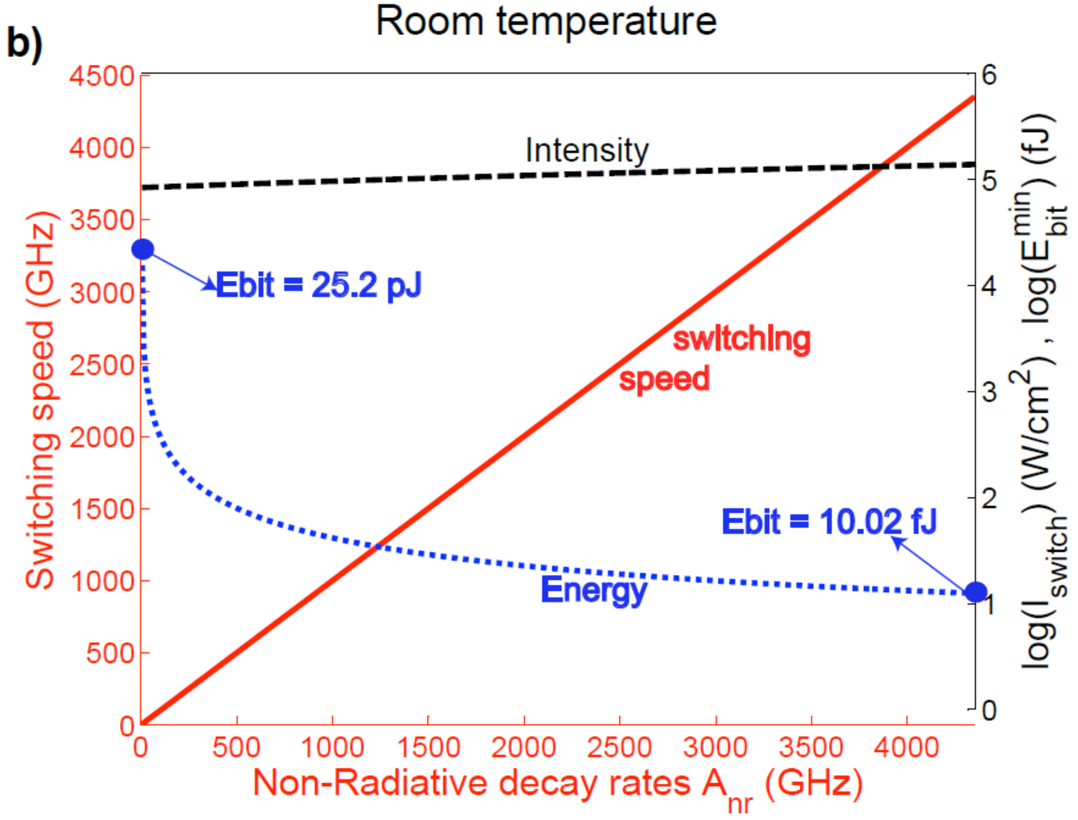
b)
Room temperature
Switching speed (GHz)
4500
4000
3500
3000
2500
2000
1500
1000
500
0
Intensity
Ebit = 25.2 pJ
switching
speed
Ebit = 10.02 fJ
Energy
0
500
1000
1500
2000
2500
3000
3500
4000
Non-Radiative decay rates A_{nr} (GHz)
6
5
4
3
2
1
0
$\log(I_{switch})$ (W/cm^2) , $\log(E_{bit}^{min})$ (fJ)

Figure 33 : Dependence of switching intensity, switching time and E_{bit} on the nonradiative lifetimes at (a) 4K and (b) room temperature. Switching speed is displayed on the left axis. Switching intensity and E_{bit} are displayed on the right on log axis

Figure 33a plots the dependence of switching speed and switching intensity on the non-radiative decay rates(A_{nr}) of the QDs. The limit of A_{nr} is chosen to be equal to 4350 GHz (1/230 fs) which is shortest carrier lifetime observed in GaAs systems. With the introduction of non-radiative decay mechanisms into the system, the switching speed increases proportionally. However, this also brings about an increase in switching intensity. The switching intensity increases from 63 W/cm ^{2} when $A_{nr} = 0$ to 50kW/cm ^{2} when $A_{nr} = 4350$ GHz. However, the more fundamental parameter is the switching energy per bit (E_{bit}) which is defined as energy required to perform one switching operation. The minimum energy per bit can be obtained to be

$$E_{bit}^{min} = P_{control}^{min}\tau_{switch} = \frac{CJ\hbar\omega^3}{6\pi nc^2}\left(1+\frac{1}{T_2}\left(\frac{1}{A_r + A_{nr}}\right)\right) \tag{5.18}$$

The dependence of E_{bit}^{min} on A_{nr} is also plotted in Figure 33a. The minimum switching energy per bit with $A_{nr} = 0$ is 18.9 fJ. The minimum switching energy per bit with $A_{nr} = 4350$ GHz is 3.78 fJ. Thus, even though the switching intensities have increased considerably with increasing A_{nr}, E_{bit} decreases due to the larger bandwidth (shorter switching times). So, non-radiative mechanisms lead to better performance of the switch in terms of smaller switching energy per bit and higher switching speed.

Most practical applications would require room temperature switching operation. At room temperature, the pure dephasing time T_2 of InAs QDs on GaAs has been measured to be 260 fs. This value is significantly smaller (2000 times) than $T_2 = 500$ ps at cryogenic temperature. It is evident from Eq 5.18 that by decreasing the dephasing times, the switching energy per bit increases. Without non-radiative decay, the switching speed, switching intensity and E_{bit}^{min} at room temperature are 1 GHz, 84 kW/cm^2 and 25.2 pJ respectively. However, these numbers can be improved by introducing non-radiative decay, as shown in Figure 33b. As nonradiative decay is increased the switching speed increases linearly but switching intensity, which is dominated by dephasing, remains almost constant. The increase in switching speed of the device without any change in switching intensity due to non-radiative mechanisms results in a significant drop in E_{bit}. At room temperature, E_{bit}^{min} with $A_{nr} = 4350$ GHz is 10.02 fJ. Comparing this with E_{bit}^{min} of 3.78 fJ with $A_{nr} = 4350$ GHz at cryogenic temperatures, it is only a factor of 2.7 higher. Thus, introducing non radiative decay can compensate the increase in switching intensity brought about by shorter dephasing times with respect to switching energy.

5.5 Summary

In summary, we have proposed and analyzed an implementation of an all-optical switch using QD saturable absorbers in a DBR cavity. The device was found to exhibit low switching power and power dissipation under realistic operating conditions. It is also easy to fabricate using standard planar epitaxial growth techniques and requires minimal nanofabrication capabilities to make. The proposed switch satisfies all the requirements needed for all optical logic, making a good candidate as a basic building block for optical transistors. It may therefore find applications in reducing power requirements for optical networking and optical computation.

Chapter 6

Reversible tuning of Photonic crystal cavities using photochromic thin films

6.1 Overview of photonic crystal cavity tuning techniques

We demonstrate reversible tuning of a photonic crystal cavity resonance using a thin photochromic film composed of spiropyran and PMMA that serves as a photosensitive cladding layer. Exposure of spiropyran to ultraviolet light results in smooth redshift of the cavity resonance that can be reversed by exposure to visible wavelength light. We achieve a reversible resonance shift of up to 2.7 nm, which can be performed locally on individual cavities. The resonance shift over multiple successive UV and visible light exposures is studied to determine the repeatability of the photochromic film.

Integrated nanophotonic structures play an important role in development of high-speed and low-power optical devices. One of the most promising methods integrating optical components uses photonic crystal structures [112]. Photonic crystals enable the development of high-Q cavities [22,47,113] and low-loss waveguides that can be combined to form complex integrated structures on a semiconductor chip [114,115]. These integrated structures are finding applications as efficient filters [116], optical logic components [26,27], and quantum optical devices.

One of the main limitations of photonic crystals is the difficulty of post-fabrication tuning. Photonic crystals can be tuned by changing the temperature of the sample, which modifies the index of refraction by shifting the bangdap, [117] or by depositing an atomic layer of a gas such as xenon or nitrogen [118]. Such tuning methods are not localized and affect the resonances of the entire sample, making it difficult to tune individual components. Methods for localized temperature tuning using heating pads enable better local control of cavity resonances [119], but still affect a large enough area of the device to make it difficult to tune closely-packed photonic structures. In addition, for experiments in which photonic crystals are coupled to quantum dots (QDs), temperature tuning also shifts the QD resonances [31], making the system less controllable.

Another method for tuning photonic crystals is to coat them with a photosensitive cladding layer, such as chalcogenide glass, whose index of refraction can be optically modified [120,121]. Chalcogenide glass films have been used to tune both photonic crystal cavities and quantum cascade lasers by local optical excitation that induces a shift in the index of refraction of the cladding. However, for chalcogenide glass cladding this shift is irreversible, so once the cavity is shifted there is no way to undo the change.

6.2 Photochromic sample preparation

Here we introduce a technique for tuning of photonic crystal structures which is both local and reversible. This capability could be used for development of reconfigurable photonic devices that can be reversibly modified post fabrication. Reversible local tuning is achieved by spin coating a thin layer of photochromic material composed of a mixture of a spiropyran (SP) and polymethylmethacrylate (PMMA) on top of the device. Spiropyrans are a class of photochromic compounds whose absorption in the visible wavelengths can be modified reversibly through irradiation with UV and visible light [122]. This change in absorption occurs because SPs can exist in two stable forms, spirocyanine (SC) and merocyanine (MC). By irradiation with UV or visible light, SPs can be transformed reversibly between the colorless SC and colored MC forms. Accompanying the change in the visible absorption of the SP layer on top of the cavity is a change in refractive index at NIR wavelengths, causing a shift in the cavity resonance. At the same time, SPs are highly transparent in the NIR wavelengths and illumination with NIR light has little effect on its absorption. These properties make SP an ideal photochromic material for gallium arsenide (GaAs) based photonic crystal devices.

The photochromic material used in our experiments consisted of 5% 1,3,3-Trimethylindolinonaphthospirooxazine (TCI America) and 0.5% 950 PMMA A4 dissolved in anisol. This particular SP was chosen because it was found to operate well at cryogenic temperatures, in contrast to other types of SP [123]. The specific concentration of 5% SP was the maximum amount that could be dissolved in anisol, and was therefore selected in order to deliver the highest concentration of photochromic material to the sample. Adding a small amount of PMMA was found to provide a more uniform coat of the SP when spun on the sample surface.

We first characterized the absorption properties of a photochromic film spun on a glass slide at 500 rpm using a spectrophotometer. Figure 34 shows the results of the spectrophotometer absorption measurement from 400 to 1000 nm. The photochromic film right after spin coating, shown as a thick solid line, features little absorption indicating that the SP is initially in its SC form. The film is then exposed to UV light from a mercury xenon lamp with an intensity of 3 W/m^2 for 10 minutes. After UV exposure the absorption increases significantly in the wavelength range of 550 to 650 nm, as shown in the solid black curve, indicating that a significant fraction of SP has been converted to its MC form.

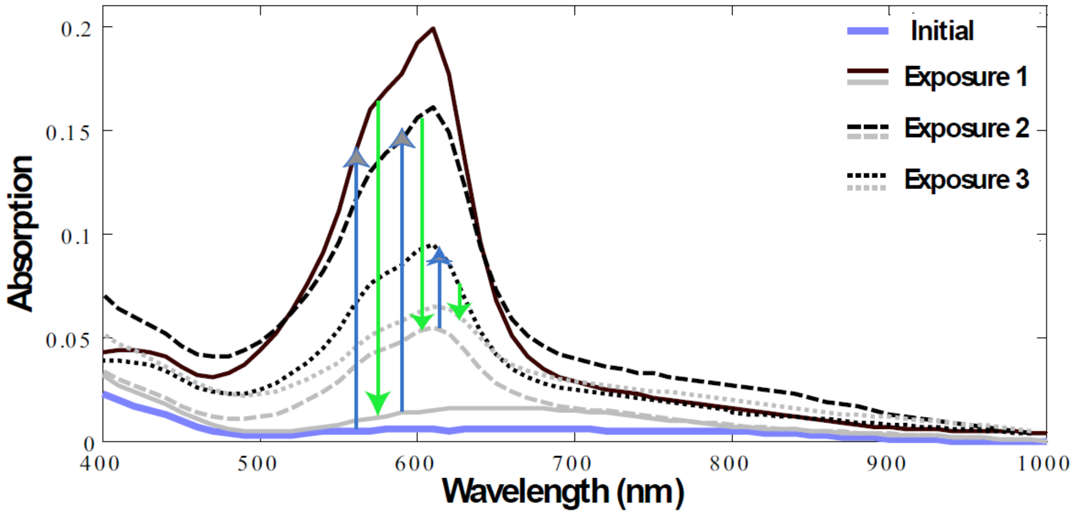

Figure 34 : Absorption of the SP film after exposure to UV and green light for 10 min. The absorbance of the film after UV exposure is indicated in dark shades and after green exposure is indicated in light shades.

Next, the sample was illuminated with 532 nm light picked off from a frequency doubled Nd:YAG pump laser, for 10 minutes at an intensity of 12 W/m^2. The absorption was once again measured (solid light gray line) and found to return to near its original starting point, showing the reversibility of the process. When the film is not irradiated by UV or visible light, it is stable and does not degrade. The absorption in the 900 to 1000 nm region is small in both forms of SP. Thus, for cavities that are resonant at NIR wavelengths we can use the SP film to shift the cavity resonance without degrading the cavity *Q*. After initial illumination with UV and green light, the procedure was repeated two more times on the same sample, as indicated by the dotted and dashed lines. It can be seen that the reversibility of the material degrades as it is cycled repeatedly between SC and MC forms. Although this degradation puts a limit on the number of times a film can be reversed, the film can be easily washed away with acetone and a new film deposited. We further characterized the refractive index of the photochromic film in its initial state to be 1.5 using an n-k analyzer, which estimates the refractive index of a thin film.

In order to demonstrate reversible tuning of photonic crystal structures, we spin-coated a thin film on a GaAs sample containing photonic crystal cavities. Figure 35a shows an SEM image of the photonic crystal cavity fabricated for the cavity shift experiments. The initial sample is composed of a 160 nm thick GaAs grown on a 500 nm thick sacrificial layer of $Al_{0.8}Ga_{0.2}As$. A single layer of InAs QDs of density 100-150 QDs/μm^2 was grown at the center of the GaAs slab. The 2-D photonic crystal with triangular lattice structure was patterned onto the sample using electron beam lithography and inductively coupled plasma etching. The sacrificial layer was then undercut by wet etching to create the photonic crystal membrane. We used an L3 cavity design formed by removing 3 holes from the photonic crystal lattice composed of 72 nm holes with a 230 nm lattice constant. The device was cooled to 4 K and photoluminescence (PL) measurements were performed using a confocal microscope.

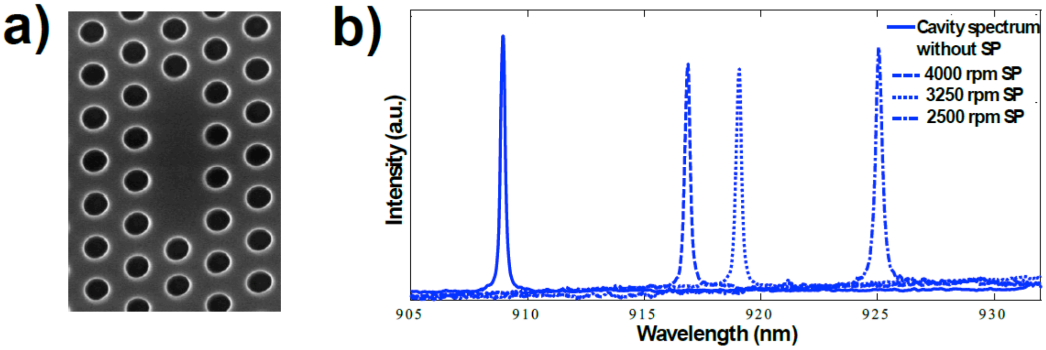

Figure 35 : a) SEM image of the photonic crystal cavity. b) Shift in resonances of the cavity after spinning on the photochromic material at different spin speeds

To determine the appropriate SP thickness, the film was spun on the same sample at three different spin rates of 4000 rpm, 3300 rpm, and 2500 rpm. The film thicknesses corresponding to these spinning rates, determined by independent SEM cross-sectional measurements, are 35 nm, 55 nm, and 100 nm respectively. To obtain spectra of the cavity, the sample is mounted in a cryostat cooled to 4K and illuminated at 780 nm from a Ti:Sapphire laser using a 0.75NA objective. The photoluminescence from the cavity is then captured using the same objective and focused onto the CCD of the spectrometer for spectroscopy measurements. Figure 35b shows the measured PL cavity spectrum for these three different film thicknesses along with the spectrum of the uncoated cavity. The uncoated cavity has a center wavelength of 909.1 nm and a measured *Q* of 5060. The InAs QDs act as a bright internal source, enabling us to measure the cavity resonance over the broadband luminescence of the QDs. After depositing the photochromic films of different thicknesses the cavity resonance was red-shifted by 8.0 nm, 11.1 nm, and 16.5 nm respectively. The cavity *Q*s measured at these three thicknesses were 4640, 4260 and 2640. For very thin films (30 nm), the effective index above the GaAs slab is still close to air so there is little effect on the cavity *Q*. As we make the film thicker the structure becomes more asymmetric and light is allowed to escape from the top more quickly, degrading the cavity *Q*. For the 100 nm film the degradation of the *Q* was considered to be too severe, so all measurements were performed using either 35 nm or 55 nm films.

6.3 Photochromic tuning method

To locally shift a single photonic crystal on the sample, we placed the sample in the cryostat cooled to 4K and illuminated it with either 375 nm light from a doubled Ti:Sapphire laser or 532 nm light from a doubled Nd:YAG. The UV spot size was approximately 5 µm^2 in diameter, corresponding to a UV intensity of 1.2 W/cm^2. The green light was also focused to a spot size of 5 µm^2, corresponding to an intensity of 24 W/cm^2. Exposure of the sample surface created a visible change in the SP film that was localized to the illuminated spot. The intensity of visible light was chosen to be much higher than that needed for UV, because the reversibility of SP degrades at cryogenic temperatures. We initially illuminated with UV to convert the SP to from its colorless SC form to its MC form. Figure 36a shows a series of PL spectra of the cavity after twelve 10 s exposures using UV light for 55 nm thick film. Each exposure created a red shift of approximately 0.25 nm. After twelve exposures a maximum shift of 2.7 nm was achieved. We note that no detectable change of cavity *Q* was observed throughout the entire tuning range. Following UV exposure a set of exposures with the green laser was then used to convert the SP back to its SC form to reverse the tuning. The cavity was shifted back to near its original resonance, but a residual shift of 0.5 nm remained. This residual shift is due to the fact that after green illumination the SP does not fully return to its original absorption spectrum. A similar experiment was carried out for the 35 nm film thickness which was found to have nearly identical behavior but achieved only a 2 nm maximum cavity shift.

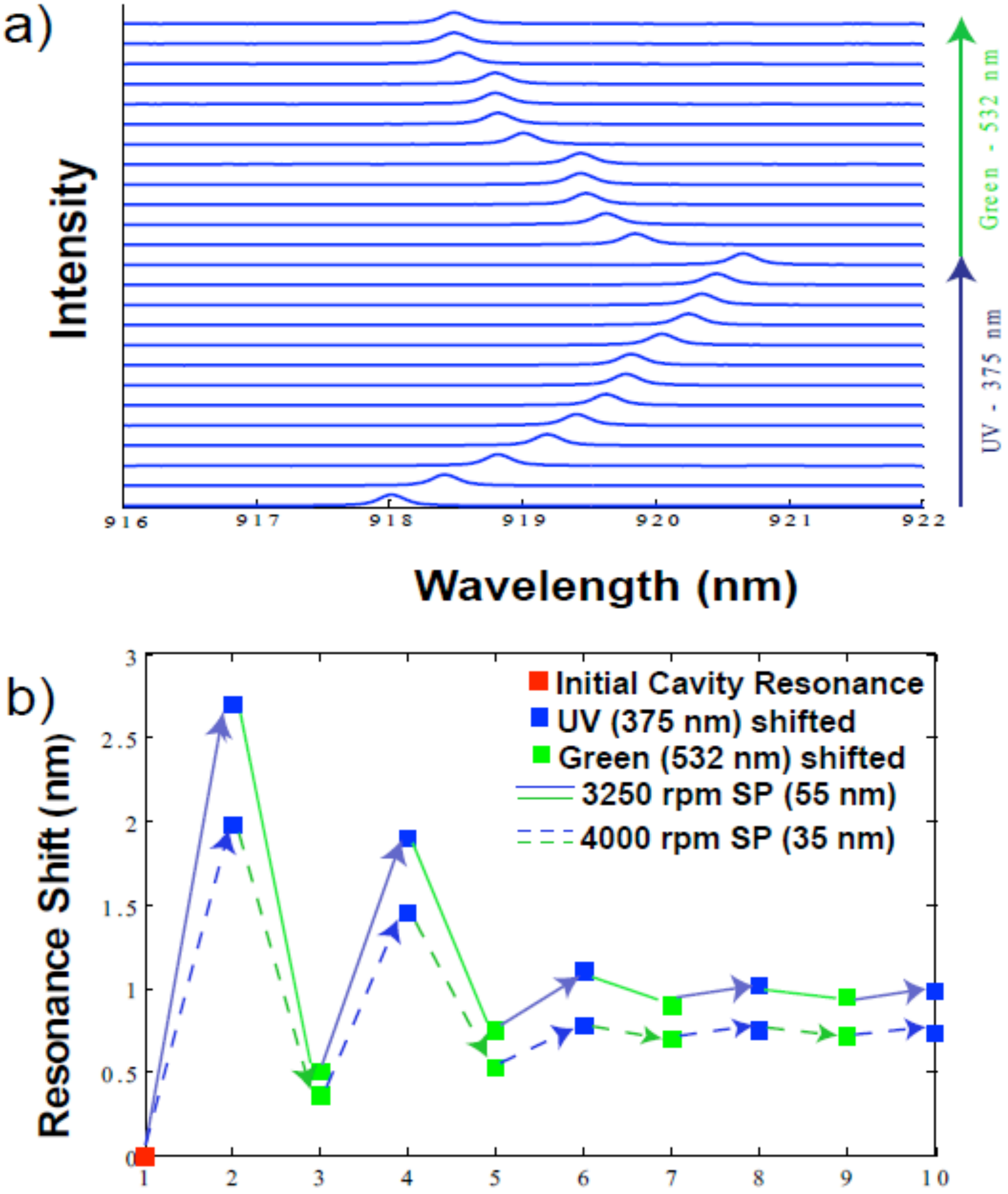

Figure 36 : Fine shifts in cavity resonance with exposure to UV and green. The SP film used corresponds to a thickness of 55nm spun at 3250 rpm b) The maximum shifts in cavity resonance after exposure to UV and green light as a function of the number of exposures

6.4 Reversibility of the photochromic film

To explore the reversibility of the shift, we increased the UV intensity to 3.84 W/cm^2 and the green intensity to 76.8 W/cm^2. These intensities are sufficient to achieve the maximum shift with a single 10 s exposure. Figure 36b plots the cavity resonance after successive UV and green exposures for both the 35 nm and 55 nm thick coatings. The cavity can be shifted and reversed roughly three times before the tunability degrades too much for further significant shifts.

In conclusion, we have demonstrated a method for reversible tuning of photonic crystal cavity resonances using spiropyran photochromic thin films. The film enabled reversible tunings as large as 2.7 nm by successive exposures of UV and visible wavelength light with little degradation to the cavity *Q*. The performance of the film could be improved by incorporating photochromic materials that exhibit greater index changes and reversibility [124]. The photochromic films demonstrated here could add significant flexibility in nanophotonic design enabling reconfigurable optical chips with tunable components that be adjusted post-fabrication. With the film, we can also tune a cavity in and out of resonance with a narrowband light source such as a single quantum dot. This work can also be extended to other material systems like PbS quantum dots on AlGaAs membranes that have the potential to perform at room temperature.

Chapter 7

A reversibly tunable photonic crystal nanocavity laser using photochromic thin film

7.1 Overview of tunable laser

We demonstrate a reversibly tunable photonic crystal quantum dot laser using a photochromic thin film. The laser is composed of a photonic crystal cavity with a bare cavity Q as high as 4500 coupled to a high density ensemble of indium arsenide quantum dots. By depositing a thin layer of photochromic material on the photonic crystal cavities, the laser can be optically tuned smoothly and reversibly over a wavelength range of 2.68 nm. Lasing is observed at temperatures as high as 80 K in the 900-1000 nm near-infrared wavelength range. The spontaneous emission coupling factor is measured to be as high as β=0.41, indicating that the laser operates in the high-β regime.

Compact tunable lasers are an important enabling technology for a broad range of applications in optical communications and integrated optical data processing. Photonic crystals provide an ideal platform for implementing such lasers due to their ability to integrate a large number of optical components in a small chip-sized device [125-127]. These structures can be seeded by active materials such as quantum wells that offer high optical gain at room temperature [128] and quantum dots which exhibit high carrier confinement, low transparency carrier density, and small nonradiative decay rates [129,130]. The engineering of photonic crystal (PhC) cavities with high quality factors (Q) and small mode volumes seeded with a variety of active materials has resulted in the development of low threshold lasers with high emission efficiencies [131-140]. In addition, the strong optical confinement of photonic crystals enables lasing with a single QD emitter [141].

One of the primary limitations of photonic crystal lasers is that they are very difficult to tune locally after fabrication. Such local tuning is essential for integrated optical structures to ensure that individual optical components are resonantly excited. In addition, local tunability could enable the engineering of reconfigurable optical devices whose functionality can be modified post-fabrication. Photonic crystal structures can be tuned via temperature [22], gas deposition methods [118], but these methods are non-local and will tune all optical structures on the fabricated device simultaneously. Improved temperature tuning methods based on local heating pads have been demonstrated [142] and provide more localization but still require large spacing between optical components. Other techniques based on chalcogenide glass film deposition provide highly localized tunability but are not reversible [121]. Electrical tuning of photonic crystal laser with nematic liquid crystal infiltration has also been demonstrated [143]. More recently a novel laser based on a tapered fiber evanescently coupled to a photonic crystal nanobeam cavity has been shown to be reversibly tunable by up to 7 nm [13]. This technique relies on locally positioning a tapered fiber on a photonic crystal structure, making the extension to tuning of multiple closely packed devices challenging.

An alternate method for local reversible tuning of photonic crystal devices is using photochromic thin-films [144]. These films exhibit a reversible change in their index of refraction when irradiated by UV and visible light, enabling a highly controllable all-optical tuning of the cavity mode at near-infrared (NIR) wavelengths. By depositing these films on a photonic crystal cavity coupled to a low density of QD spontaneous emitters, reversible cavity-frequency tuning was observed through the fluorescence of the device. Here, we demonstrate a method for using these photochromic thin films to create a reversibly tunable photonic crystal laser. The laser consists of a cavity coupled to an active high gain medium composed of three high density quantum dot layers embedded in the device. The tuning method we present is both local and reversible, enabling the tuning of multiple closely spaced lasers on an integrated optical chip. We show that by controlling film thickness we can maintain a high bare cavity *Q* to support lasing while simultaneously achieving a sufficiently large modification of the effective index to enable a reversible tuning range of up to 2.68 nm.

7.2 Sample preparation

A schematic of the device used to realize the tunable laser is shown in Figure 37a. The initial wafer was comprised of a 160-nm gallium arsenide (GaAs) membrane with three layers of InAs QDs grown at the center (corresponding to a QD density of ~500 μm^{-2}), on a 1-μm thick sacrificial layer of aluminum gallium arsenide ($Al_{0.78}Ga_{0.22}As$). Photonic crystals were defined on the GaAs membrane using electron-beam lithography and chlorine-based inductively coupled plasma dry etching, followed by a selective wet etch to remove the sacrificial AlGaAs layer, resulting in a free-standing GaAs membrane. The cavity design used in this experiment was a three-hole linear defect (L3) cavity with three-hole tuning as shown in the fabricated device in Figure 37b. The parameter *a* was set to 240 nm and the hole diameter was varied between 130 nm and 160 nm to achieve cavity resonances across the QD gain bandwidth. The three holes at the edge of the cavity, labeled A, B, and C in the figure, were shifted by 0.176*a*, 0.024*a* and 0.176*a* respectively.

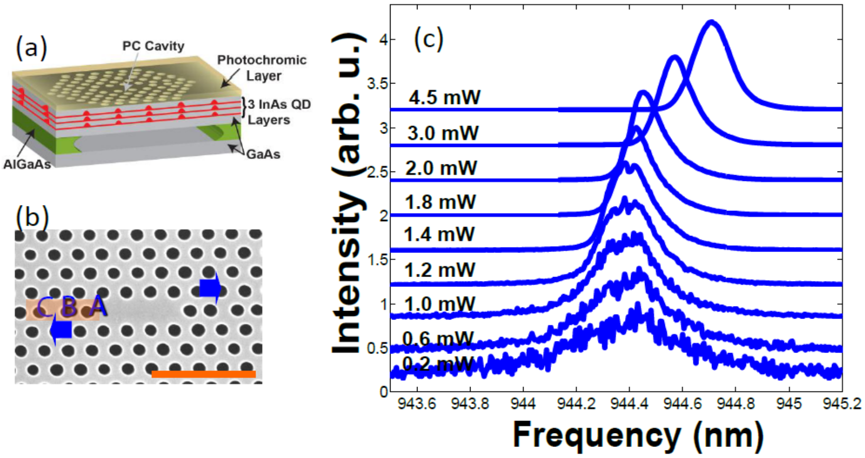

Figure 37 : a) Schematic showing the cross section of photonic crystal cavity laser with 3 QD layers embedded at the center of the GaAs slab. After fabrication, the photochromic thin-film is spun on the surface. b) SEM image of cavity with side holes A, B, C shifted. Scale bar: 1μm. c) Cavity emission spectrum of a typical device at 80 K recorded for increasing excitation powers using the 780 nm pump laser.

After fabricating the devices, the photochromic material was prepared as outlined in Ref. [144] by mixing 5 wt% 1,3,3-Trimethylindolinonaphthospirooxazine (TCI America) and 0.5 wt % 950 PMMA A4 dissolved in anisol. The polymer mixture was spun on the sample at a spinning rate of 3500 RPM, resulting in a film of 50 nm thickness. This thickness was found to be small enough to minimally affect the cavity quality factors while providing a sufficiently high index change to reversibly tune the resonances of the nanocavities. For device characterization, the fabricated structures were placed in a continuous-flow liquid He cryostat and cooled to a temperature ranging between 20K and 80 K. In order to observe lasing, the QDs in the cavity region were excited above-band by a continuous wave titanium sapphire laser tuned to 780 nm wavelength. Emission was collected by a confocal microscope setup using a 0.7 NA objective lens and measured by a grating spectrometer with a wavelength resolution of 0.02 nm.

Upon exciting the cavity with the 780 nm pump laser, a bright narrowband emission is observed from the cavity, as shown in Figure 37c. This figure shows several representative spectra for the cavity emission with increasing pump powers at 80K. As the pumping power is increased, there is a visible change in the output emission spectrum from a broad emission to a sharp narrowband lasing emission. The small shift of 0.3 nm in the cavity mode emission with increasing power is due to thermal effects caused by above band pumping.

7.3 Input-Output characteristics of the laser

In order to verify that the bright emission from the cavity mode is due to lasing, we investigate both the output power and linewidth of the cavity emission as a function of pump power. The measurement results are shown in Figure 38. Figure 38a plots the cavity output power (red circles) and linewidth (green diamonds) as a function of input pump power at 20 K temperature where the QD linewidth is minimally perturbed by phonon broadening. The cavity output power curve, commonly referred to as the light-in light-out (L-L) curve, exhibits a clear threshold behavior in that the emitted light power rapidly increases when the pump power exceeds a critical value. Well above threshold the output power is linearly increasing with pump power, as expected from standard laser theory. To estimate the pumping threshold we extrapolate the linear region of the L-L curve to determine the x-intercept. Using this method, we estimate the lasing threshold to be 80μW at 20K.

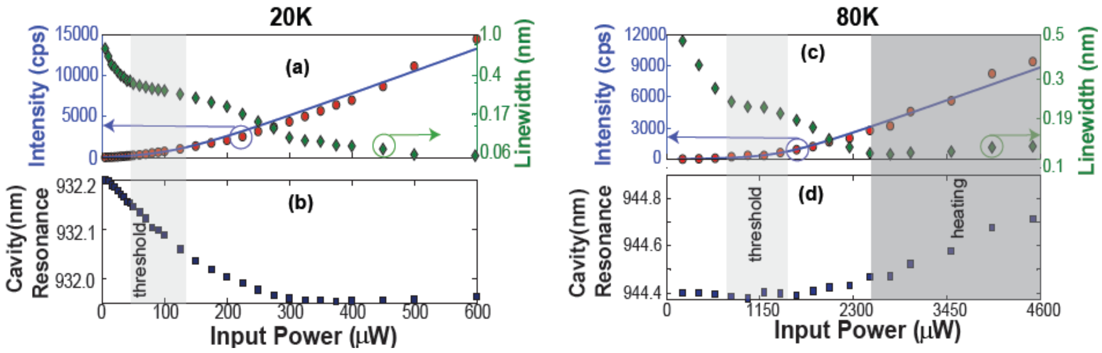

Figure 38 : (a) Laser output intensity (red circles) and linewidth (green diamonds) as function of input power at 20K. The blue line represents the theoretical fit to the cavity intensity using Eq. (1). (b) Cavity resonance as a function of input power at 20K (c) Laser output intensity (red circles) and linewidth (green diamonds) as function of input power at 80K. The blue line represents the theoretical fit to the cavity intensity using Eq. (1). (d) Cavity resonance as a function of input power at 80K

An important signature of lasing is the dependence of linewidth of the laser emission on the pump power. In a microcavity laser, the linewidth is expected to initially decrease due to absorption saturation, then increase near threshold due to gain-refractive index coupling, and finally decrease again due to onset of stimulated emission [140,145-147]. For microcavity lasers with high spontaneous emission coupling factors the linewidth broadening near threshold is small and is usually observed as a plateau rather than an increase [135,148]. The emission linewidth of the laser, shown in Figure 38a, is calculated by fitting the spectrum at each pumping power to a Lorentzian. The linewidth exhibits an initial drop from the absorption limited linewidth of 0.73 nm (*Q*=1300) to a cavity linewidth of 0.31 nm followed by a plateau right at threshold. From the linewidth at the threshold power we estimate the bare cavity *Q* to be 3100, which corresponds to a bare cavity decay rate of κ=0.31nm. The experimentally measured bare cavity *Q* is limited by a combination of fabrication errors and degradation in Q due to the photochromic film. The linewidth then continues to decrease beyond the threshold region, as expected from standard microcavity laser theory.

An important figure of merit for a microcavity laser is the spontaneous emission coupling factor β, defined as the percentage of spontaneous emission that couples to the lasing mode. This parameter can be extracted from the L-L curve. Using a simple rate equation model, the relation between the input power P_{in} and output power P_{out} is given by [149]:

$$P_{in} = \frac{\hbar\omega\kappa}{\beta\eta}\left[\frac{p}{1+p}(1+\xi)(1+\beta p) - \xi\beta p\right] \tag{7.1}$$

where κ is the decay rate of the cavity, ω is the cavity resonant frequency, $p = P_{out}/\hbar\omega\kappa$ is the photon number in the cavity and η is the coupling efficiency. The parameter ξ is a dimensionless parameter which scales as the ratio of the phonon dephasing rate to the spontaneous emission rate of the QDs. We fit the measured L-L curve to the above equation, treating β, ξ and η as fitting parameters, and setting κ to the decay rate calculated from the emission linewidth at threshold. The best fit, shown as a solid curves in Figure 38a, is attained for β=0.41, indicating that the laser operates in the high β regime.

In Figure 38b we plot the resonance wavelength of the cavity mode as a function of pump power. As the pump power is increased, the cavity resonance blue shifts as threshold is approached, then reaches a stable value which is shifted by 0.25 nm from the initial low pump power regime. This blue shift may be attributed to the change in refractive index of the cavity medium due to the injection of free carriers [150].

Figure 38c shows the L-L curve, linewidth, and cavity center wavelength for a different device that was maintained at 80 K. At this temperature the lasing threshold is measured to be 920 μW, which is higher than the threshold for the device measured at 20 K. The higher lasing threshold is expected due to increased dephasing and non-radiative decay of the QDs. The linewidth of the cavity decreases from its absorption limited initial value of 0.5 nm to 0.21 nm (Q ~ 4500), followed by a plateau at threshold. The linewidth then continues to decrease beyond the threshold and reaches its minimal value of 0.1 nm at a pump power of 2.75mw. At pumping powers beyond 2.75mw the linewidth begins to increase again. At the same point the center wavelength of the cavity begins to red-shift. The increase in linewidth and simultaneous red-shift of the cavity wavelength is attributed to cavity heating and has been observed in previous works [136,151]. In contrast, the device measured at 20 K exhibited no such heating due to the lower threshold which enabled us to pump it at lower pump powers.

7.4 Photochromic tuning of laser

The tunability of our photonic crystal laser is enabled by the changing index of refraction of the photochromic thin film with UV or visible light irradiation [122]. The properties of the photochromic film have been reported in chapter 6. We investigate the tunability of the laser by first exposing the cavity structure to 375 nm UV light generated from the second harmonic of a pulsed Ti:Sapphire laser. The cavity was irradiated by a UV intensity of 3 kW/cm^2 for a period of 50 s, while the emission spectrum was monitored by the spectrometer. The intensity of the UV light was set to be sufficiently low so that the laser was tuned slowly over its entire range during the 50 s exposure (the shifting rate can be significantly increased by increasing the UV intensity [152]). The spectrometer acquired and saved the entire emission spectrum every 500 ms during the exposure period. Figure 39a shows several snapshots of the laser emission spectrum from the cavity taken at different times during this exposure. UV irradiation at the cavity increased the index of refraction resulting in a continuous red shift over the 50 s exposure period. At any time during the tuning process, blocking the UV laser maintained the laser emission at that wavelength.

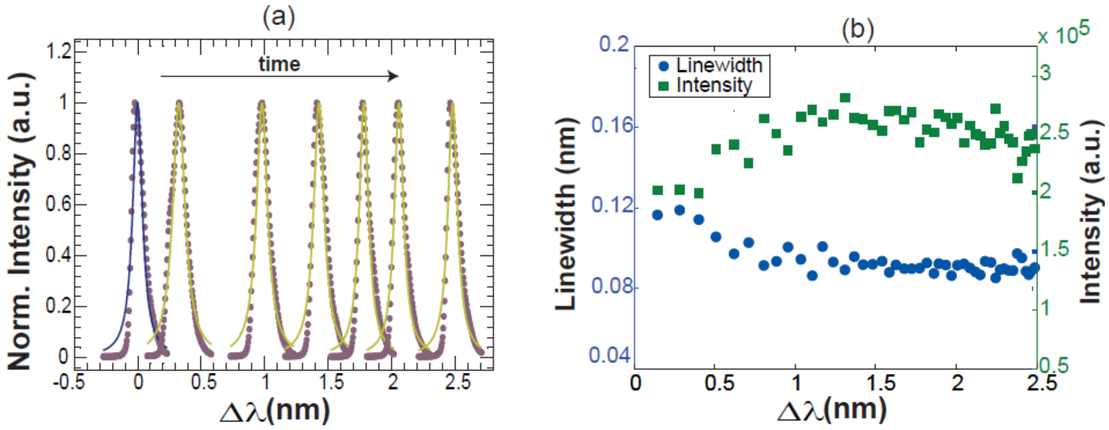

Figure 39 : (a) Cavity emission spectra (solid circles) recorded as a function of photochromic tuning from initial resonance using UV radiation, with Lorentzian fits (solid lines). (b) Linewidth (blue circles) and intensity (green squares) of the photochromic laser as a function of tuning from initial resonance, derived from the same scan as (a).

Each spectrum acquired over the 50 s tuning window was fit to a Lorentzian in order to extract the linewidth, center frequency and intensity. The Lorentzian fits for the different snapshots shown in Figure 39a are plotted as solid lines. Figure 39b plots both the linewidth and integrated lasing emission intensity as a function of emission wavelength shift over a 2.5 nm tuning range. We observe that the power output of the laser is stable over the photochromic tuning process with fluctuations of less than 10%. The cavity mode linewidth also stays near the threshold value of 0.10 during the tuning process. The variations in the linewidth and intensity for the first few steps of photochromic tuning are likely caused by slight drifts in the cavity position due to vibrations in the optical setup. Because our pump laser was highly focused, drift in the cavity caused it to be pumped less hard resulting in an increase in linewidth and a simultaneous decrease in output intensity. In general, the lasing mode spectrum was found to be highly sensitive to the excitation spot of the 780 nm laser**.**

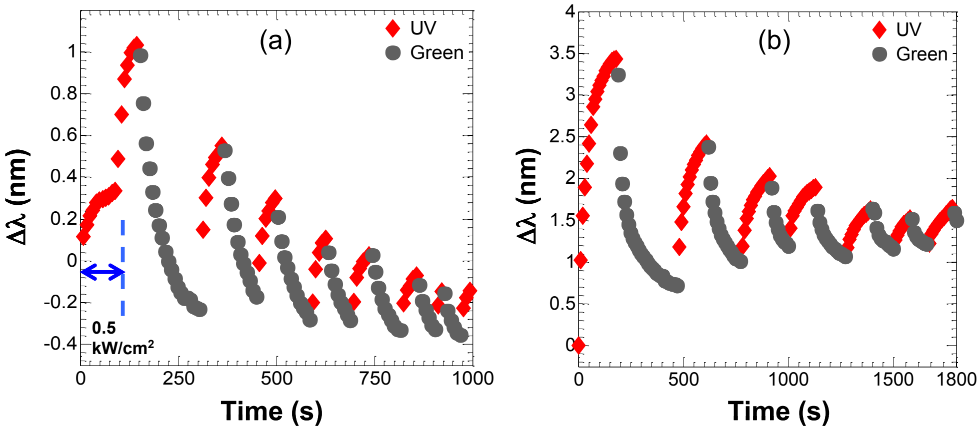

Figure 40 : Tunability of the photonic crystal quantum dot laser at (a) 20 K and (b) 80K. Regions corresponding to UV exposure are shown by diamonds. Green exposure is shown by gray circles. The average pump intensity for UV and green are 3 kW/cm^2 except for the region shown by arrows where 0.5 kW/cm^2 was used.

Having demonstrated the ability to continuously red-shift the cavity resonance, we next investigate the reversibility of the tuning processes. Reversibility is accomplished by irradiating the photonic crystal cavity by green light from a frequency-doubled Nd:YAG laser with an emission wavelength of 532 nm and at an intensity of 3 kW/cm^2. In Figure 40a and 40b, we show the reversibility of the photochromic tuning process at 20 K and 80 K. The cavity mode spectrum is shown at 6 (8) second- intervals at 20 (80) K while the cavity was exposed to UV or green radiation. Diamonds represent regions when the UV was turned on while the green laser was turned off. Circles represent regions when the green laser was turned on while the UV laser was turned off. After the initial UV exposure, the cavity mode red-shifted with a maximum red-tuning range of 1 nm at 20K and 3.4 nm at 80K. The tuning range at 20K is lower than the tuning range at 80K due to the lower conversion efficiency from the spiropyran to the merocyanine states at low temperatures [153]. After UV exposure the green laser was turned on in order to blue-shift the cavity mode. At the end of the first green exposure, we observe that the cavity shifted back for an overall detuning of -0.23 nm (+0.72 nm) from the initial resonance at 20K (80K). This shift corresponds to a maximum reversible tuning range of 1.23 nm for 20 K operation and 2.68 nm for 80 K operation.

7.5 Limitations of photochromic tuning

One limitation of spiropyran-based photochromic films is that the reversibility fatigues over repeated cycles, reducing the range over which the device can be tuned. This fatigue can be readily observed both at 20 K and 80 K through a decrease in the tunability with successive exposures. After four consecutive cycles of red and blue shifting, the reversible tuning range, defined as the wavelength range over which the laser is reversibly tunable in each UV-green cycle, is reduced from its maximum value of 1.23 nm to 0.38 nm at 20 K, while at 80 K it is reduced from 2.68 nm to 0.83 nm. Both cases represent a 70 % reduction of the maximum tuning range on the fourth cycle. Once the film has fatigued, it can be removed with acetone and a new film can be spun without destroying the device itself.

In conclusion, we have demonstrated a locally and reversibly tunable near-infrared photonic crystal laser with high beta factors (0.14-0.41). Tunability was achieved using a photochromic thin-film that was spun onto the sample surface. The resulting bare cavity *Q*s were measured to be as high as 4500, while lasing threshold was achieved at pump powers of 80μW at 20 K and 920μW at 80K. The reversible tuning range of the device was measured to be 1.23 nm at 20 K and 2.68 nm at 80 K, while the maximum tuning range was measured to be 3.4 nm. The photochromic tuning process was found to maintain a stable output power emission linewidth over the entire tuning range of the device. Larger tuning could be potentially achieved at higher temperatures using a different gain medium such as quantum wells that can support room temperature operation. Further device improvements in reversibility and tuning range could be attained by using other photochromic materials that exhibit better reversibility over hundreds of tuning cycles [154,155]. Furthermore, the method we demonstrate for reversible tuning is not restricted to photonic crystals, and could be applied to a broad range of other photonic structures such as microdisks and distributed feedback structures in a straightforward way. The combination of photochromics with integrated devices could open up the possibility for integration of tunable lasers, filters, beamsplitters, and other optical components to create highly reconfigurable photonic systems, with applications in optical communications and optical computation.

Chapter 8

Generating entanglement between quantum dots with different resonant frequencies based on Dipole Induced Transparency

8.1 Entanglement with Quantum Dots

We describe a method for generating entanglement between two spatially separated dipoles coupled to optical micro-cavities. The protocol works even when the dipoles have different resonant frequencies and radiative lifetimes. This method is particularly important for solid-state emitters, such as quantum dots, which suffer from large inhomogeneous broadening. We show that high fidelities can be obtained over a large dipole detuning range without significant loss of efficiency. We analyze the effects of non-idealities such as imperfect cavity transmission, and show that the protocol is robust to these imperfections.

Generation of entanglement between qubits is an important operation for a large variety of applications in quantum information processing. Such states can be used to the realize schemes such as transmission of secret messages via quantum key distribution [156,157] and teleportation of quantum information [158-161]. The exchange of entanglement between two distant parties is also required for implementation of quantum repeaters [61] which use a combination of entanglement swapping and entanglement purification to achieve unconditional secure communication over arbitrarily long distances.

To date, a variety of methods have been proposed for creating entanglement between spatially separated nodes. One of the most common methods is to transmit entangled photons generated by parametric down-conversion [162]. Entanglement protocols for atomic systems have also been proposed [59,163-165]. Atom entanglement has the advantages that quantum information can be stored for long time periods, which is important for long distance quantum networking.

Semiconductor based approaches to quantum information processing are currently an area of great interest because they offer the potential for a compact and scalable quantum information architecture. Solid-state emitters, such as semiconductor quantum dots (QDs), can be coupled to ultra compact cavity waveguide systems to form integrated waveguide systems [30,31,166,167].

A major challenge in using solid-state emitters is that they suffer from enormous inhomogeneous broadening, typically caused by emitter size variation and strain fields in the host material. The inhomogeneous broadening makes it difficult to find two identical emitters. Previous protocols for generating atom entanglement require the dipoles to emit indistinguishable photons, and are thus difficult to implement in semiconductor systems.

Here, we describe a protocol for creating entanglement between two dipoles with different radiative properties. This property is extremely important for semiconductor systems. The proposed protocol uses Dipole Induced Transparency (DIT) to achieve the desired entanglement which occurs when a dipole is coupled to an optical cavity [57]. When the coupling is sufficiently strong, the dipole can switch a cavity from being highly transmitting to highly reflecting. The switching contrast is determined by the Purcell Factor, which is the ratio of the lifetime of the bare emitter in free space to the modified lifetime of the cavity-coupled emitter. Purcell enhancement has been observed in semiconductor emitters coupled to a variety of different micro-cavity architectures [22,31,117,168,169].

8.2 Protocol for entanglement generation

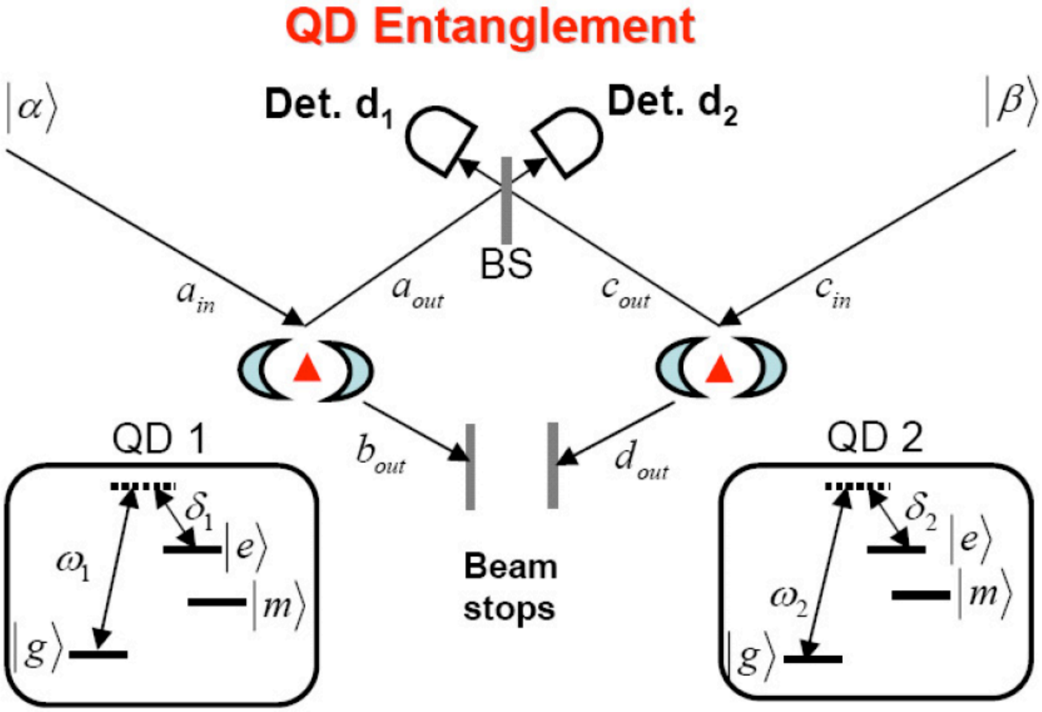

Figure 41: Schematic of QD-QD entanglement protocol

The schematic for generating entanglement between two spatially separated quantum dots is shown in Figure 41. Each qubit consists of a quantum dot coupled to a double sided cavity. Each quantum dot is assumed to have three states: a ground state, a long lived metastable state and an excited state, which we refer to as $|g\rangle$, $|m\rangle$ and $|e\rangle$ respectively. The states $|g\rangle$ and $|m\rangle$ represent the two qubit states of each QD. The transition from the ground state to the excited state for QD1 may be detuned by δ_1 from the resonant frequency ω_1 of cavity 1. Similarly, the transition from the ground state to the excited state for QD2 may be detuned by δ_2 from the resonant frequency ω_2 of cavity 2.

In Figure 41, the state $\left|m\right\rangle$ is shown to be lying between the ground and excited states. In general, this does not have to be the case. State $\left|m\right\rangle$ can be anywhere in energy level as long as the transition from the metastable state to the excited state is decoupled from g-e transition. One way to achieve this decoupling is by spectral detuning, wherein the m-e transition frequency is far detuned from the g-e transition. Another way to achieve this is to reduce the dipole transition strength of the m-e transition by spin selection rules.

The three level systems described above can be realized in a variety of ways. One way to achieve them in QDs is by making use of excitonic and biexcitonic transitions [170]. They can also be realized in QDs using spin based bright and dark states [171]. In addition, three level structures can also be achieved using quantum-dot molecules [172], charged quantum dots [173] and impurity bound excitons [174]. Similar qubits states can also been realized in diamond, using neutral and negatively charged nitrogen vacancy defects [175,176]. We assume both the QDs to have the same decay rate γ. The operators $\hat{\boldsymbol{\sigma}}_{\mathbf{1}-}$ and $\hat{\boldsymbol{\sigma}}_{\mathbf{2}-}$ represent the dipole lowering operators for the QDs in cavities 1 and 2 respectively. We define $\hat{\mathbf{a}}_{in}$ and $\hat{\mathbf{c}}_{in}$ as the two input modes to the cavity, $\hat{\mathbf{a}}_{out}$ and $\hat{\mathbf{c}}_{out}$ as the reflected modes, and $\hat{\mathbf{b}}_{out}$ and $\hat{\mathbf{d}}_{out}$ as the transmitted modes. The energy decay rate of the cavities into the reflected and transmitted modes is κ. The field inside the cavities is given by the cavity field operators $\hat{\mathbf{f}}_1$ and $\hat{\mathbf{f}}_2$.

The protocol works as follows. Both the quantum dots are initialized to be in an equal superposition of qubit states $\left|g\right\rangle$ and $\left|m\right\rangle$. Thus, the initial state of the quantum dots is $1/2(|gg\rangle + |mm\rangle + |gm\rangle + |mg\rangle)$. The initialization of the QDs in a superposition of $|g\rangle$ and $|m\rangle$ states requires coherent control of the QDs. The initial state can be prepared by a preparation pulse which is a bright coherent pulse. The intensity of the pulse should be selected to correspond to a $\pi/2$ rotation between the two qubit states. After the initialization of the QDs, a weak coherent field $|\alpha\rangle$ with frequency ω is inserted at input $\hat{\mathbf{a}}_{in}$. Simultaneously, another weak coherent field $|\beta\rangle$ with frequency ω is input at $\hat{\mathbf{c}}_{in}$. The fields at $\hat{\mathbf{a}}_{in}$ and $\hat{\mathbf{c}}_{in}$ are created by the bosonic creation operators $\hat{\mathbf{a}}_{in}^{\dagger}$ and $\hat{\mathbf{c}}_{in}^{\dagger}$ respectively. These input fields interact with the cavity-dipole system. The interaction between the input field $\hat{\mathbf{a}}_{in}$ and cavity-dipole system 1 can be characterized by the Heisenberg's equations of motion for the cavity field operator $\hat{\mathbf{f}}_1$ and the dipole lowering operator $\hat{\boldsymbol{\sigma}}_{\mathbf{1-}}$

$$\frac{d\hat{\mathbf{f}}_1}{dt} = -(i\omega_0 + \kappa)\hat{\mathbf{f}}_1 - \sqrt{\kappa}\hat{\mathbf{a}}_{\mathbf{in}} - ig\boldsymbol{\sigma}_{\mathbf{1-}} \tag{8.1}$$

$$\frac{d\hat{\boldsymbol{\sigma}}_{\mathbf{1-}}}{dt} = (-i(\omega_0 + \delta_1) + \gamma)\boldsymbol{\sigma}_{-} + ig\sigma_z\hat{\mathbf{f}}_1 \tag{8.2}$$

Similar equations can also be written for the interaction of the input field $\hat{\mathbf{c}}_{in}$ with cavity-dipole system 2. The interaction between the input fields and the cavity-dipole systems results in part of the field being transmitted into the modes $\hat{\mathbf{b}}_{out}^{\dagger}$ and $\hat{\mathbf{d}}_{out}^{\dagger}$ and reflected into the modes $\hat{\mathbf{a}}_{out}^{\dagger}$ and $\hat{\mathbf{c}}_{out}^{\dagger}$. The amount of light reflected and transmitted is given by the cavity reflection and transmission coefficients.

Our analysis works in the weak excitation limit, where predominantly the quantum dots are populated in the ground state. In this limit, $\langle \sigma_z(t) \rangle \approx -1$. Using this limit in Eqs. 8.1 and 8.2, we can derive the reflection and transmission coefficients to be

$$r_{1,2}(\omega) = \frac{(-i\Delta\omega_{1,2} + \dfrac{g^2}{-i(\Delta\omega_{1,2} - \delta_{1,2}) + \gamma})}{(-i\Delta\omega_{1,2} + \kappa + \dfrac{g^2}{-i(\Delta\omega_{1,2} - \delta_{1,2}) + \gamma})} \tag{8.3}$$

$$t_{1,2}(\omega) = \frac{\kappa}{(-i\Delta\omega_{1,2} + \kappa + \dfrac{g^2}{-i(\Delta\omega_{1,2} - \delta_{1,2}) + \gamma})} \tag{8.4}$$

Subscript 1 denotes cavity-dipole system 1 and subscript 2 denotes cavity-dipole system 2. Thus, $\Delta\omega_1 = \omega - \omega_1$ and $\Delta\omega_2 = \omega - \omega_2$ the cavity reflection and transmission coefficients depend on the state and detuning of the dipoles. The state of the dipoles is indicated by the parameter g in the Eq 8.1, which represents the coupling between the field and the dipole. When the dipoles are in state $|g\rangle$, the input field couples to the cavity-dipole system and g is set to be equal to the vacuum Rabi frequency of the dipole.

When the dipoles are in state $|g\rangle$, the reflected fields are given by $\hat{a}^{\dagger}_{out} = \mathrm{r}_1^g(\omega)\hat{a}^{\dagger}_{in}$ and $\hat{c}^{\dagger}_{out} = \mathrm{r}_2^g(\omega)\hat{c}^{\dagger}_{in}$ and the transmitted fields are given by $\hat{b}^{\dagger}_{out} = \mathrm{t}_1^g(\omega)\hat{a}^{\dagger}_{in}$ and $\hat{d}^{\dagger}_{out} = \mathrm{t}_2^g(\omega)\hat{c}^{\dagger}_{in}$. We can obtain the reflection coefficients r_1^g and r_2^g and transmission coefficients t_1^g and t_2^g by substituting the vacuum Rabi frequency for g in Eq 8.1.

When the dipoles are in state $|m\rangle$, the field does not couple to the dipole transition from $|m\rangle$ to $|e\rangle$ and g is set to 0. The reflected fields are given by $\hat{a}_{out}^{\dagger} = \mathrm{r}_1^m(\omega)\hat{a}_{in}^{\dagger}$ and $\hat{c}_{out}^{\dagger} = \mathrm{r}_2^m(\omega)\hat{c}_{in}^{\dagger}$ and the transmitted fields are given by $\hat{b}_{out}^{\dagger} = \mathrm{t}_1^m(\omega)\hat{a}_{in}^{\dagger}$ and $\hat{d}_{out}^{\dagger} = \mathrm{t}_2^m(\omega)\hat{c}_{in}^{\dagger}$. We can obtain the reflection coefficients r_1^m and r_2^m and transmission coefficients t_1^m and t_2^m by substituting 0 for g in Eqs 8.3 and 8.4. When the quantum dots are resonant with the cavity ($\delta_1 = \delta_2 = 0$), we have $r_1^g = r_2^g = C/(1+C)$ and $r_1^m = r_2^m = 0$. The constant $C = g^2/\gamma\kappa$ is called the atomic cooperativity index. It is the ratio of the cavity coupled dipole decay rate g^2/κ to the bare dipole decay rate γ within the cavity. Here, it is more useful to define atomic cooperativities rather than Purcell factors. Purcell factors measure the enhancement in emission rate of QDs within cavities to bulk emission. The emission of QDs in bulk is due to both radiative and non radiative decay. However according to our definition of γ, it is the dipole decay rate within the cavity. Therefore, it is dominated by nonradiative mechanisms and weak coupling to the leaky modes. Hence, the Purcell factor underestimates the spontaneous emission enhancement rate and is not a very useful figure of merit for this work.

When $C >> 1$ we have $r_1^g = r_2^g = 1$. Thus, for high atomic cooperativity indices, when the dipole is in state $|g\rangle$, the field is completely reflected and when it is in state $|m\rangle$, the field is completely transmitted. Thus, we need to achieve a large C to achieve higher transparency. However, we do not need the full normal mode splitting condition $g > \kappa$, which represents the onset of strong coupling between the quantum dot and the cavity. It is to be noted that the equations for reflectivity and transmittivity are complete and valid irrespective of whether we are in the strong or weak coupling regime.

For the calculations in this section, we use parameters that are appropriate for InAs quantum dots coupled to photonic crystal defect cavities. We set $\kappa =$ 100 GHz which corresponds to a cavity Q of 3300. We set g = 20 GHz for both the quantum dots. We estimate dipole decay rate γ within the cavity to be 0.125 GHz, using the lifetime of several quantum dots that are placed inside a photonic crystal cavity, but heavily detuned to be 7.96 ns. We calculate C to be 32 and the cavity-dipole systems to be 96.7% reflective on resonance. For the chosen values of g and κ, the cavity-dipole systems are in the weak coupling regime. However, this analysis is completely general and is equally valid also for the strong coupling regime.

We first investigate the protocol under the assumptions that the resonant frequencies of both the cavities are the same ($\omega_1 = \omega_2$), and the fields are sufficiently weak that we may expand them to first order in photon number. In the later sections, we will investigate how higher order photon numbers and cavity mismatch affect the protocol. Since the coherent fields can be expanded to first order in photon number, the initial state of the system (dipoles and fields) is given by

$$\left|\Psi_i\right\rangle = 1/2(\left|gg\right\rangle + \left|mm\right\rangle + \left|gm\right\rangle + \left|mg\right\rangle)(\alpha\hat{a}_{in}^{\dagger} + \beta\hat{c}_{in}^{\dagger}) \tag{8.5}$$

The fields, after interacting with the cavities, are transformed according to cavity reflection and transmission coefficients. The reflected field from the two cavities is mixed on a 50/50 beam splitter that applies the transformation:

$$\hat{\mathbf{a}}^{\dagger}_{out} \rightarrow (\hat{\mathbf{d}}_1 + \hat{\mathbf{d}}_2)/\sqrt{2}, \hat{\mathbf{c}}^{\dagger}_{out} \rightarrow (\hat{\mathbf{d}}_1 - \hat{\mathbf{d}}_2)/\sqrt{2} \tag{8.6}$$

The final state of the QDs can be obtained by applying the cavity and beamsplitter transformations. If a detection event is observed in detector $\hat{\mathbf{d}}_2$, then the state of the two QDs collapses to

$$\left|\Psi_f\right\rangle = \frac{1}{N}[(\alpha r_1^g - \beta r_2^g)\left|gg\right\rangle + \alpha r_1^g \left|gm\right\rangle - \beta r_2^g \left|mg\right\rangle \tag{8.7}$$

where $N^2 = |\alpha r_1^g - \beta r_2^g|^2 + |\alpha r_1^g|^2 + |\beta r_2^g|^2$. In general, $r_1^g \neq r_2^g$ because the QDs have different resonant frequencies. However, we can correct for this mismatch by properly selecting the amplitudes of the fields. The amplitudes are selected such that

$$\alpha r_1^g = \beta r_2^g \tag{8.8}$$

In this case, the state of the qubits is projected onto

$$\left|\Psi_-\right\rangle = (\left|gm\right\rangle - \left|mg\right\rangle)/\sqrt{2} \tag{8.9}$$

which is an ideal entangled state. Thus, by properly choosing the amplitude and phase of the input coherent fields $\left|\alpha\right\rangle$ and $\left|\beta\right\rangle$, we ensure that a detection at $\hat{\mathbf{d}}_2$ creates an entangled state of QDs.

8.3 Higher order photon numbers

The matching condition $\alpha r_1^g = \beta r_2^g$ gives a relationship between α and β, but does not tell us how large to make α. In general, we want to make $|\alpha|^2$ as large as possible to improve the chances of a detection event at $\hat{\mathbf{d}}_2$. The probability of detecting a photon at detector $\hat{\mathbf{d}}_2$ is defined as the efficiency η of the protocol. When the fields $\left|\alpha\right\rangle$ and $\left|\beta\right\rangle$ are weak, efficiency of the protocol is proportional to the intensity of the field at $\hat{\mathbf{d}}_2$ and can be derived to be $|\alpha r_1^g|^2/4$. The factor 0.25 appears because 50% is transmitted into the transmitted modes $\hat{\mathbf{b}}_{out}^\dagger$ and $\hat{\mathbf{d}}_{out}^\dagger$ and another 50% is lost when the beamsplitter splits the photons equally between $\hat{\mathbf{d}}_1$ and $\hat{\mathbf{d}}_2$. We see that we can achieve higher efficiencies by increasing input photon flux rate $|\alpha|^2$. However, if we make α too large we will eventually not be in the weak field limit and higher order photon number contributions will become important. In the ideal case, only one photon of $\left|\alpha\right\rangle$ and one photon of $\left|\beta\right\rangle$ interact with cavity-dipole systems 1 and 2 respectively. Depending upon the state of the dipoles, we either register a detection event at $\hat{\mathbf{d}}_2$ or not. Thus, the information about the state of the dipoles is contained entirely in the photon and no residual "which-path" information is left in the system.

Now suppose we consider the second order process of simultaneously injecting two photons injected into the input ports $\left|\alpha\right\rangle$ and $\left|\beta\right\rangle$. In the ideal case (both QDs are on resonance with the cavities), if the state of the two QDs is $\left|gm\right\rangle$, cavity 1 will reflect its incident photon while cavity 2 will transmit the second photon. The transmitted photon in cavity 2 will always keep track of the fact that QD 2 was in state $\left|m\right\rangle$, and this information cannot be erased by the beamsplitter. Thus, we expect the state to be completely decohered when this happens.

We will now consider not only this specific case, but all the higher order expansions of α and β in the coherent fields to see how the final state of the system is affected. The initial state of the system is given by

$$|\Psi_i\rangle = 1/2(|gg\rangle + |mm\rangle + |gm\rangle + |mg\rangle|\alpha\rangle|\beta\rangle \tag{8.10}$$

The coherent states $|\alpha\rangle$ and $|\beta\rangle$ can also be written as $|\alpha\rangle = D_1(\alpha)|0\rangle$ and $|\beta\rangle = D_2(\beta)|0\rangle$. D_1 and D_2 are the displacement operators and are given by

$$D_1(\alpha) = e^{\alpha \hat{a}_{in}^{\dagger} - \alpha^* \hat{a}_{in}} \tag{8.11}$$

$$D_2(\beta) = e^{\beta \hat{c}_{in}^{\dagger} - \beta^* \hat{c}_{in}} \tag{8.12}$$

The displacement operator is another way of writing the coherent states. It includes all the higher order photon numbers of α and β in their coherent fields. The final state of system $|\Psi_f\rangle$ is obtained by applying the cavity and beamsplitter transformations to the initial state $|\Psi_i\rangle$. After applying the transformations, the final state of the QDs is obtained by tracing out over the photon fields and is described by the reduced density matrix

$$\rho_{dipoles} = \frac{tr_{(\text{fields})}\{\langle M \,|\, \Psi_f\rangle\langle\Psi_f \,|\, M\rangle\}}{tr_{(\text{dipoles \& fields})}\{\langle M \,|\, \Psi_f\rangle\langle\Psi_f \,|\, M\rangle\}} \tag{8.13}$$

The matrix M is mathematically defined as $\sum_{n=1}^{\infty} |n_{d_2}\rangle\langle n|$. It is called a projection matrix, because it projects the state of the system onto a subspace containing at least one photon in $\hat{d}_2$. This projection accounts for the photon counter, which registers a detection event if there is at least one photon in mode $\hat{d}_2$. Since the final state of QDs is mixed, we need a figure of merit to measure how well the QDs are entangled. In this chapter we use the fidelity, which is defined as the overlap integral between the desired final state and the actual final state of the system. In our protocol, the desired final state is the maximally entangled Bell state $|\Psi_-\rangle$. Thus, the expression for fidelity is $\langle\Psi_-|\rho_{dipoles}|\Psi_-\rangle$. If the actual final state is same as the desired final state, we have a perfect entangled state and fidelity of 1. A fidelity of 0.5 implies that the state of the QDs is a random mixture of $|gm\rangle$ and $|mg\rangle$ and completely decohered. If the fields are not weak, the previous expression for efficiency $|\alpha r_1^g|^2/4$ is not valid. Using the definition for efficiency as the probability of getting detection at detector $\hat{d}_2$, the mathematical expression for it is

$$tr_{(\text{dipoles \& fields})}\{\langle M|\Psi_f\rangle\langle\Psi_f|M\rangle\} \tag{8.14}$$

Using the matching condition $\alpha r_1^g = \beta r_2^g$, the expression can be simplified to $\eta = 0.5(1 - e^{|\alpha r_1^g|^2/2})$

In Figure 42, we plot both fidelity and efficiency as a function of $|\alpha r_1^g|^2$. Fidelity is plotted for four values of δ_1, ranging from 0 to 100 GHz, with δ_2 fixed at 0. Note that the efficiency is only a function of $|\alpha r_1^g|$, so the plot of efficiency is the same for all values of δ_1. From Figure 42, we see that there is a tradeoff between fidelity and efficiency as we increase α. When $|\alpha r_1^g|^2 << 1$ the fidelity is close to 1, indicating an ideal entangled state, which is consistent with our predictions in the weak field limit.

In the region $0.1 < |\alpha r_1^g|^2 < 1$, the fidelity quickly drops due to the presence of higher photon number contributions. In the limit $|\alpha r_1^g|^2 >> 1$, the fidelity asymptotically approaches 0.5, indicating the higher photon number contributions have completely decohered the state. When $|\alpha r_1^g|^2 << 1$, the fidelity curves for different values of δ_1 nearly overlap. Fidelity stays close to 1 in this region.

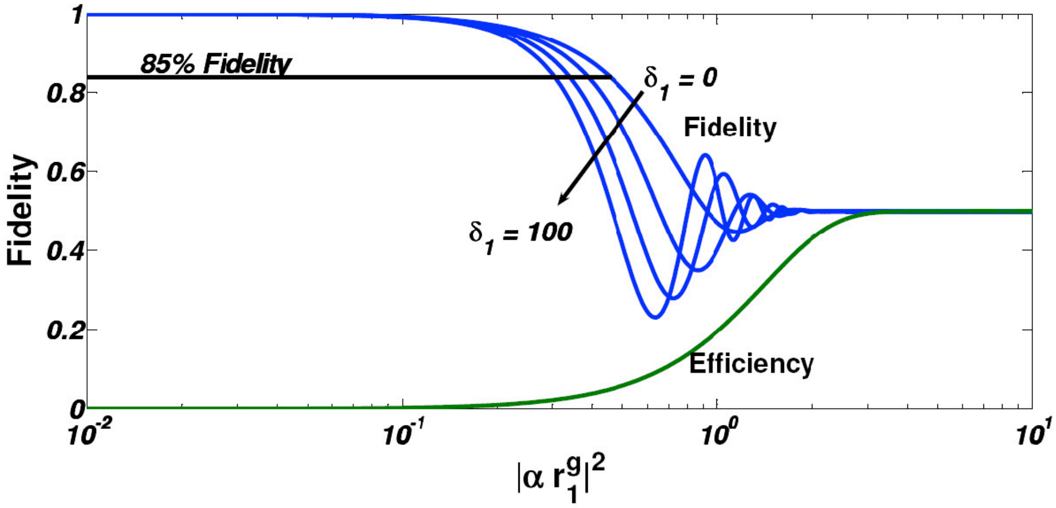

Figure 42 : Variation of fidelity and efficiency with $\left|\alpha r_1^g\right|^2$ for different values of δ_1

However, in the region $0.1 < |\alpha|^2 < 1$, the fidelity curves for different values of δ_1 separate out. There is a drop in fidelity with increase in dipole detuning from $\delta_1 = 0$ to $\delta_1 = 100\,\text{GHz}$. Also, efficiency is a function of $|\alpha r_1^g|$ alone and does not change with δ_1. This implies that fidelity decreases with increase in dipole detuning for a constant efficiency. In Figure 42, we also plot a line of constant fidelity of 0.85. Note that for every value of δ_1 there is a unique point on the plot corresponding to a fidelity of 0.85. As δ_1 increases, this point shifts to lower values of $|\alpha r_1^g|^2$. Since, efficiency is a function of $|\alpha r_1^g|$, this in turn implies a decrease in efficiency. Thus, it is important to consider how the efficiency of the protocol changes for a fixed value of fidelity.

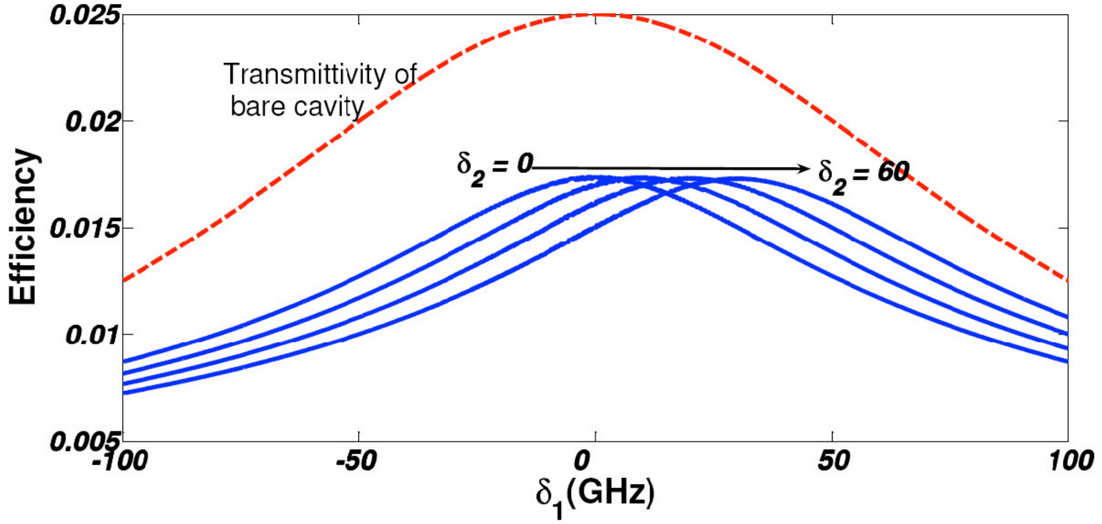

Figure 43 : Efficiency as a function of δ_1/κ for different values of $\delta_2 = 0$. Fidelity is fixed at 0.85

To investigate this, we plot efficiency as a function of δ_1 for several values of δ_2 for a constant fidelity of 0.85 in Figure 43. The solid lines plot efficiency, while the dashed line plots the cavity transmission spectrum. This spectrum is plotted as a reference, so that one can compare where the dipole lies on the cavity spectrum. We see that even though there is a loss of efficiency, the change is gradual and there is only a 50% reduction over a cavity linewidth. Also, we would expect that if we added another detuning δ_2, efficiency would decrease. However, this does not happen. From Figure 43 we see that the effect of δ_2 is to shift the efficiency curves by the detuning δ_2 without altering the shape. So, the protocol can be used to obtain high efficiencies over a wide range of dipole detunings.

8.4 Weak Excitation Limit

In the protocol we describe, dipole detuning is compensated by fixing $|\alpha\rangle$, and adjusting the amplitude and phase of the other input coherent field $|\beta\rangle$ until the matching condition $\alpha r_1^g = \beta r_2^g$ is satisfied. The more detuning we have, the larger the amplitude required by the coherent field in order to achieve the desired efficiency. It is possible that at some point, the amplitudes required by the coherent fields will be so large that the g-e transition of the QDs will be saturated leading to a giant optical nonlinearity and enlargement of g-e transition. Because of this, the cavity reflection and transmission equations will depend on the pump power and Eqs 8.3 and 8.4 need to be modified accordingly. However, our protocol is intended to work in the linear regime wherein the QDs are unsaturated. This is possible only if the amplitude of the input fields is within a certain limit called the weak excitation limit. The weak excitation limit is defined as $\langle \sigma_z(t) \rangle \approx -1$, and is necessary for Eq. 8.3 to be valid. In order to see how large of detuning the protocol can withstand before the weak excitation limit is exceeded, we start with the Heisenberg equations of motion for the cavity field operator $\hat{\mathbf{f}}_1$ and the dipole lowering operator $\hat{\boldsymbol{\sigma}}_{\mathbf{1}-}$ given in Eq 8.1. We will consider cavity-dipole system 1. Similar equations are also applicable for cavity-dipole system 2. Eliminating $\hat{\mathbf{b}}$ from Eq 8.1, we have

$$[\frac{\kappa}{2}(i\delta_1 + \gamma) - g^2]\hat{\boldsymbol{\sigma}}_- = -ig\sqrt{\kappa}\hat{\mathbf{a}}_{in}^{\dagger} \tag{8.15}$$

Using the fact the cooperativity index C is $g^2/\gamma\kappa > 1$, the equation can be further simplified and multiplied with its conjugate to obtain

$$\langle \sigma_+ \sigma_- \rangle = \frac{g^2 \kappa}{(g^4 + \delta_1^2 \kappa^2 / 4)} \langle \hat{a}_{in}^{\dagger} \hat{a}_{in} \rangle \tag{8.16}$$

The parameter $\langle \sigma_+ \sigma_- \rangle$ represents the probability of the QD being in the excited state. In the weak excitation limit, $\langle \sigma_+ \sigma_- \rangle < 1$. We also identify $\langle \hat{a}_{in}^{\dagger} \hat{a}_{in} \rangle$ as the total flux of photons in the input field $|\alpha\rangle$. Using this in Eq 8.16, the weak excitation limit thus puts a limit on $|\alpha|^2$ given by

$$\frac{|\alpha|^2}{\tau_p} < \frac{g^2}{\kappa} + \frac{\kappa \delta_1^2}{g^2} \tag{8.17}$$

where τ_p is the pulse width of the laser. From Eq 8.17, we see that when there is no detuning δ_1, the flux of photons in the input field $|\alpha\rangle$ should be less than the modified lifetime of the QD within the cavity $\frac{g^2}{\kappa}$. This is understandable because, if the first photon excites the QD and the second photon comes in before the QD has decayed, we will no longer be in the weak excitation limit. However, if the QD is off resonant from the cavity with detuning δ_1, not all the light that comes in couples to the QD. Therefore, we will be able to pump the QDs with much more power before we exceed the weak excitation limit. This is given by the detuning dependent term $\frac{\kappa \delta_1^2}{g^2}$ in Eq 8.17.

Eq 8.17 conveys more than the weak excitation limit of $|\alpha\rangle$. We already saw that the matching condition $\alpha r_1^g = \beta r_2^g$ ensures that we get the maximum fidelity out of the system. If we use this condition in Eq 8.17, we obtain a limit on the flux of photons in the input field $\left|\beta\right\rangle$ given by

$$\frac{|\beta|^2}{\tau_p} < \frac{g^2}{\kappa} + \frac{\kappa\delta_2^2}{g^2} \tag{8.18}$$

We recognize this as the weak excitation limit equation for the field $\left|\beta\right\rangle$ which we would have obtained had we used the Heisenberg's equations of motion for cavity-dipole system 2. This implies that if we pick an $\left|\alpha\right\rangle$ such that it satisfies the weak excitation limit of cavity-dipole system 1, the matching condition automatically ensures that the flux of photons in $\left|\beta\right\rangle$ is within the weak excitation limit of cavity-dipole 2.

The upper bound on the photon flux of the input fields $\left|\alpha\right\rangle$ and $\left|\beta\right\rangle$ due to the weak excitation limit also indirectly limits the rate at which photons can be reflected from the cavities. The rate at which photons are reflected from cavity 1 is $|\alpha r_1^g|^2/\tau_p$. Using the upper limit on $|\alpha|^2/\tau_p$ from Eq 8.17 and cavity reflectivity r_1^g from Eq 8.3, we get

$$\frac{|\alpha r_1^g|^2}{\tau_p} < \frac{g^2}{\kappa} \tag{8.19}$$

The above equation implies that if QD1 is within the weak excitation limit, then the rate at which photons are scattered from cavity 1 cannot exceed g^2/κ. We recognize that the rate of reflected photons is also the rate at which photons impinge on detector $\hat{\mathbf{d}}_2$. This in turn defines the rate of entanglement between the two QDs. Thus, the upper bound on the rate of reflected photons from the cavities limits the rate of entanglement and this limit is given by g^2 / κ.

The analysis of higher order photon numbers in the previous section showed that the number of input photons in $|\alpha\rangle$ and $|\beta\rangle$ should be small in order to have a high fidelity entangled state between the QDs. The analysis of weak excitation limit in this section puts an upper bound on the rate of the input photons in $|\alpha\rangle$ and $|\beta\rangle$. Thus, the two analyses are fundamentally different in that one limits the total number of input photons and the other limits the rate of incoming photons. If we restrict the total number of input photons to a certain limit, the condition for weak excitation limit can be satisfied by determining the pulse width of the input fields. The weak excitation limit can always be satisfied by choosing a large pulse width for the input fields in order to limit the rate of the incoming photons. Hence, the limiting condition on the protocol is the contribution of the higher order photons numbers and not the saturation effects of the QD.

8.5 Effects of Cavity detuning

In the previous section, we considered the idealized case where both the cavities had identical resonant frequencies. However in realistic systems, this will not be the case. Fabrication imperfections may lead to slightly different resonances for the two cavities. Clearly, if even a small amount of mismatch between the cavities were to result in no entanglement, the usefulness of our protocol would be questionable. Thus, it is important to consider how sensitive the protocol is to cavity resonance mismatch.

Now let's consider the case where the two cavities do not have the same resonant frequency. The analysis of the protocol in the presence of cavity detuning becomes involved for two reasons. First, it is no longer clear which frequency we should use for the coherent fields $|\alpha\rangle$ and $|\beta\rangle$. We do not know whether to place it on resonance with one of the cavities or somewhere in between. This can depend on both the cavity separation $\Delta\omega_s$ and dipole detunings δ_1 and δ_2. Second, the matching condition used in the previous section $\alpha r_1^g = \beta r_2^g$, is not guaranteed to be optimal. If a detection event is observed in detector $\hat{\mathbf{d}}_2$, then the state of the two QDs is

$$\begin{aligned}\left|\Psi_f\right\rangle_{dipoles} = \frac{1}{N}[(\alpha r_1^g - \beta r_2^g)\left|gg\right\rangle + (\alpha r_1^m - \beta r_2^m)\left|mm\right\rangle \\ + \alpha r_1^m\left|mg\right\rangle - \beta r_2^m\left|gm\right\rangle]\end{aligned} \tag{8.20}$$

where $N^2 = |\alpha r_1^m - \beta r_2^m|^2 + |\alpha r_1^m|^2 + |\beta r_2^m|^2$. The matching condition $\alpha r_1^g = \beta r_2^g$ ensures that we do not have any detection at $\hat{\mathbf{d}}_2$ if both the dipoles are in the state $|g\rangle$. However, the field amplitude at $\hat{\mathbf{d}}_2$ if both the dipoles are in the state $|m\rangle$ i.e. $(\alpha r_1^m - \beta r_2^m)$ is not compensated. This results in imperfect destructive interference at detector $\hat{\mathbf{d}}_2$. Thus, there is a small probability of detection at $\hat{\mathbf{d}}_2$ when both the dipoles are in state $|m\rangle$. This causes a loss of fidelity.

In order to obtain the state that comes closest to the desired final entangled state, we must optimize the fidelity with respect to ω, α and β. Figure 44 plots the dependence of fidelity on the laser frequency for several different values of δ_1. The cavity separation $\Delta\omega_s = \omega_2 - \omega_1$ is set to 50 GHz, and $\delta_2 = \Delta\omega_s / 2$ (halfway between the frequencies of the two cavities). The figure is optimized over the real and imaginary parts of $\frac{\alpha}{\beta}$. The value of the maximum fidelity for the three curves occurs at three different frequencies. The frequency at which we get maximum fidelity is the optimal frequency ω. The fidelity at that frequency is the maximum fidelity that can be obtained for that particular configuration of $\Delta\omega_s$, δ_1 and δ_2.

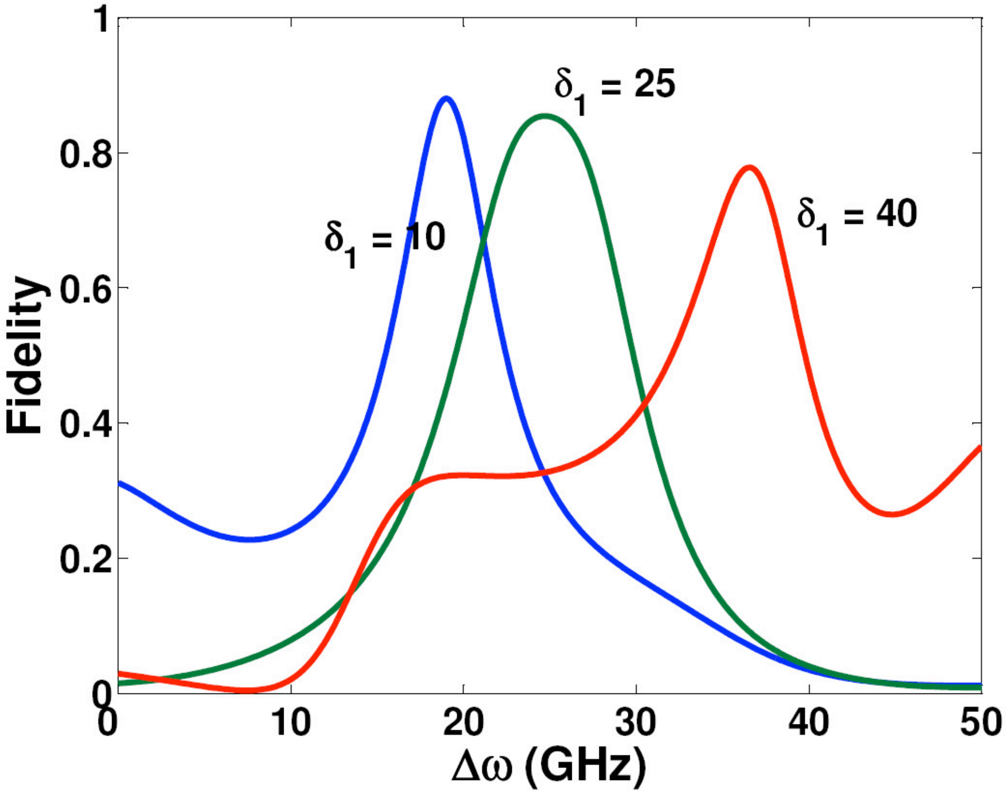

Figure 44 : Fidelity as a function of laser frequency for different values of Δ_1. Optimization is performed over the real and imaginary parts of α/β. Cavity separation is set to 50 GHz and $\Delta_2 = 0.25\kappa$ GHz

For calculating the effects of cavity detuning, the frequency midway between the two cavity frequencies is set as the reference frequency. Based on this reference frequency, $\omega_1 = -\Delta\omega_s / 2$ and $\omega_2 = \Delta\omega_s / 2$. Also, it will be easier if we define the dipole detunings in terms of the reference frequency rather than the cavity frequencies. We define $\Delta_1 = \delta_1 + \omega_1$ and $\Delta_2 = \delta_2 + \omega_2$, which are the dipole detunings of QD 1 and 2 with respect to the reference frequency located midway between the two cavities. These definitions ensure that when increasing the cavity separation $\Delta\omega_s$ we do not affect the QDs. In Figure 45, we plot optimized fidelity as a function of cavity detuning $\Delta\omega_s$ for different values of Δ_1 with $\Delta_2 = 0$. When $\Delta\omega_s = 0$, which represents the case when there is no cavity detuning, fidelity is 1. We have already considered the case when there is no cavity detuning and the input fields are considered to be weak. So, it is not surprising that we get a perfectly entangled state when $\Delta\omega_s = 0$. As the two cavities move apart, the spectrums of the two cavities no longer overlap. Thus, there is a small probability of photon detection at $\hat{\mathbf{d}}_2$ when the dipoles are in the state $|mm\rangle$. This results in a loss of fidelity. Surprisingly, however, the fidelity does not continue to decrease, but instead increases back to 1 at some value of $\Delta\omega_s$. As we keep increasing $\Delta\omega_s$ further, for a certain value of the laser frequency ω, both r_1^g and r_2^g are 0. If a detection event is observed in detector $\hat{\mathbf{d}}_2$, then the state of the two QDs collapses to

$$\left|\Psi_f\right\rangle_{dipoles} = \frac{1}{N}[(\alpha r_1^m - \beta r_2^m)|mm\rangle + \alpha r_1^m |mg\rangle - \beta r_2^m |gm\rangle] \tag{8.21}$$

where $N^2 = |\alpha r_1^m - \beta r_2^m|^2 + |\alpha r_1^m|^2 + |\beta r_2^m|^2$. So, instead of using the matching condition $\alpha r_1^g = \beta r_2^g$, we need to use the matching condition $\alpha r_1^m = \beta r_2^m$. Thus, the state of the QDs is projected onto $\left|\Psi_{-}\right\rangle = \left(\left|gm\right\rangle - \left|mg\right\rangle\right)/\sqrt{2}$. We have an ideal entangled state and fidelity of 1.

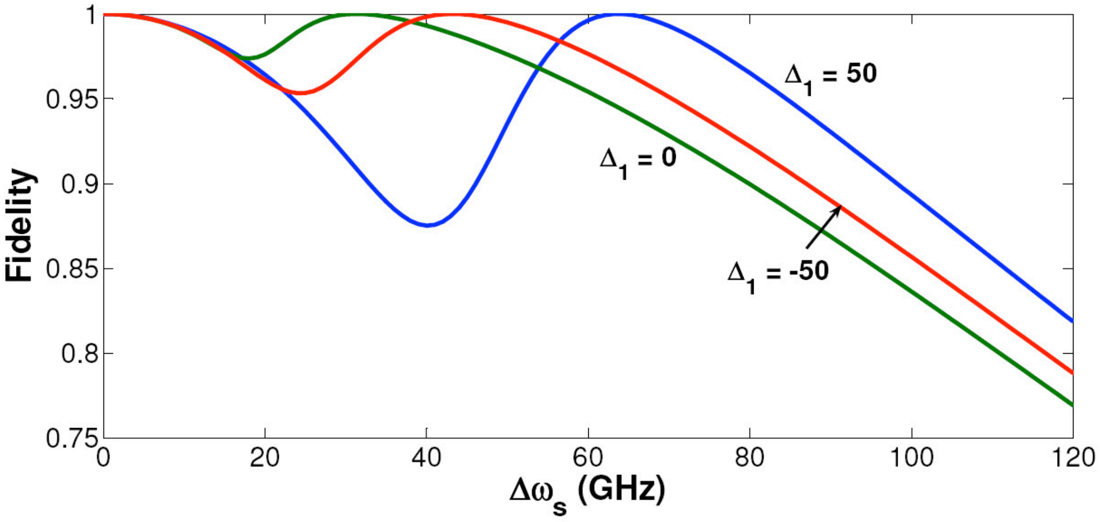

Figure 45 : Optimized fidelity as a function of $\Delta\omega_s$ for different values of Δ_1. $\Delta_2 = 0$

In Figure 46, we plot optimized fidelity as a function of cavity detuning $\Delta\omega_s$, and dipole detuning Δ_1. Maximum fidelity of 1 is obtained when $\Delta\omega_s = 0$, which represents the case when the two cavities have the same resonant frequency. When $\Delta\omega_s < 50$GHz, the variation in optimized fidelity with Δ_1 is very less. This is very important because it not very difficult to engineer two cavities to have similar resonant frequencies, but it is very difficult to find QDs with similar emission frequencies. So, most often we will be working in the regime where $\Delta\omega_s$ is close to 0. Thus in this regime, optimized fidelity not only gives the best fidelity that can be obtained but is also independent of dipole detuning Δ_1. As we increase $\Delta\omega_s$, the dependence of fidelity on δ_1 also increases. Thus, we are no longer in the regime where fidelity is independent of dipole detunings. This can also be seen from the peak fidelity, which occurs at different values of Δ_1 for different values of $\Delta\omega_s$. From Figure 46, fidelity is over 0.75 for a cavity linewidth separation (100 GHz) of the cavities even over a wide range of dipole detunings. Thus, we can use the protocol to obtain high fidelities even if the cavities and dipoles are detuned.

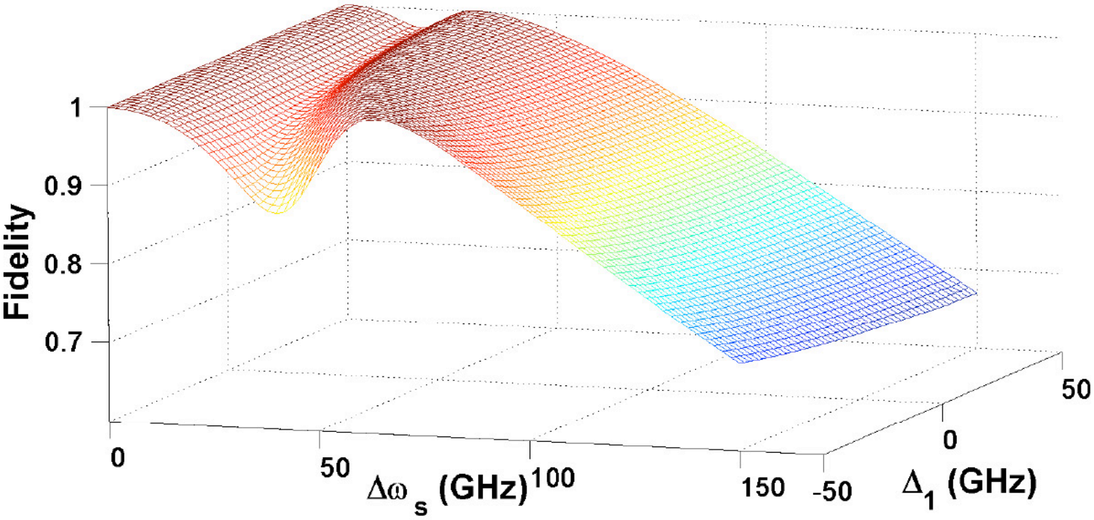

Figure 46 : Fidelity as a function of cavity separation $\Delta\omega_s$ and dipole detuning Δ_1

8.6 Exciton-Biexciton Model

The protocol to generate entanglement between two QDs relies on considering the QD as a three level system. One of the ways to consider the QD as a three level system is by making use of the excitonic and biexcitonic transitions. The QD consists of three states: the ground state, an exciton state X consisting of a single electron-hole pair within the QD and a biexciton state XX which is formed when two electron-hole pairs are trapped inside the QD. The recombination of an electron-hole pair in the XX state generates the biexciton XX photon. Similarly, the recombination of an electron-hole pair in X state generates the X photon. The X and XX photons have different energies due to the difference in coulomb energies between the initial and final states. The typical wavelength separation between the two lines is 1nm which corresponds to a 400 GHz separation in frequency. Thus, we can make use of this difference in frequencies to spectrally isolate the two lines. The schematic of the QD as a three level system is shown in Figure 47. We identify the three states of the QD as the ground, X and XX states. However, we still do not know which of these states corresponds to $|g\rangle, |e\rangle$ and $|m\rangle$ states described initially in the protocol. In order to match the actual three level system of the QD with the three level system used in the protocol, let us consider the biexciton XX transition to be the g-e transition. Thus, the X and XX states correspond to the $|g\rangle$ and $|e\rangle$ states. Since, the X and XX states are the $|g\rangle$ and $|e\rangle$ states, the actual ground state of the QD is taken to be the metastable state $|m\rangle$ described in the protocol. Thus the ground, X and XX states of the QD correspond to the $|m\rangle, |g\rangle$ and $|e\rangle$ states respectively.

We assume the biexciton transition to be on resonance with the cavity frequency. This is indicated in Figure 47 where the XX transition is in the middle of the cavity spectrum. The modified spontaneous emission rate of XX photon in the cavity is given by g^2 / κ. This XX photon lifetime determines the minimum pulse duration for the input coherent fields. The pulse duration τ_p of the input coherent fields $|\alpha\rangle$ and $|\beta\rangle$ should be more than the lifetime of the XX transition to be able to see dipole induced transparency. The XX photon emission rate also determines the maximum rate at which entanglement can occur. Thus, the maximum rate at which entanglement can occur is given by $\gamma_{XX} = g^2 / \kappa$.

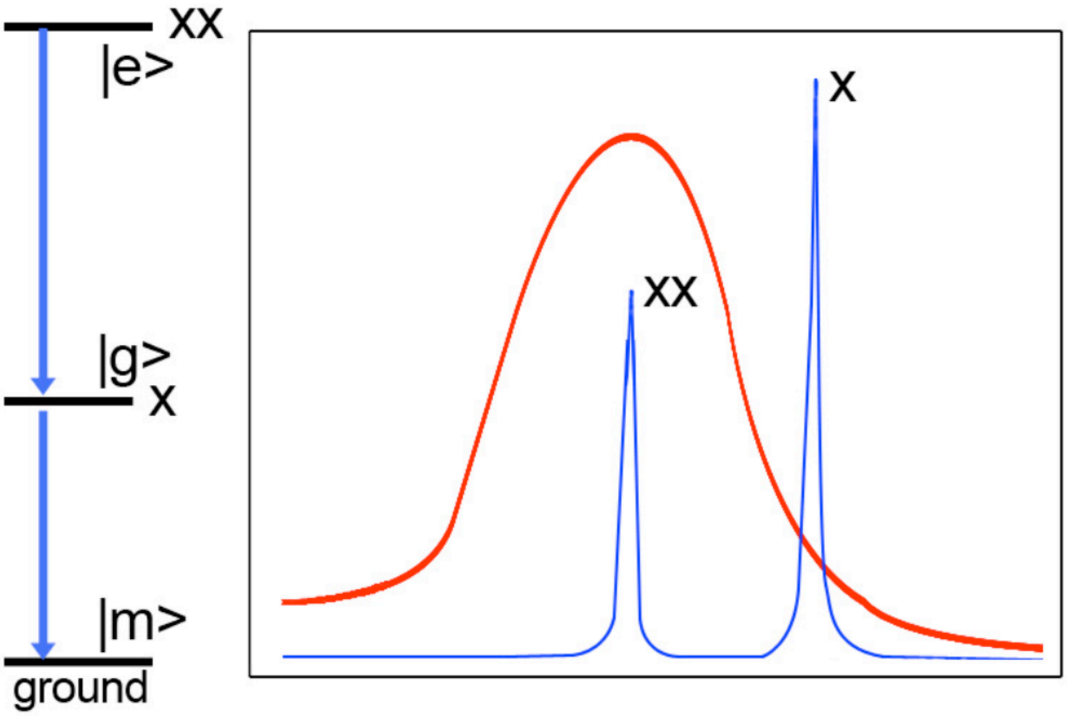

Figure 47 : QD as a three level system

For the three level structure that we have considered, there is no m-e transition. However, there is a g-X transition which decoheres the system. The coherence time of this transition determines the coherence time of the experiment. The lifetime of this transition is due to both radiative decay and dephasing. The radiative decay rate of g-X transition can be obtained by solving the equation of motion for the dipole lowering operator $\hat{\boldsymbol{\sigma}}_{\mathbf{1}-}$ given in time domain. Thus, the cavity-coupled radiative decay rate of the QD is given by $g^2\kappa / (\delta^2 + \kappa^2) + \gamma$. We see that the detuning of the exciton line δ from the cavity results in an decrease in transition rate between the $\left|g\right\rangle$ and $\left|m\right\rangle$

states. The dephasing of the QDs which occurs at rate of $1/T_2$, where T_2 is the dephasing time, further adds to the rate of decoherence of the g-X transition. Thus, the total decoherence rate of the exciton is given by

$$\gamma_x = \frac{g^2\kappa}{\delta^2 + \kappa^2} + \gamma + \frac{1}{T_2} \tag{8.22}$$

In order to determine the validity of the metastable state as a shelving state, we define the ratio of the biexciton modified lifetime to the exciton coherence (γ_{xx}/γ_x) as an important figure of merit N_{ent}.

$$N_{ent} = \frac{\gamma_{xx}}{\gamma_x} \tag{8.23}$$

Since, γ_{xx} determines the entanglement rate and γ_x determines the decoherence rate, this ratio determines the maximum number of entanglements that can be performed before the system decoheres. It is obvious that if N_{ent} is less than one, the system decoheres before any entanglement is completed. So, we need to achieve large N_{ent} to perform a greater number of entanglement operations. For calculations, we choose values experimentally observed for g as 20 GHz and κ of 25 GHz which corresponds to a Q of 13300. For values of T_2 we use 2 ns, which are appropriate values for InAs QDs. For these values, γ_{xx} is 16 GHz , γ_x is 0.69 GHz and N_{ent} is 23. Thus, theoretically the maximum number of entanglement operations that can be performed is 23. N_{ent} can be made larger by increasing γ_{xx} by fabricating high Q cavities with smaller κ and larger g. N_{ent} can also be made larger by decreasing γ_x. However, γ_x cannot be decreased beyond a certain point as it will be limited by dephasing rate.

For a cavity linewidth of 25 GHz, the exciton line lies outside the cavity spectrum ($\delta = 400$ GHz). However, the exciton line still couples to the cavity and we cannot ignore the presence of an extra transition coupled to the cavity. In the best case, it couples to the cavity with the coupling strength equal to the vacuum Rabi frequency. So, we cannot substitute for g as 0 in Eq 8.3 and Eq 8.4 in order to obtain transmission and reflection coefficients when the QD is in state $\left|m\right\rangle$. We need to use the vacuum Rabi frequency as the value for g in Eqs 8.3 and 8.4 to obtain the values of r_1^m and t_1^m. The changes in the coefficients will modify the final state of the QDs and hence the fidelity of the system. In Figure 48 we plot the dependence of fidelity on dipole detunings δ_1 and δ_2 for the above case. For both $\delta_1 = 0$ and $\delta_2 = 0$, fidelity is 1 as expected. When we increase δ_1 and δ_2, the transmission and reflection coefficients are modified due to the coupling of the X transition to the cavity. This lowers the fidelity of the output state. The drop is fidelity is gradual and for a cavity linewidth separation of the dipoles from the cavity resonance (25 GHz), fidelity drops to only 0.98. As we further increase the detunings to 100 GHz, fidelity drops to 0.85. Thus, the protocol can be used to create entanglement between QDs even if the exciton line couples to the cavity.

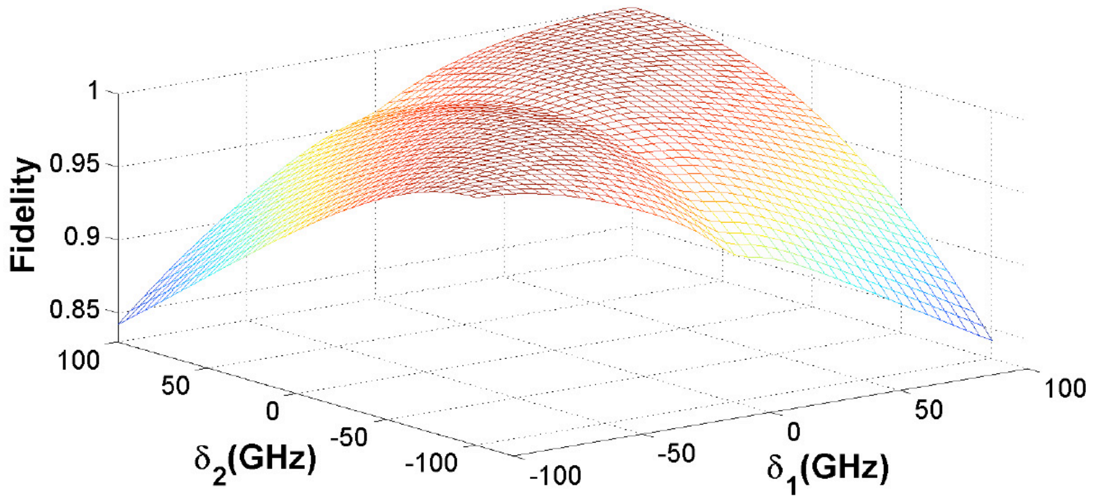

Figure 48 : Fidelity as a function of dipole detunings δ_1 and δ_2 for exciton-biexciton of a QD

8.7 Fidelity of entanglement measurement

The input coherent fields are $|\alpha\rangle$ and $|\beta\rangle$. Both the dipoles are initialized in a superposition of states $|g\rangle$ and $|m\rangle$. Thus, the initial state of the system is

$$|\Psi_i\rangle = |\alpha\rangle|\beta\rangle(|g\rangle + |m\rangle)(|g\rangle + |m\rangle)/2 \tag{8.24}$$

The coherent states can be replaced by their corresponding displacement operators to account for all order of photon numbers. Thus,

$$|\Psi_i\rangle = \frac{1}{2} e^{(\alpha \hat{a}_{in}^{\dagger} - \alpha^* \hat{a}_{in})} |0\rangle_{a_{in}} \; e^{(\beta \hat{c}_{in}^{\dagger} - \beta^* \hat{c}_{in})} |0\rangle_{c_{in}} \left(|gg\rangle + |gm\rangle + |mg\rangle + |mm\rangle\right) \tag{8.25}$$

The input fields after interactions with the cavity-dipole systems are transformed. Thus, when the dipoles are in state $|gg\rangle$,

$$\begin{aligned} \hat{a}^{\dagger}_{in} &\to r_1^g \hat{a}^{\dagger}_{out} + t_1^g \hat{b}^{\dagger}_{out} \\ \hat{c}^{\dagger}_{in} &\to r_2^g \hat{c}^{\dagger}_{out} + t_2^g \hat{d}^{\dagger}_{out} \end{aligned} \tag{8.26}$$

Similar transformation equations apply when the dipoles are in the states $|gm\rangle$, $|mg\rangle$ and $|mm\rangle$. The reflected field from the two cavities is mixed on a 50/50 beamsplitter that applies the transformation:

$$\begin{aligned} \hat{a}^{\dagger}_{out} &\to (\hat{d}_1 + \hat{d}_2)/\sqrt{2} \\ \hat{c}^{\dagger}_{out} &\to (\hat{d}_1 - \hat{d}_2)/\sqrt{2} \end{aligned} \tag{8.27}$$

Applying the cavity and beamsplitter transformations on the initial state $|\Psi_i\rangle$ we get

$$|\Psi_{gg}\rangle = D(\frac{\alpha r_1^g + \beta r_2^g}{\sqrt{2}}) D(\frac{\alpha r_1^g - \beta r_2^g}{\sqrt{2}}) D(\alpha t_1^g) D(\beta t_2^g) |0\rangle_{d_1, d_2, b_{out}, d_{out}} |gg\rangle \tag{8.28}$$

where $|\Psi_{gg}\rangle$ is the state of the output modes for the dipoles in state $|gg\rangle$. This state can be split up into the modes of detector $\hat{d}_1$, $\hat{b}_{out}$ and $\hat{d}_{out}$ and detector $\hat{d}_2$. Thus,

$$\begin{aligned} |\Psi_{gg}\rangle &= |\psi_{gg}\rangle |\mu_{gg}\rangle |gg\rangle \\ |\psi_{gg}\rangle &= D(\frac{\alpha r_1^g + \beta r_2^g}{\sqrt{2}}) D(\alpha t_1^g) D(\beta t_2^g) |0\rangle_{d_1, b_{out}, d_{out}} \\ |\mu_{gg}\rangle &= D(\frac{\alpha r_1^g - \beta r_2^g}{\sqrt{2}}) |0\rangle_{d_2} \end{aligned} \tag{8.29}$$

$|\psi_{gg}\rangle$ is the state of the output modes at detector $\hat{d}_1$ and the transmitted modes $\hat{b}_{out}$ and $\hat{d}_{out}$ when the dipoles are in state $|gg\rangle$. $|\mu_{gg}\rangle$ is the field amplitude at detector $\hat{d}_2$

when the dipoles are in state $\left|gg\right\rangle$. Similarly, we can obtain the field amplitudes

$\left|\Psi_{gm}\right\rangle$, $\left|\Psi_{mg}\right\rangle$ and $\left|\Psi_{mm}\right\rangle$

when the dipoles are in states $\left|gm\right\rangle$, $\left|mg\right\rangle$ and $\left|mm\right\rangle$. The final state of the system is given by

$$\left|\Psi_f\right\rangle = \left|\Psi_{gg}\right\rangle + \left|\Psi_{gm}\right\rangle + \left|\Psi_{mg}\right\rangle + \left|\Psi_{mm}\right\rangle \tag{8.30}$$

These states $\left|\Psi_{gm}\right\rangle$, $\left|\Psi_{mg}\right\rangle$ and $\left|\Psi_{mm}\right\rangle$ can be further decomposed on similar lines to Eq \ref{dipstate} to obtain the field amplitudes $\left|\psi_{gm}\right\rangle$ and $\left|\mu_{gm}\right\rangle$,$\left|\psi_{mg}\right\rangle$ and $\left|\mu_{mg}\right\rangle$ and $\left|\psi_{mm}\right\rangle$ and $\left|\mu_{mm}\right\rangle$ respectively.

We define the projection matrix M as $M = \sum_{n=1}^{\infty} \left|n\right\rangle_{d_2} \left\langle n\right|$. M can also be written as

$$\begin{aligned} M &= \sum_{n=0}^{\infty} \left|n\right\rangle_{d_2} \left\langle n\right| - \left|0\right\rangle_{d_2} \left\langle 0\right| \\ &= I - \left|0\right\rangle_{d_2} \left\langle 0\right| \end{aligned} \tag{8.31}$$

In terms of *M,* the density matrix of the dipoles is given by

$$\rho_{dipoles} = \frac{tr_{(\text{fields})}\{\left\langle M \mid \Psi_f\right\rangle\left\langle \Psi_f \mid M\right\rangle\}}{tr_{(\text{dipoles \& fields})}\{\left\langle M \mid \Psi_f\right\rangle\left\langle \Psi_f \mid M\right\rangle\}} \tag{8.32}$$

The fidelity *F* of the system is then

$$F = \left\langle \Psi_- \middle| \rho_{dipoles} \middle| \Psi_- \right\rangle \tag{8.33}$$

$$F = \left\langle \Psi_- \right| \frac{tr_{(\text{fields})}\{\left\langle M \mid \Psi_f\right\rangle\left\langle \Psi_f \mid M\right\rangle\}}{tr_{(\text{dipoles \& fields})}\{\left\langle M \mid \Psi_f\right\rangle\left\langle \Psi_f \mid M\right\rangle\}} \left| \Psi_- \right\rangle \tag{8.34}$$

The denominator is the probability of getting a detection at detector $\hat{d}_2$. We identify this as efficiency η.

$$\begin{aligned} F &= \left\langle \Psi_- \middle| \rho_{dipoles} \middle| \Psi_- \right\rangle \\ &= \left\langle \Psi_- \right| \frac{tr_{(\text{fields})}\{ \left| \Psi_f \right\rangle \left\langle \Psi_f \right| - tr_{(\text{fields})}\{ \left\langle M \mid \Psi_f \right\rangle \left\langle \Psi_f \mid M \right\rangle \}}{\eta} \left| \Psi_- \right\rangle \\ &= \frac{F_1 - F_2}{\eta} \end{aligned} \tag{8.35}$$

The individual terms can be evaluated to give

$$F_1 = \frac{1}{4} - \frac{\left\langle \Psi_{gm} \middle| \Psi_{mg} \right\rangle}{2} - \frac{\left\langle \Psi_{mg} \middle| \Psi_{gm} \right\rangle}{2} \tag{8.36}$$

$$\begin{aligned} F_2 = \frac{1}{8} e^{-|\mu_{gm}|^2} + \frac{1}{8} e^{-|\mu_{mg}|^2} - \frac{1}{2} e^{-(|\mu_{gm}|^2 + |\mu_{mg}|^2)/2} \left\langle \psi_{mg} \middle| \psi_{gm} \right\rangle \\ - \frac{1}{2} e^{-(|\mu_{gm}|^2 + |\mu_{mg}|^2)/2} \left\langle \psi_{gm} \middle| \psi_{mg} \right\rangle \end{aligned} \tag{8.37}$$

$$\eta = \frac{1}{4} \left[e^{-\mu_{gg}^2} + e^{-\mu_{gm}^2} + e^{-\mu_{mg}^2} + e^{-\mu_{mm}^2} \right] \tag{8.38}$$

Thus, the complete expression for fidelity and efficiency can be obtained.

8.8 Conclusions

In conclusion, we have shown that one can achieve high fidelity entangled states between two dipoles, even when their emission frequencies are different. The method is robust to dipole and cavity frequency mismatch. Efficiency loss for a cavity linewidth change in dipole detuning is about 50% for a constant fidelity. Therefore, relatively high fidelity can be obtained over a large range of dipole detunings without significant loss of efficiency. The development of protocols that are robust to these imperfections is extremely important for semiconductor based implementations of quantum networks.

Chapter 9

Perspectives and Future directions

Over the last decade, exponential increase of information bandwidth over the internet and other communication media has increased the total power consumed by the devices associated with information exchange. The overall energy consumption of information processing and communications is estimated to be 3% of the fraction of US electrical power consumed. This figure is only expected to increase due to the increase in the number of users. On one hand, the CMOS industry is trying to pack a large number of devices onto a chip in keeping with the Moores law, which states that the number of transistors on a chip is expected to double every 16 months. However, the power consumption of the devices based on energy consumed per bit of operation has been decreasing very slowly and stands at fentojoule level for the CMOS industry. This figure is expected to decrease in the future, but very slowly.

In this scenario, optical technology is thought of as an ideal replacement for electronic switches. Switches based on optics have always had the potential to outperform their electronic counterparts. An optical transistor has the potential to perform switching at not only attojoule levels corresponding to single photon levels, but their switching speed can also be much higher. The current switching time for CMOS devices is in the ps range. This figure is due to the limit imposed by the power dissipation of the devices.

In this work, we have demonstrated optical switching of an incoming beam with a switching energy of 14 aJ which corresponds to 65 photons in the switching pulse. This figure is much lower than the benchmark set by the CMOS industry. This work presents one of the first approaches which have been able to break the benchmark set by the CMOS industry. The development of all optical switch capable of outperforming the electronic counterparts is a healthy addition in the battle between optics and electronics.

There is plenty of scope for improvement in the devices that we have demonstrated in this work. Firstly, the coupling rate between the cavity and waveguide was not optimized. On one hand, we want to achieve a high coupling between the cavity and waveguide so that most of the light propagating in the waveguide can couple to the cavity. However, if we increase the cavity-waveguide coupling rate, the *Q* of the cavity decreases and it becomes increasingly difficult to find any strongly coupled dots in the cavity. Thus, we need to strike a balance between the cavity-waveguide coupling rate and the decay rate of the cavity called the critical coupling point when light in the waveguide maximally couples to the cavity.

The switching speed of the device was shown to be 8.4 GHz. This figure can be improved by working with cavity-QD systems with higher g. Till about some time back strong coupling was difficult to achieve in GaAs systems due to the difficulties experienced in fabrication of photonic crystal cavities. The highest *Q*s that have been reported on GaAs material systems embedded with a quantum dot layer is 20000 [177]. This *Q* is much lower than *Q*s that have been reported in GaAs without QDs indicating that most of reduction in Q is due to material losses from the QDs. This presents an interesting tradeoff during fabrication. On one hand, we want to achieve high Q to realize strong g. This implies that we want to reduce the density of QDs on the sample. On the flip side, if we decrease the number of QDs on the sample, we decrease the probability of finding QDs which are strongly coupled to the cavities. We start off with a QD sample with a density of 3-10 QDs/μm^2. With this density of dots, we have been able to achieve Qs of 35000 on GaAs photonic crystal cavities. At the same time, we find from our measurements that roughly 10% of the cavities have a strongly coupled QD embedded in them. The coupling between the waveguide and grating coupler is also low in our experiments. However, recent studies have shown that efficient grating couplers can be designed which can have a coupling efficiency as high as 90%. With the design of such coupler and optimized cavity-QD system with high g's, such systems have the potential to outperform the results in this work.

These systems are also not without their drawbacks. In this work, we are working with cavity-QD which have been brought onto resonance by changing the temperature of the sample. In principle, we could have also worked with photochromic materials and obtained the same result. Now, if we want to extend the work to multiple cavities, either fabrication needs to be extremely good so that all the cavities have the same resonance or the QDs that we work with should have the same resonance. Both these conditions are difficult to achieve. Fabrication inconsistencies is one of the limiting factors for the development of multicavity systems. If the cavities all the have resonance, then the photochromic material can be used to shift the cavity resonances inspite of the differences in resonances of the quantum dots. The probabilistic growth of the QDs also restricts the practicality of such systems to an extent. Nevertheless, these systems based on GaAs photonic crystals embedded with InAs QDs serve as ideal candidates for studying optical phenomenon which can be adopted by other material systems in the future.

Bibliography

[1] D.A.B. Miller, “Are optical transistors the logical next step?,” *Nature Photonics*, vol. 4, 2010, p. 3–5.

[2] R. Takahashi, Y. Kawamura, and H. Iwamura, “Ultrafast 1.55 µm all-optical switching using low-temperature-grown multiple quantum wells,” *Applied Physics letters*, vol. 68, 1996, p. 153–155.

[3] A.V. Gopal, H. Yoshida, A. Neogi, N. Georgiev, and T. Mozume, “Intersubband absorption saturation in InGaAs-AlAsSb quantum wells,” *Quantum Electronics, IEEE Journal of*, vol. 38, 2002, p. 1515–1520.

[4] S. Nakamura, Y. Ueno, and K. Tajima, “Femtosecond switching with semiconductor-optical-amplifier-based symmetric Mach–Zehnder-type all-optical switch,” *Applied Physics Letters*, vol. 78, 2001, p. 3929.

[5] H.J.S. Dorren, X. Yang, A.K. Mishra, Z. Li, H. Ju, H. de Waardt, G.D. Khoe, T. Simoyama, H. Ishikawa, and H. Kawashima, others, “All-optical logic based on ultrafast gain and index dynamics in a semiconductor optical amplifier,” *Selected Topics in Quantum Electronics, IEEE Journal of*, vol. 10, 2004, p. 1079–1092.

[6] M.L. Nielsen, J. M\ork, R. Suzuki, J. Sakaguchi, and Y. Ueno, “Experimental and theoretical investigation of the impact of ultra-fast carrier dynamics on high-speed SOA-based all-optical switches,” *Optics Express*, vol. 14, 2006, p. 331–347.

[7] P.A. Andrekson, H. Sunnerud, S. Oda, T. Nishitani, and J. Yang, “Ultrafast, atto-Joule switch using fiber-opticparametric amplifier operated in saturation,” *Optics Express*, vol. 16, Jul. 2008, pp. 10956-10961.

[8] K. Hinton, G. Raskutti, P.M. Farrell, and R.S. Tucker, “Switching energy and device size limits on digital photonic signal processing technologies,” *Selected Topics in Quantum Electronics, IEEE Journal of*, vol. 14, 2008, p. 938–945.

[9] R. Bose, D. Sridharan, G.S. Solomon, and E. Waks, “Large optical Stark shifts in semiconductor quantum dots coupled to photonic crystal cavities,” *Applied Physics Letters*, vol. 98, 2011, p. 121109.

[10] E. Waks and J. Vuckovic, “Dispersive properties and large Kerr nonlinearities using dipole-induced transparency in a single-sided cavity,” *Physical Review A*, vol. 73, 2006, p. 041803.

[11] K. Srinivasan and O. Painter, “Linear and nonlinear optical spectroscopy of a strongly coupled microdisk–quantum dot system,” *Nature*, vol. 450, 2007, p. 862–865.

[12] I. Fushman, D. Englund, A. Faraon, N. Stoltz, P. Petroff, and J. Vučković, “Controlled phase shifts with a single quantum dot,” *Science*, vol. 320, 2008, p. 769.

[13] K. Nozaki, T. Tanabe, A. Shinya, S. Matsuo, T. Sato, H. Taniyama, and M. Notomi, “Sub-femtojoule all-optical switching using a photonic-crystal nanocavity,” *Nature Photonics*, vol. 4, 2010, p. 477–483.

[14] S. Matsuo, A. Shinya, T. Kakitsuka, K. Nozaki, T. Segawa, T. Sato, Y. Kawaguchi, and M. Notomi, "High-speed ultracompact buried heterostructure photonic-crystal laser with 13 fJ of energy consumed per bit transmitted," *Nature Photonics*, vol. 4, 2010, p. 648–654.

[15] J.D. Meindl, "Low power microelectronics: Retrospect and prospect," *Proceedings of the IEEE*, vol. 83, 1995, p. 619–635.

[16] G.W. Bryant and G. Solomon, *Optics of quantum dots and wires*, Artech House, 2005.

[17] J.-Y. Marzin, J.-M. Gérard, A. Izraël, D. Barrier, and G. Bastard, "Photoluminescence of Single InAs Quantum Dots Obtained by Self-Organized Growth on GaAs," *Physical Review Letters*, vol. 73, 1994, p. 716.

[18] J.M. Moison, F. Houzay, F. Barthe, L. Leprince, E. Andre, and O. Vatel, "Self-organized growth of regular nanometer-scale InAs dots on GaAs," *Applied Physics Letters*, vol. 64, Jan. 1994, pp. 196-198.

[19] J. Tersoff, C. Teichert, and M.G. Lagally, "Self-Organization in Growth of Quantum Dot Superlattices," *Physical Review Letters*, vol. 76, Mar. 1996, p. 1675.

[20] E. Yablonovitch, "Inhibited spontaneous emission in solid-state physics and electronics," *Physical Review Letters*, vol. 58, 1987, p. 2059–2062.

[21] H. Carmichael, *Statistical Methods in Quantum Optics: Non-classical fields*, Springer Verlag, 2007.

[22] T. Yoshie, A. Scherer, J. Hendrickson, G. Khitrova, H.M. Gibbs, G. Rupper, C. Ell, O.B. Shchekin, and D.G. Deppe, “Vacuum Rabi splitting with a single quantum dot in a photonic crystal nanocavity,” *Nature*, vol. 432, Nov. 2004, pp. 200-203.

[23] E.M. Purcell, H.C. Torrey, and R.V. Pound, “Resonance Absorption by Nuclear Magnetic Moments in a Solid,” *Physical Review*, vol. 69, Jan. 1946, p. 37.

[24] S.E. Harris, J.E. Field, and A. Imamogbrevelu, “Nonlinear optical processes using electromagnetically induced transparency,” *Physical Review Letters*, vol. 64, Mar. 1990, p. 1107.

[25] M.F. Yanik, S. Fan, and M. Soljačić, “High-contrast all-optical bistable switching in photonic crystal microcavities,” *Applied Physics Letters*, vol. 83, 2003, p. 2739.

[26] M. Notomi, A. Shinya, S. Mitsugi, G. Kira, E. Kuramochi, and T. Tanabe, “Optical bistable switching action of Si high-Q photonic-crystal nanocavities,” *Optics Express*, vol. 13, 2005, p. 2678–2687.

[27] T. Tanabe, M. Notomi, S. Mitsugi, A. Shinya, and E. Kuramochi, “All-optical switches on a silicon chip realized using photonic crystal nanocavities,” *Applied Physics Letters*, vol. 87, 2005, p. 151112–151112.

[28] Chad Husko, Alfredo De Rossi, , and , Sylvain Combrié, “Ultrafast all-optical modulation in GaAs photonic crystal cavities.” Applied Physics Letters vol 94, 2009, 021111

[29] K. Rivoire, Z. Lin, F. Hatami, W.T. Masselink, and J. Vuckovic, “Second harmonic generation in gallium phosphide photonic crystal nanocavities with ultralow continuous wave pump power,” *Optics Express*, vol. 17, Dec. 2009, pp. 22609-22615.

[30] I. Fushman, D. Englund, A. Faraon, N. Stoltz, P. Petroff, and J. Vučković, “Controlled Phase Shifts with a Single Quantum Dot,” *Science*, vol. 320, May. 2008, pp. 769 -772.

[31] D. Englund, A. Faraon, I. Fushman, N. Stoltz, P. Petroff, and J. Vuckovic, “Controlling cavity reflectivity with a single quantum dot,” *Nature*, vol. 450, Dec. 2007, pp. 857-861.

[32] D. Englund, A. Majumdar, A. Faraon, M. Toishi, N. Stoltz, P. Petroff, and J. Vučković, “Resonant excitation of a quantum dot strongly coupled to a photonic crystal nanocavity,” *Physical Review Letters*, vol. 104, 2010, p. 73904.

[33] S. Ates, S.M. Ulrich, A. Ulhaq, S. Reitzenstein, A. Löffler, S. Höfling, A. Forchel, and P. Michler, “Non-resonant dot–cavity coupling and its potential for resonant single-quantum-dot spectroscopy,” *Nature Photonics*, vol. 3, 2009, p. 724–728.

[34] Y. Akahane, T. Asano, B.-S. Song, and S. Noda, “Fine-tuned high-Q photonic-crystal nanocavity,” *Optics Express*, vol. 13, Feb. 2005, pp. 1202-1214.

[35] A. Majumdar, A. Faraon, E.D. Kim, D. Englund, H. Kim, P. Petroff, and J. Vuccaronkovicacute, “Linewidth broadening of a quantum dot coupled to an off-resonant cavity,” *Physical Review B*, vol. 82, Jul. 2010, p. 045306.

[36] S. Ates, S.M. Ulrich, S. Reitzenstein, A. Löffler, A. Forchel, and P. Michler, “Post-Selected Indistinguishable Photons from the Resonance Fluorescence of a Single Quantum Dot in a Microcavity,” *Physical Review Letters*, vol. 103, Oct. 2009, p. 167402.

[37] M. Winger, T. Volz, G. Tarel, S. Portolan, A. Badolato, K.J. Hennessy, E.L. Hu, A. Beveratos, J. Finley, V. Savona, and A. Imamogbrevelu, “Explanation of Photon Correlations in the Far-Off-Resonance Optical Emission from a Quantum-Dot–Cavity System,” *Physical Review Letters*, vol. 103, Nov. 2009, p. 207403.

[38] U. Hohenester, “Cavity quantum electrodynamics with semiconductor quantum dots: Role of phonon-assisted cavity feeding,” *Physical Review B*, vol. 81, Apr. 2010, p. 155303.

[39] M. Yamaguchi, T. Asano, K. Kojima, and S. Noda, “Quantum electrodynamics of a nanocavity coupled with exciton complexes in a quantum dot,” *Physical Review B*, vol. 80, Oct. 2009, p. 155326.

[40] M. Yamaguchi, T. Asano, and S. Noda, “Photon emission by nanocavity-enhancedquantum anti-Zeno effect in solid-state cavityquantum-electrodynamics,” *Optics Express*, vol. 16, Oct. 2008, pp. 18067-18081.

[41] M. Kaniber, A. Laucht, A. Neumann, J.M. Villas-Bôas, M. Bichler, M.-C. Amann, and J.J. Finley, “Investigation of the nonresonant dot-cavity coupling in two-dimensional photonic crystal nanocavities,” *Physical Review B*, vol. 77, Apr. 2008, p. 161303.

[42] P. Borri, W. Langbein, S. Schneider, U. Woggon, R.L. Sellin, D. Ouyang, and D. Bimberg, “Ultralong Dephasing Time in InGaAs Quantum Dots,” *Physical Review Letters*, vol. 87, 2001, p. 157401.

[43] P. Borri, W. Langbein, S. Schneider, U. Woggon, R.L. Sellin, D. Ouyang, and D. Bimberg, “Exciton relaxation and dephasing in quantum-dot amplifiers from room to cryogenic temperature,” *Selected Topics in Quantum Electronics, IEEE Journal of*, vol. 8, 2002, pp. 984-991.

[44] M. Toishi, D. Englund, A. Faraon, and J. Vu?kovi?, “High-brightness single photon source from a quantum dot in a directional-emission nanocavity,” *Optics Express*, vol. 17, 2009, pp. 14618-14626.

[45] A. Faraon, I. Fushman, D. Englund, N. Stoltz, P. Petroff, and J. Vuckovic, “Dipole induced transparency inwaveguide coupled photonic crystalcavities,” *Optics Express*, vol. 16, 2008, pp. 12154-12162.

[46] Y. Akahane, T. Asano, B.-S. Song, and S. Noda, “High-Q photonic nanocavity in a two-dimensional photonic crystal,” *Nature*, vol. 425, Oct. 2003, pp. 944-947.

[47] B.-S. Song, S. Noda, T. Asano, and Y. Akahane, “Ultra-high-Q photonic double-heterostructure nanocavity,” *Nature Materials*, vol. 4, Mar. 2005, pp. 207-210.

[48] M. Notomi, T. Tanabe, A. Shinya, E. Kuramochi, H. Taniyama, S. Mitsugi, and M. Morita, “Nonlinear and adiabatic control of high-Qphotonic crystal nanocavities,” *Optics Express*, vol. 15, Dec. 2007, pp. 17458-17481.

[49] T. Yamamoto, M. Notomi, H. Taniyama, E. Kuramochi, Y. Yoshikawa, Y. Torii, and T. Kuga, “Design of a high-Q air-slot cavity based on a width-modulated line-defect in a photonic crystal slab,” *Optics Express*, vol. 16, 2008, pp. 13809-13817.

[50] K. Hennessy, A. Badolato, M. Winger, D. Gerace, M. Atature, S. Gulde, S. Falt, E.L. Hu, and A. Imamoglu, “Quantum nature of a strongly coupled single quantum dot-cavity system,” *Nature*, vol. 445, Feb. 2007, pp. 896-899.

[51] Y. Ota, N. Kumagai, S. Ohkouchi, M. Shirane, M. Nomura, S. Ishida, S. Iwamoto, S. Yorozu, and Y. Arakawa, “Investigation of the Spectral Triplet in Strongly Coupled Quantum Dot–Nanocavity System,” *Applied Physics Express*, vol. 2, 2009, p. 122301.

[52] A. Badolato, M. Winger, K.J. Hennessy, E.L. Hu, and A. Imamoglu, “Cavity QED effects with single quantum dots,” *Comptes Rendus Physique*, vol. 9, Oct. 2008, pp. 850-856.

[53] A. Imamoglu, D.D. Awschalom, G. Burkard, D.P. DiVincenzo, D. Loss, M. Sherwin, and A. Small, “Quantum Information Processing Using Quantum Dot Spins and Cavity QED,” *Physical Review Letters*, vol. 83, Nov. 1999, p. 4204.

[54] M. Winger, A. Badolato, K.J. Hennessy, E.L. Hu, and A. Imamogbrevelu, “Quantum Dot Spectroscopy Using Cavity Quantum Electrodynamics,” *Physical Review Letters*, vol. 101, Nov. 2008, p. 226808.

[55] Y.A. Vlasov, M. O’Boyle, H.F. Hamann, and S.J. McNab, “Active control of slow light on a chip with photonic crystal waveguides,” *Nature*, vol. 438, Nov. 2005, pp. 65-69.

[56] E. Waks and J. Vuckovic, “Coupled mode theory for photonic crystal cavity-waveguide interaction,” *Optics Express*, vol. 13, Jun. 2005, pp. 5064-5073.

[57] E. Waks and J. Vuckovic, “Dipole induced transparency in drop-filter cavity-waveguide systems,” *Physical Review Letters*, vol. 96, 2006, p. 153601.

[58] D. Sridharan and E. Waks, “Generating entanglement between quantum dots with different resonant frequencies based on dipole-induced transparency,” *Physical Review A*, vol. 78, Nov. 2008, p. 052321.

[59] L.-M. Duan, M.D. Lukin, J.I. Cirac, and P. Zoller, “Long-distance quantum communication with atomic ensembles and linear optics,” *Nature*, vol. 414, Nov. 2001, pp. 413-418.

[60] L. Jiang, J.M. Taylor, K. Nemoto, W.J. Munro, R. Van Meter, and M.D. Lukin, “Quantum repeater with encoding,” *Physical Review A*, vol. 79, Mar. 2009, p. 032325.

[61] H.-J. Briegel, W. Dür, J.I. Cirac, and P. Zoller, “Quantum Repeaters: The Role of Imperfect Local Operations in Quantum Communication,” *Physical Review Letters*, vol. 81, Dec. 1998, p. 5932.

[62] L.-M. Duan and R. Raussendorf, “Efficient Quantum Computation with Probabilistic Quantum Gates,” *Physical Review Letters*, vol. 95, 2005, p. 080503.

[63] X. Yang, M. Yu, D.-L. Kwong, and C.W. Wong, “All-Optical Analog to Electromagnetically Induced Transparency in Multiple Coupled Photonic Crystal Cavities,” *Physical Review Letters*, vol. 102, Apr. 2009, p. 173902.

[64] A. Faraon, I. Fushman, D. Englund, N. Stoltz, P. Petroff, and J. Vuckovic, “Dipole induced transparency in waveguide coupled photonic crystal cavities,” *IEEE Lasers and Electro-Optics Society, 2008. LEOS 2008. 21st Annual Meeting of the*, 2008, p. 622–623.

[65] D.F. Walls and G.J. Milburn, *Quantum Optics*, Springer, 2008.

[66] S. Hughes and H. Kamada, “Single-quantum-dot strong coupling in a semiconductor photonic crystal nanocavity side coupled to a waveguide,” *Physical Review B*, vol. 70, Nov. 2004, p. 195313.

[67] J. Pan, S. Sandhu, Y. Huo, N. Stuhrmann, M.L. Povinelli, J.S. Harris, M.M. Fejer, and S. Fan, “Experimental demonstration of an all-optical analogue to the superradiance effect in an on-chip photonic crystal resonator system,” *Physical Review B*, vol. 81, Jan. 2010, p. 041101.

[68] J.-T. Shen and S. Fan, “Theory of single-photon transport in a single-mode waveguide. I. Coupling to a cavity containing a two-level atom,” *Physical Review A*, vol. 79, Feb. 2009, p. 023837.

[69] A.J. Hudson, R.M. Stevenson, A.J. Bennett, R.J. Young, C.A. Nicoll, P. Atkinson, K. Cooper, D.A. Ritchie, and A.J. Shields, “Coherence of an Entangled Exciton-Photon State,” *Physical Review Letters*, vol. 99, Dec. 2007, p. 266802.

[70] E. Waks and D. Sridharan, “Cavity QED treatment of interactions between a metal nanoparticle and a dipole emitter,” *Physical Review A*, vol. 82, 2010, p. 043845.

[71] A. Faraon, E. Waks, D. Englund, I. Fushman, and J. Vučković, “Efficient photonic crystal cavity-waveguide couplers,” *Applied Physics Letters*, vol. 90, 2007, p. 073102.

[72] T. Tanabe, M. Notomi, E. Kuramochi, A. Shinya, and H. Taniyama, "Trapping and delaying photons for one nanosecond in an ultrasmall high-Q photonic-crystal nanocavity," *Nature Photonics*, vol. 1, Jan. 2007, pp. 49-52.

[73] M. Notomi, E. Kuramochi, and T. Tanabe, "Large-scale arrays of ultrahigh-Q coupled nanocavities," *Nature Photonics*, vol. 2, Dec. 2008, pp. 741-747.

[74] M. Soljacic and J.D. Joannopoulos, "Enhancement of nonlinear effects using photonic crystals," *Nature materials*, vol. 3, 2004, p. 211–219.

[75] A.F. Dirk Englund, N.S. Ilya Fushman, and J.V. Pierre Petroff, "Controlling cavity reflectivity with a single quantum dot," *Nature*, vol. 450, 2007, p. 857–861.

[76] R. Bose, D. Sridharan, G.S. Solomon, and E. Waks, "Observation of strong coupling through transmission modification of a cavity-coupled photonic crystal waveguide," *Optics Express*, vol. 19, 2011, p. 5398–5409.

[77] A. Majumdar, A. Faraon, E.D. Kim, D. Englund, H. Kim, P. Petroff, and J. Vuccaronkovicacute, "Linewidth broadening of a quantum dot coupled to an off-resonant cavity," *Physical Review B*, vol. 82, Jul. 2010, p. 045306.

[78] T. Durhuus, B. Mikkelsen, C. Joergensen, S.L. Danielsen, and K.E. Stubkjaer, "All-optical wavelength conversion by semiconductor optical amplifiers," *Lightwave Technology, Journal of*, vol. 14, 1996, p. 942–954.

[79] K. Vlachos, N. Pleros, C. Bintjas, G. Theophilopoulos, and H. Avramopoulos, “Ultrafast time-domain technology and its application in all-optical signal processing,” *Lightwave Technology, Journal of*, vol. 21, 2003, p. 1857–1868.

[80] K.E. Stubkjaer, “Semiconductor optical amplifier-based all-optical gates for high-speed optical processing,” *Selected Topics in Quantum Electronics, IEEE Journal of*, vol. 6, 2000, p. 1428–1435.

[81] T. Houbavlis, K.E. Zoiros, M. Kalyvas, G. Theophilopoulos, C. Bintjas, K. Yiannopoulos, N. Pleros, K. Vlachos, H. Avramopoulos, L. Schares, L. Occhi, G. Guekos, J.R. Taylor, S. Hansmann, and W. Miller, “All-optical signal Processing and applications within the esprit project DO_ALL,” *Lightwave Technology, Journal of*, vol. 23, 2005, p. 781–801.

[82] M. Asobe, T. Kanamori, and K. Kubodera, “Ultrafast all-optical switching using highly nonlinear chalcogenide glass fiber,” *Photonics Technology Letters, IEEE*, vol. 4, 1992, p. 362–365.

[83] M. Asobe, T. Ohara, I. Yokohama, and T. Kaino, “Low power all-optical switching in a nonlinear optical loop mirror using chalcogenide glass fibre,” *Electronics Letters*, vol. 32, 1996, p. 1396–1397.

[84] G.S. Kanter, P. Kumar, K.R. Parameswaran, and M.M. Fejer, “Wavelength-selective pulsed all-optical switching based on cascaded second-order nonlinearity in a periodically poled lithium-niobate waveguide,” *Photonics Technology Letters, IEEE*, vol. 13, 2001, p. 341–343.

[85] Y.L. Lee, B.-A. Yu, T.J. Eom, W. Shin, C. Jung, Y.-C. Noh, J. Lee, D.-K. Ko, and K. Oh, "All-optical AND and NAND gates based on cascaded second-order nonlinear processes in a Ti-diffused periodically poled LiNbO3 waveguide," *Optics Express*, vol. 14, Apr. 2006, p. 2776–2782.

[86] M. Whitehead and G. Parry, "High-contrast reflection modulation at normal incidence in asymmetric multiple quantum well Fabry-Perot structure," *Electronics Letters*, vol. 25, 1989, p. 566–568.

[87] D. Massoubre, J.L. Oudar, J. Dion, J.C. Harmand, A. Shen, J. Landreau, and J. Decobert, "Scaling of the saturation energy in microcavity saturable absorber devices," *Applied Physics Letters*, vol. 88, 2006, p. 153513–153513.

[88] N. Hitoshi, Y. Sugimoto, K. Kanamoto, N. Ikeda, Y. Tanaka, Y. Nakamura, S. Ohkouchi, Y. Watanabe, K. Inoue, and H. Ishikawa, others, "Ultra-fast photonic crystal/quantum dot alloptical switch for future photonic networks," *Opt. Express*, vol. 12, 2004, p. 6606–6614.

[89] T. Tanabe, M. Notomi, S. Mitsugi, A. Shinya, and E. Kuramochi, "Fast bistable all-optical switch and memory on a silicon photonic crystal on-chip," *Optics Letters*, vol. 30, Oct. 2005, pp. 2575-2577.

[90] T. Tanabe, K. Nishiguchi, A. Shinya, E. Kuramochi, H. Inokawa, M. Notomi, K. Yamada, T. Tsuchizawa, T. Watanabe, and H. Fukuda, others, "Fast all-optical switching using ion-implanted silicon photonic crystal nanocavities," *Applied Physics Letters*, vol. 90, 2007, p. 031115.

[91] K. Asakawa, Y. Sugimoto, Y. Watanabe, N. Ozaki, A. Mizutani, Y. Takata, Y. Kitagawa, H. Ishikawa, N. Ikeda, and K. Awazu, others, “Photonic crystal and quantum dot technologies for all-optical switch and logic device,” *New Journal of Physics*, vol. 8, 2006, p. 208.

[92] Y. Sakakibara, A.G. Rozhin, H. Kataura, Y. Achiba, and M. Tokumoto, “Carbon nanotube-poly (vinylalcohol) nanocomposite film devices: Applications for femtosecond fiber laser mode lockers and optical amplifier noise suppressors,” *Japanese Journal of Applied Physics-Part 1 Regular Papers and Short Notes*, vol. 44, 2005, p. 1621–1625.

[93] S. Tatsuura, M. Furuki, Y. Sato, I. Iwasa, M. Tian, and H. Mitsu, “Semiconductor carbon nanotubes as ultrafast switching materials for optical telecommunications,” *Advanced Materials*, vol. 15, 2003, p. 534–537.

[94] C.Y. Jin, O. Kojima, T. Kita, O. Wada, M. Hopkinson, and K. Akahane, “Vertical-geometry all-optical switches based on InAs/GaAs quantum dots in a cavity,” *Applied Physics Letters*, vol. 95, 2009, p. 021109.

[95] T. Kitada, T. Mukai, T. Takahashi, K. Morita, and T. Isu, “Fast carrier relaxation of self-assembled InAs quantum dots embedded in strain-relaxed In0. 35Ga0. 65As barriers for ultrafast nonlinear optical switching applications,” *Journal of Crystal Growth*, vol. 311, 2009, p. 1807–1810.

[96] A. Muller, W. Fang, J. Lawall, and G.S. Solomon, "Emission spectrum of a dressed exciton-biexciton complex in a semiconductor quantum dot," *Physical Review Letters*, vol. 101, 2008, p. 27401.

[97] J. Vuckovic, D. Fattal, C. Santori, G.S. Solomon, and Y. Yamamoto, "Enhanced single-photon emission from a quantum dot in a micropost microcavity," *Applied Physics Letters*, vol. 82, May. 2003, p. 3596–3598.

[98] J. Vuckovic and Y. Yamamoto, "Photonic crystal microcavities for cavity quantum electrodynamics with a single quantum dot," *Applied Physics Letters*, vol. 82, Apr. 2003, p. 2374–2376.

[99] M. Born and E. Wolf, *Principles of Optics: Electromagnetic Theory of Propagation, Interference and Diffraction of Light*, Cambridge University Press, 1999.

[100] T.H. Stievater, X. Li, D.G. Steel, D. Gammon, D.S. Katzer, D. Park, C. Piermarocchi, and L.J. Sham, "Rabi Oscillations of Excitons in Single Quantum Dots," *Phys. Rev. Lett.*, vol. 87, Sep. 2001, p. 133603.

[101] X. Huang, A. Stintz, H. Li, L.F. Lester, J. Cheng, and K.J. Malloy, "Passive mode-locking in 1.3 μm two-section InAs quantum dot lasers," *Applied Physics Letters*, vol. 78, 2001, p. 2825.

[102] C. Cornet, C. Labbé, H. Folliot, P. Caroff, C. Levallois, O. Dehaese, J. Even, A. Le Corre, and S. Loualiche, "Time-resolved pump probe of 1.55 μm InAs/

InP quantum dots under high resonant excitation," *Applied Physics Letters*, vol. 88, 2006, p. 171502.

[103] W. Langbein, P. Borri, U. Woggon, V. Stavarache, D. Reuter, and A.D. Wieck, "Radiatively limited dephasing in InAs quantum dots," *Physical Review B*, vol. 70, Jul. 2004, p. 033301.

[104] A. Farjadpour, D. Roundy, A. Rodriguez, M. Ibanescu, P. Bermel, J.D. Joannopoulos, S.G. Johnson, and G. Burr, "Improving accuracy by subpixel smoothing in FDTD," *Optics Letters*, vol. 31, Oct. 2006, p. 2972–2974.

[105] R. Urata, L.Y. Nathawad, R. Takahashi, K. Ma, D.A.B. Miller, B.A. Wooley, and J.S. Harris, "Photonic A/D conversion using low-temperature-grown GaAs MSM switches integrated with Si-CMOS," *Journal of lightwave technology*, vol. 21, 2003, p. 3104.

[106] S. Suomalainen, A. Vainionp\ä\ä, O. Tengvall, T. Hakulinen, S. Karirinne, M. Guina, O.G. Okhotnikov, T.G. Euser, and W.L. Vos, "Long-wavelength fast semiconductor saturable absorber mirrors using metamorphic growth on GaAs substrates," *Applied Physics Letters*, vol. 87, 2005, p. 121106.

[107] L. Joulaud, J. Mangeney, J.M. Lourtioz, P. Crozat, and G. Patriarche, "Thermal stability of ion-irradiated InGaAs with (sub-) picosecond carrier lifetime," *Applied Physics Letters*, vol. 82, 2003, p. 856.

[108] F. Ganikhanov, G.R. Lin, W.C. Chen, C.S. Chang, and C.L. Pan, "Subpicosecond carrier lifetimes in arsenic-ion-implanted GaAs," *Applied Physics Letters*, vol. 67, 1995, p. 3465.

[109] T. Kitada, A. Mukaijo, T. Takahashi, T. Mukai, K. Morita, and T. Isu, "Doping effect on photocarrier lifetime in InAs quantum dots with strain-relaxed InGaAs barriers grown by molecular beam epitaxy," *Physica E: Low-dimensional Systems and Nanostructures*, 2009.

[110] D. Sreenivasan, J.E.M. Haverkort, T.J. Eijkemans, and R. N\ötzel, "Photoluminescence from low temperature grown InAs/ GaAs quantum dots," *Applied Physics Letters*, vol. 90, 2007, p. 112109.

[111] M. Haiml, U. Siegner, F. Morier-Genoud, U. Keller, M. Luysberg, P. Specht, and E.R. Weber, "Femtosecond response times and high optical nonlinearity in beryllium-doped low-temperature grown GaAs," *Applied Physics Letters*, vol. 74, 1999, p. 1269.

[112] J.D. Joannopoulos, *Photonic crystals: molding the flow of light*, Princeton University Press, 2008.

[113] K. Srinivasan, P.E. Barclay, O. Painter, J. Chen, A.Y. Cho, and C. Gmachl, "Experimental demonstration of a high quality factor photonic crystal microcavity," *Applied Physics Letters*, vol. 83, 2003, p. 1915.

[114] S. McNab, N. Moll, and Y. Vlasov, "Ultra-low loss photonic integrated circuit with membrane-type photonic crystal waveguides," *Optics Express*, vol. 11, Nov. 2003, pp. 2927-2939.

[115] W. Bogaerts, D. Taillaert, B. Luyssaert, P. Dumon, J. Van Campenhout, P. Bienstman, D. Van Thourhout, R. Baets, V. Wiaux, and S. Beckx, "Basic structures for photonic integrated circuits in Silicon-on-insulator," *Optics Express*, vol. 12, Apr. 2004, pp. 1583-1591.

[116] S. Fan, P. Villeneuve, J. Joannopoulos, and H. Haus, "Channel drop filters in photonic crystals," *Optics Express*, vol. 3, Jul. 1998, pp. 4-11.

[117] J.P. Reithmaier, G. Sek, A. Loffler, C. Hofmann, S. Kuhn, S. Reitzenstein, L.V. Keldysh, V.D. Kulakovskii, T.L. Reinecke, and A. Forchel, "Strong coupling in a single quantum dot-semiconductor microcavity system," *Nature*, vol. 432, Nov. 2004, pp. 197-200.

[118] S. Mosor, J. Hendrickson, B.C. Richards, J. Sweet, G. Khitrova, H.M. Gibbs, T. Yoshie, A. Scherer, O.B. Shchekin, and D.G. Deppe, "Scanning a photonic crystal slab nanocavity by condensation of xenon," *Applied Physics Letters*, vol. 87, 2005, p. 141105.

[119] A. Faraon, D. Englund, I. Fushman, J. Vučković, N. Stoltz, and P. Petroff, "Local quantum dot tuning on photonic crystal chips," *Applied Physics Letters*, vol. 90, 2007, p. 213110.

[120] S. Song, S.S. Howard, Z. Liu, A.O. Dirisu, C.F. Gmachl, and C.B. Arnold, "Mode tuning of quantum cascade lasers through optical processing of chalcogenide glass claddings," *Applied Physics Letters*, vol. 89, 2006, p. 041115.

[121] A. Faraon, D. Englund, D. Bulla, B. Luther-Davies, B.J. Eggleton, N. Stoltz, P. Petroff, and J. Vučković, "Local tuning of photonic crystal cavities using chalcogenide glasses," *Applied Physics Letters*, vol. 92, 2008, p. 043123.

[122] G. Berkovic, V. Krongauz, and V. Weiss, "Spiropyrans and Spirooxazines for Memories and Switches," *Chemical Reviews*, vol. 100, May. 2000, pp. 1741-1754.

[123] T. Yoshida and A. Morinaka, "Irreversible photochromism of spiropyran films at low temperatures," *Journal of Photochemistry and Photobiology A: Chemistry*, vol. 78, Mar. 1994, pp. 179-183.

[124] A.K. Chibisov and H. Görner, "Complexes of spiropyran-derived merocyanines with metal ions: relaxation kinetics, photochemistry and solvent effects," *Chemical Physics*, vol. 237, Oct. 1998, pp. 425-442.

[125] F. Xia, L. Sekaric, and Y. Vlasov, "Ultracompact optical buffers on a silicon chip," *Nat Photon*, vol. 1, Jan. 2007, pp. 65-71.

[126] M. Notomi, E. Kuramochi, and T. Tanabe, "Large-scale arrays of ultrahigh-Q coupled nanocavities," *Nat Photon*, vol. 2, Dec. 2008, pp. 741-747.

[127] S. Noda, “Seeking the Ultimate Nanolaser,” *Science*, vol. 314, Oct. 2006, pp. 260 -261.

[128] T. Ishihara, Y. Ikemoto, T. Goto, A. Tsujimura, K. Ohkawa, and T. Mitsuyu, “Optical gain in an inhomogeneously broadened exciton system,” *Journal of Luminescence*, vol. 58, Jan. 1994, pp. 241-243.

[129] T.B. Norris, K. Kim, J. Urayama, Z.K. Wu, J. Singh, and P.K. Bhattacharya, “Density and temperature dependence of carrier dynamics in self-organized InGaAs quantum dots,” *Journal of Physics D: Applied Physics*, vol. 38, 2005, pp. 2077-2087.

[130] J. Johansen, S. Stobbe, I.S. Nikolaev, T. Lund-Hansen, P.T. Kristensen, J.M. Hvam, W.L. Vos, and P. Lodahl, “Size dependence of the wavefunction of self-assembled InAs quantum dots from time-resolved optical measurements,” *Physical Review B*, vol. 77, Feb. 2008, p. 073303.

[131] O. Painter, R.K. Lee, A. Scherer, A. Yariv, J.D. O’Brien, P.D. Dapkus, and I. Kim, “Two-Dimensional Photonic Band-Gap Defect Mode Laser,” *Science*, vol. 284, Jun. 1999, pp. 1819 -1821.

[132] T. Yoshie, O.B. Shchekin, H. Chen, D.G. Deppe, and A. Scherer, “Quantum dot photonic crystal lasers,” *Electronics Letters*, vol. 38, 2002, p. 967–968.

[133] H. Altug and J. Vučković, “Photonic crystal nanocavity array laser,” *Phys. Lett*, vol. 81, 2002, p. 2680–2682.

[134] S. Strauf, K. Hennessy, M.T. Rakher, Y.-S. Choi, A. Badolato, L.C. Andreani, E.L. Hu, P.M. Petroff, and D. Bouwmeester, "Self-Tuned Quantum Dot Gain in Photonic Crystal Lasers," *Physical Review Letters*, vol. 96, Mar. 2006, p. 127404.

[135] M. Nomura, S. Iwamoto, K. Watanabe, N. Kumagai, Y. Nakata, S. Ishida, and Y. Arakawa, "Room temperature continuous-wave lasing in photonic crystal nanocavity," *Optics Express*, vol. 14, 2006, p. 6308–6315.

[136] Y. Gong, B. Ellis, G. Shambat, T. Sarmiento, J.S. Harris, and J. Vuckovic, "Nanobeam photonic crystal cavity quantum dot laser," *Optics Express*, vol. 18, Apr. 2010, pp. 8781-8789.

[137] B. Ellis, I. Fushman, D. Englund, B. Zhang, Y. Yamamoto, and J. Vučković, "Dynamics of quantum dot photonic crystal lasers," *Applied Physics Letters*, vol. 90, 2007, p. 151102.

[138] Y. Zhang, M. Khan, Y. Huang, J. Ryou, P. Deotare, R. Dupuis, and M. Lončar, "Photonic crystal nanobeam lasers," *Applied Physics Letters*, vol. 97, 2010, p. 051104.

[139] J. Hendrickson, B.C. Richards, J. Sweet, S. Mosor, C. Christenson, D. Lam, G. Khitrova, H.M. Gibbs, T. Yoshie, A. Scherer, O.B. Shchekin, and D.G. Deppe, "Quantum dot photonic-crystal-slab nanocavities: Quality factors and lasing," *Physical Review B*, vol. 72, Nov. 2005, p. 193303.

[140] K.A. Atlasov, M. Calic, K.F. Karlsson, P. Gallo, A. Rudra, B. Dwir, and E. Kapon, “Photonic-crystal microcavity laser with site-controlled quantum-wire active medium,” *Optics Express*, vol. 17, 2009, pp. 18178-18183.

[141] M. Nomura, N. Kumagai, S. Iwamoto, Y. Ota, and Y. Arakawa, “Laser oscillation in a strongly coupled single-quantum-dot-nanocavity system,” *Nature Phyics*, vol. 6, Apr. 2010, pp. 279-283.

[142] A. Faraon and J. Vučković, “Local temperature control of photonic crystal devices via micron-scale electrical heaters,” *Applied Physics Letters*, vol. 95, 2009, p. 043102.

[143] B. Maune, M. Lončar, J. Witzens, M. Hochberg, T. Baehr-Jones, D. Psaltis, A. Scherer, and Y. Qiu, “Liquid-crystal electric tuning of a photonic crystal laser,” *Applied Physics Letters*, vol. 85, 2004, p. 360.

[144] D. Sridharan, E. Waks, G. Solomon, and J.T. Fourkas, “Reversible tuning of photonic crystal cavities using photochromic thin films,” *Applied Physics Letters*, vol. 96, 2010, p. 153303.

[145] G. Bjork and Y. Yamamoto, “Analysis of semiconductor microcavity lasers using rate equations,” *Quantum Electronics, IEEE Journal of*, vol. 27, 1991, p. 2386–2396.

[146] R. Hui, S. Benedetto, and I. Montrosset, “Near threshold operation of semiconductor lasers and resonant-type laser amplifiers,” *Quantum Electronics, IEEE Journal of*, vol. 29, 1993, p. 1488–1497.

[147] M. Bagheri, M.H. Shih, S.J. Choi, J.D. O’Brien, and P.D. Dapkus, “Microcavity Laser Linewidth Close to Threshold,” *Quantum Electronics, IEEE Journal of*, vol. 45, 2009, p. 945–949.

[148] M. Nomura, S. Iwamoto, A. Tandaechanurat, Y. Ota, N. Kumagai, and Y. Arakawa, “Photonic band-edge micro lasers with quantum dot gain,” *Optics Express*, vol. 17, Jan. 2009, pp. 640-648.

[149] H. Kim, M.T. Rakher, D. Bouwmeester, and P.M. Petroff, “Electrically pumped quantum post vertical cavity surface emitting lasers,” *Applied Physics Letters*, vol. 94, 2009, p. 131104.

[150] F. Raineri, C. Cojocaru, R. Raj, P. Monnier, A. Levenson, C. Seassal, X. Letartre, and P. Viktorovitch, “Tuning a two-dimensional photonic crystal resonance via optical carrierinjection,” *Optics Letters*, vol. 30, Jan. 2005, pp. 64-66.

[151] T. Ide, T. Baba, J. Tatebayashi, S. Iwamoto, T. Nakaoka, and Y. Arakawa, “Lasing characteristics of InAs quantum-dot microdisk from 3 K to room temperature,” *Applied Physics Letters*, vol. 85, 2004, p. 1326.

[152] J. Buback, M. Kullmann, F. Langhojer, P. Nuernberger, R. Schmidt, F. Würthner, and T. Brixner, “Ultrafast Bidirectional Photoswitching of a Spiropyran,” *Journal of the American Chemical Society*, vol. 132, Nov. 2010, pp. 16510-16519.

[153] N.P. Ernsting, B. Dick, and T. Arthen-Engeland, “The primary photochemical reaction step of unsubstituted indolino-spiropyrans,” *Pure and Applied Chemistry*, vol. 62, 1990, pp. 1483-1488.

[154] K. Uchida, T. Ishikawa, M. Takeshita, and M. Irie, “Thermally irreversible photochromic systems. Reversible photocyclization of 1,2-bis(thiazolyl)perfluorocyclopentenes,” *Tetrahedron*, vol. 54, Jun. 1998, pp. 6627-6638.

[155] M. Irie, T. Lifka, K. Uchida, S. Kobatake, and Y. Shindo, “Fatigue resistant properties of photochromic dithienylethenes: by-product formation,” *Chemical Communications*, 1999, pp. 747-750.

[156] A.K. Ekert, “Quantum cryptography based on Bell’s theorem,” *Physical Review Letters*, vol. 67, 1991, p. 661.

[157] T. Jennewein, C. Simon, G. Weihs, H. Weinfurter, and A. Zeilinger, “Quantum Cryptography with Entangled Photons,” *Physical Review Letters*, vol. 84, May. 2000, p. 4729.

[158] C.H. Bennett, G. Brassard, C. Crépeau, R. Jozsa, A. Peres, and W.K. Wootters, “Teleporting an unknown quantum state via dual classical and Einstein-Podolsky-Rosen channels,” *Physical Review Letters*, vol. 70, Mar. 1993, p. 1895.

[159] D. Bouwmeester, J.-W. Pan, K. Mattle, M. Eibl, H. Weinfurter, and A. Zeilinger, “Experimental quantum teleportation,” *Nature*, vol. 390, Dec. 1997, pp. 575-579.

[160] W.T. Buttler, R.J. Hughes, P.G. Kwiat, S.K. Lamoreaux, G.G. Luther, G.L. Morgan, J.E. Nordholt, C.G. Peterson, and C.M. Simmons, “Practical Free-Space Quantum Key Distribution over 1 km,” *Physical Review Letters*, vol. 81, Oct. 1998, p. 3283.

[161] K. Mattle, H. Weinfurter, P.G. Kwiat, and A. Zeilinger, “Dense Coding in Experimental Quantum Communication,” *Physical Review Letters*, vol. 76, Jun. 1996, p. 4656.

[162] P.G. Kwiat, K. Mattle, H. Weinfurter, A. Zeilinger, A.V. Sergienko, and Y. Shih, “New High-Intensity Source of Polarization-Entangled Photon Pairs,” *Physical Review Letters*, vol. 75, Dec. 1995, p. 4337.

[163] D. Jaksch, H.-J. Briegel, J.I. Cirac, C.W. Gardiner, and P. Zoller, “Entanglement of Atoms via Cold Controlled Collisions,” *Physical Review Letters*, vol. 82, Mar. 1999, p. 1975.

[164] S.D. Barrett and P. Kok, “Efficient high-fidelity quantum computation using matter qubits and linear optics,” *Physical Review A*, vol. 71, Jun. 2005, p. 060310.

[165] P. van Loock, T.D. Ladd, K. Sanaka, F. Yamaguchi, K. Nemoto, W.J. Munro, and Y. Yamamoto, “Hybrid Quantum Repeater Using Bright Coherent Light,” *Physical Review Letters*, vol. 96, Jun. 2006, p. 240501.

[166] R. Bose, D. Sridharan, G.S. Solomon, and E. Waks, “Observation of strong coupling through transmission modification of a cavity-coupled photonic crystal waveguide,” *Optics Express*, vol. 19, Mar. 2011, pp. 5398-5409.

[167] D. Englund, A. Faraon, B. Zhang, Y. Yamamoto, and J. Vuckovic, “Generation and transfer of single photons on a photonic crystal chip,” *Optics Express*, vol. 15, Apr. 2007, pp. 5550-5558.

[168] E. Moreau, I. Robert, J.M. Gérard, I. Abram, L. Manin, and V. Thierry-Mieg, “Single-mode solid-state single photon source based on isolated quantum dots in pillar microcavities,” *Applied Physics Letters*, vol. 79, 2001, p. 2865.

[169] A. Badolato, K. Hennessy, M. Atatüre, J. Dreiser, E. Hu, P.M. Petroff, and A. Imamoğlu, “Deterministic Coupling of Single Quantum Dots to Single Nanocavity Modes,” *Science*, vol. 308, May. 2005, pp. 1158 -1161.

[170] C. Santori, M. Pelton, G. Solomon, Y. Dale, and Y. Yamamoto, “Triggered Single Photons from a Quantum Dot,” *Physical Review Letters*, vol. 86, Feb. 2001, p. 1502.

[171] R.M. Stevenson, R.J. Young, P. See, D.G. Gevaux, K. Cooper, P. Atkinson, I. Farrer, D.A. Ritchie, and A.J. Shields, “Magnetic-field-induced reduction of the

exciton polarization splitting in InAs quantum dots," *Physical Review B*, vol. 73, Jan. 2006, p. 033306.

[172] E.A. Stinaff, M. Scheibner, A.S. Bracker, I.V. Ponomarev, V.L. Korenev, M.E. Ware, M.F. Doty, T.L. Reinecke, and D. Gammon, "Optical Signatures of Coupled Quantum Dots," *Science*, vol. 311, Feb. 2006, pp. 636 -639.

[173] D. Gammon, "Quantum dots: An optical point of view," *Nat Phys*, vol. 3, Nov. 2007, pp. 761-762.

[174] K.-M.C. Fu, C. Santori, C. Stanley, M.C. Holland, and Y. Yamamoto, "Coherent Population Trapping of Electron Spins in a High-Purity n-Type GaAs Semiconductor," *Physical Review Letters*, vol. 95, Oct. 2005, p. 187405.

[175] C. Santori, P. Tamarat, P. Neumann, J. Wrachtrup, D. Fattal, R.G. Beausoleil, J. Rabeau, P. Olivero, A.D. Greentree, S. Prawer, F. Jelezko, and P. Hemmer, "Coherent Population Trapping of Single Spins in Diamond under Optical Excitation," *Physical Review Letters*, vol. 97, Dec. 2006, p. 247401.

[176] P. Kok and B.W. Lovett, "Materials science: Qubits in the pink," *Nature*, vol. 444, Nov. 2006, p. 49.

[177] M. Nomura, N. Kumagai, S. Iwamoto, Y. Ota, and Y. Arakawa, "Laser oscillation in a strongly coupled single-quantum-dot-nanocavity system," *Nature Physics*, vol. 6, Apr. 2010, pp. 279-283.